The Calcite($10\bar{1}4$) Surface: A Versatile Substrate for Molecular Self-Assembly

Dissertation
zur Erlangung des Grades
"Doktor der Naturwissenschaften"
im Promotionsfach Physikalische Chemie

am Fachbereich Chemie, Pharmazie und Geowissenschaften
der Johannes Gutenberg-Universität Mainz

Philipp Alexander Rahe

geboren in Osnabrück

Mainz, den 24. Juni 2011

This thesis was supervised by [Personal data removed] and was carried out at the Universität Osnabrück and the Johannes Gutenberg-Universität Mainz from April 2008 to June 2011.

D77 (Dissertation Johannes Gutenberg-Universität Mainz)

Dekan:	[Personal data removed]
1. Berichterstatter:	[Personal data removed]
2. Berichterstatter:	[Personal data removed]
3. Berichterstatter:	[Personal data removed]
Tag der mündlichen Prüfung:	15. Juli 2011

Dedicated to my parents and to my sister.

Contents

1. Introduction **1**

2. Molecules on dielectric substrates **5**

3. Methods **11**
3.1. Non-contact atomic force microscopy 11
3.2. Experimental setup 14
3.2.1. Ultra-high vacuum system 14
3.2.2. AFM head and electronics 15
3.2.3. Sample preparation 16
3.2.4. Molecule deposition 17
3.3. Data analysis, processing and representation 18
3.4. Error analysis 18

4. Atom tracking **21**
4.1. 3D data acquisition – a literature review 22
4.2. Thermal drift 25
4.3. Atom-tracking principle 27
4.4. Implementation 29
4.5. Performance 34
4.5.1. Input signal quality 34
4.5.2. Output signal quality 35
4.5.3. Tracking functionality 37
4.5.4. Drift characteristics and effective tracking precision 38
4.5.5. Reproducible line-data acquisition 39
4.6. 3D data acquisition 40
4.6.1. Protocol for 3D data acquisition 40
4.6.2. Demonstration on Calcite 42
4.6.3. Post-processing 44
4.7. Conclusions 46

5. The calcite (10.4) surface **49**
5.1. Bulk properties 49
5.2. The (10.4) surface 52
5.3. Surface reconstructions 54

5.4. Symmetry and chirality . . . 57
5.5. Identification of the surface orientation by optical means . . . 59
5.6. NC-AFM study of the calcite (10.4) surface . . . 61
5.6.1. Specific methods . . . 62
5.6.2. Contrast classification scheme . . . 62
5.6.3. Distance dependent contrast formation . . . 67
5.6.4. Tip-termination dependent contrast formation . . . 73
5.6.5. Imaging in the repulsive regime . . . 75
5.6.6. Identifying the carbonate group orientation . . . 76
5.7. Conclusions . . . 78

6. Molecular self-assembly on the calcite (10.4) surface 81
6.1. Hexa-peri-hexabenzocoronene . . . 82
6.1.1. Introduction . . . 82
6.1.2. Morphology on calcite . . . 83
6.1.3. Low-temperature experiments . . . 84
6.1.4. Island morphology . . . 86
6.1.5. Detailed island structure . . . 87
6.1.6. Conclusions . . . 90
6.2. Fullerene C_{60} . . . 91
6.2.1. Introduction . . . 91
6.2.2. Morphology on calcite . . . 92
6.2.3. Detailed structure . . . 93
6.2.4. NC-AFM imaging process . . . 94
6.2.5. Conclusions . . . 97
6.3. Terephthalic acid . . . 98
6.3.1. Introduction . . . 98
6.3.2. Adsorption at room temperature . . . 99
6.3.3. Structural model . . . 100
6.3.4. Low temperature experiments . . . 104
6.3.5. Conclusions . . . 105
6.4. Trimesic acid . . . 106
6.4.1. Introduction . . . 106
6.4.2. Adsorption on calcite . . . 106
6.4.3. Varied coverages of TMA . . . 110
6.4.4. Conclusions . . . 111
6.5. Helicenes . . . 113
6.5.1. Introduction . . . 113
6.5.2. Results and discussion . . . 114
6.5.3. Conclusions . . . 120

7. Summary 121

Bibliography **125**

A. Surface energies **145**

B. Atom tracking: technical details **147**

C. Model for drift velocity calculation **155**

D. Optical properties of calcite **159**
D.1. Coordinate sytems 159
D.2. Optical indicatrix 160

E. Energy barrier estimation **165**

Acknowledgements **167**

Publications and presentations **169**

1. Introduction

What would happen if we could arrange the atoms
one by one the way we want them?
R. Feynman, 1959

To give matter specific forms, to combine different materials and to accomplish special functionalities is accounted as one of the major achievements of mankind. The history of processing and combining materials already started ~ 2.5 million years ago in the early pleistocene epoche, where stones, wood and bones have been shaped on a tangible scale to tools such as hand axes, cutters or spearheads. Over the last centuries, most impressive developments in all fields of fundamental research, materials research, engineering and manufacturing peak in the nowadays extensive availability of materials with tailor-made and outstanding properties. This includes materials withstanding extreme conditions such as needed in aeronautics or fusion reactors [152], materials shaped to complex structures as small as 25 nm [40], for example widely used in modern processors, or materials suitable for high-efficient energy storage [181].

In his famous speech "There's plenty of room at the bottom" [60], Richard Feynman first formulated in 1959 the vision that no physical reason would contradict building single objects out of single atoms at the atomic length scale. Compared to the well-established "top-down" methodology, this "bottom-up" approach provides great potential, as it controls the assembly at the smallest possible chemical level. The research field, where the properties of matter are investigated and controlled on a scale smaller than 100 nm, is nowadays well-known as the interdisciplinary field of *nanotechnology*.

The real-space visualisation of single atoms on solid conducting surfaces became widely available after the invention of the scanning tunnelling microscope (STM) by Gerd Binnig and Heinrich Rohrer [28]. By measuring a *current*, which tunnels through a tiny gap between a conducting sample and a metallic tip, they first mapped the lateral positions of atoms on a Si(111)−(7×7) surface in 1983 [29]. Among historians, the invention of the STM is accounted for the main boost in the field of nanotechnology [210].

This invention induced, furthermore, the development of the large family of scanning probe microscopes (SPM) [16, 38]. In this family, the atomic force microscope (AFM) [27] has proven to be a most versatile tool for the investigation of

insulating surfaces, surfaces which are inaccessible to STM. By measuring *forces* instead of *currents*, Franz Giessibl has first presented true atomic resolution on a Si(111)−(7×7) surface in 1995 [66] by using the frequency modulated non-contact (NC) AFM mode [8]. The reliability and resolution capability increased over the last decade to an outstanding performance, where even submolecular resolution is possible. This has recently been demonstrated by Leo Gross and coworkers [80] by imaging the detailed molecular structure of a pentacene molecule.

With the availability of these valuable surface science tools, it became possible to address most exciting questions in both, fundamental and application oriented research fields [16, 38, 199]. Feynman's vision of creating objects atom-by-atom was first brought to life by Donald Eigler and Erhard Schweitzer in 1990 [52], where they used the tip of an STM to arrange 35 Xe atoms to their employer's name. Soon afterwards, the whole field of SPM investigations of atomic and molecular adsorption studies evolved [19, 18, 102] and the applications of these systems include ongoing fields such as catalysis [46], self-cleaning surface modifications [151] or high-efficient solar cells [110]. During the last decade, molecular structures of increasing complexity have been presented on conducting surfaces, including the formation of extended networks [194], of uni-directional "wires" [20] or of quasi zero-dimensional extent [227]. It has also been possible to manipulate single molecules [135] and to locally induce chemical reactions [91], both by using the STM tip. This *serial* approach is, however, time-consuming and inefficient in terms of device mass production. These limitations are elegantly overcome by the principles of *molecular self-assembly* [220], which proved to be a promising strategy to highly parallelise molecular structure formation.

The majority of self-assembled structures in two dimensions has, however, so far been presented on *conducting* surfaces. The usage of *dielectric* substrates is certainly for many future applications, such as molecular electronics [98], an inescapable necessity. On these *insulators*, a molecular structure is effectively decoupled from a conducting environment, and any electronic functionality is exclusively given by the adsorbed molecular layer.

Consequently, investigating molecular adsorption on dielectric substrates attracted increased interest during the last years and the experimental tool NC-AFM became the first-class choice for the real-space mapping. Early investigations [109, 35] on alkali halides such as NaCl or KBr, however, revealed a severely reduced molecule-substrate interaction, compared to adsorption studies on conducting samples. In the majority of the studies, where molecules such as perylene derivatives, porphyrines or fullerenes have been deposited, the substrate had only little or almost non-existent influence on the resulting molecular structures. In most cases, the molecules have even not favoured a wetting layer on the surface, instead they have formed a three-dimensional crystal structure [109, 47, 35]. With

this growth behaviour, the molecules effectively deprive themselves from further studies in two dimensions on insulating surfaces and finding strategies to circumvent this behaviour constitutes currently an utmost demand.

In terms of this demand, I will start in the first chapter of this thesis with discussing the quantity "surface energy" as a macroscopic parameter to decide upon the suitability of a substrate concerning molecular self-assembly in two dimensions. Furthermore, the analysis will indicate that different surfaces than those presented so far in literature might be more favourable choices. According to the presented analysis, one of the most promising dielectric substrates for molecular adsorption studies is the calcite $CaCO_3$(10.4) surface.

Investigating and understanding the properties of the calcite (10.4) surface are for themselves challenging tasks, mainly because the explanations for the surface reconstructions are still incomplete [170, 185] and the NC-AFM contrast formation is poorly understood [15, 63]. In Chapter 5, I will briefly review the current literature understanding, followed by a presentation and discussion of own NC-AFM experimental results. Most interestingly, one surface reconstruction is identified to lead to a chiral surface, a finding which has not been discussed in literature so far. The emergence of the surface chirality in high-resolution NC-AFM data will be presented. The acquisition of these high-quality NC-AFM data requires a most stable AFM system, which is achieved here by a home-built atom-tracking system. The development of this system was part of the dissertation project and is in detail described in Chapter 4. The system compensates thermal drift and features a most precise tip-positioning. Therefore, it allows for acquiring dense three-dimensional data at room temperature, one example for a full 3D data set from a $CaCO_3$(10.4) surface will be presented.

The adsorption of different organic molecules on the $CaCO_3$(10.4) surface is studied in Chapter 6. Five molecules with systematically alternating properties are chosen. The structural variety of the resulting assemblies will range from close-packed islands to uni-directional molecular "wires" of well-defined width.

This study of molecular adsorption constitutes the first successful molecular self-assembly investigation on the $CaCO_3$(10.4) surface under ultra-high vacuum conditions. In sharp contrast to similar investigations on other non-conducting surfaces, two-dimensional structures are obtained here that are clearly influenced by the substrate structure. This opens up the possibility of specifically tailoring molecular structures by templating of a non-conducting substrate. The results of this thesis are, thus, a great achievement in the field of successful two-dimensional molecular structure formation on insulating substrates.

2. Molecules on dielectric substrates

The *growth modes* of adsorbates (such as single atoms or organic as well as inorganic molecules) deposited on solid substrates has been classified by Bauer [22]. For the case of thermodynamic equilibrium, he differentiated between three well-known cases, namely Frank–van–der–Merwe (layer–by–layer) growth, Stranski–Krastanov (layer–plus–bulk) growth and Volmer–Weber (bulk) growth. These modes are depicted in Figure 2.1.

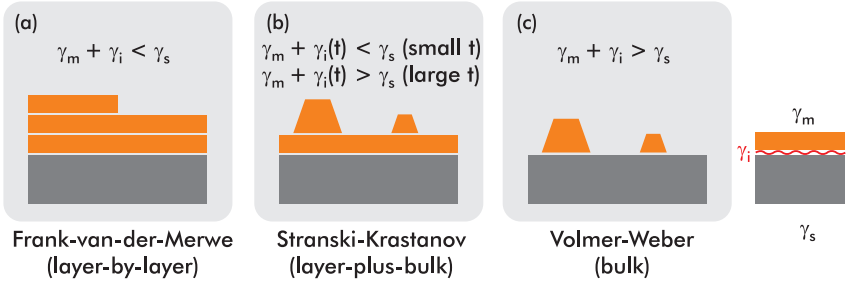

Figure 2.1.: Growth modes classified by Bauer [22]: (a) Frank–van–der–Merwe (layer–by–layer) growth, (b) Stranski–Krastanov (layer–plus–bulk) growth and (c) Volmer–Weber (bulk) growth. The growth modes are characterised by the macroscopic quantity "surface energy" of the substrate (γ_s) and the adsorbate (γ_m) as well as by the interface energy γ_i. t is the film thickness.

The growth modes are characterised in terms of the *surface energy* of the molecular deposit (γ_m) and of the solid substrate (γ_s) [216]. This quantity is a *macroscopic* material property. Layer-by-layer growth is favoured for $\gamma_m+\gamma_i<\gamma_s$, while bulk growth occures if $\gamma_m+\gamma_i>\gamma_s$, where γ_i is the interface energy. This interface energy is also a macroscopic quantity and includes all microscopic contributions from the interface formation, such as chemical bond formation or electronic as well as geometric relaxations in the substrate or molecular film. Here, also stress induced into the molecular film due to an incommensurability of the molecular structure to the substrate lattice is included in γ_i. Additionally, the interface energy γ_i is often dependent on the thickness t of the molecular film. In case of the layer–plus–bulk growth mode, the interface energy is substantially different for

the first and subsequent layers, thus, promoting a layer–by–layer growth in the first, but bulk growth in subsequent layers.

Bulk growth is highly undesireable in the context of molecular self-assembly as the formation of a molecular bulk crystal prevents exploiting the two-dimensional (2D) structural variety. To allow for tuning the 2D molecular structure formation, first the molecules necessarily need to wet the surface and, second, the substrate needs to provide a templating effect. Such growth of 2D structures is only promoted if the molecular film features layer–by–layer growth. While this growth mode is predominantly found for organic molecules on conducting surfaces [19, 20, 21, 104], bulk growth is omnipresent on insulating surfaces such as KBr(100), NaCl(100) or KCl(100) [109, 34, 35, 47, 73]. A recent review on the involved *dewetting process* is given by Burke *et al.* [35].

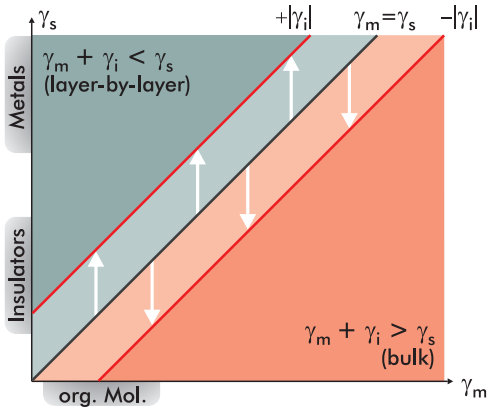

Figure 2.2.: Surface energies determining the molecular growth on substrates. The green shaded region depict combinations of (γ_m, γ_s), where layer–by–layer growth is featured. Bulk growth is favoured in the red shaded area.

The latter finding, that insulating surfaces predominantly feature bulk growth, is readily understandable from a straightforward analysis of the involved energetics. This is depicted in Figure 2.2. Here, the surface energy γ_m of the molecular deposit is plotted along the abscissa, while γ_s of the substrate is plotted along the ordinate. As a first assumption, I consider an interface energy of zero ($\gamma_i = 0$) with the system in the thermodynamic equilibrium. For this case, the identity function drawn black in Figure 2.2 separates the areas for (γ_m, γ_s) combinations, where the system preferres layer–by–layer or bulk growth. Next, for an interface energy $\gamma_i \neq 0$, this line shifts up or down, enlarging one growth mode area while diminishing the other. Usually, the interface energy γ_i is initially not known for a given materials combination, but the surface energies are available in literature for a large variety of the individual systems. Accepting the interface energy as an unknown quantity firsthand, the diagram clearly presents, that a substrate with a large surface energy γ_s features a larger range for the interface energy where layer–by–layer growth is possible. To cut a long story short, large surface-energy

substrates should be chosen for studying molecular self-assembly.

Figure 2.3 depicts the same diagram as Figure 2.2, but now with specific data concerning substrates and molecules reported in literature. Values for the surface energies are taken from various references, a list is given in the Appendix Section A. Substrates suitable for *molecular self-assembly* [220] are found at values of large γ_s, where even for large interface energies the layer–by–layer growth condition $\gamma_m + \gamma_i < \gamma_s$ is fulfilled. Furthermore this diagram suggests, that *dielectric surfaces* such as KBr(100), NaCl(100) or KCl(100), which have often been used for studying molecular adsorption, constitute unfortunate choices unless the deposited molecules form strong bonds to the surface. This is, however, usually not the case as bulk growth is regularly observed [109, 34, 35, 47, 73]. In this thesis,

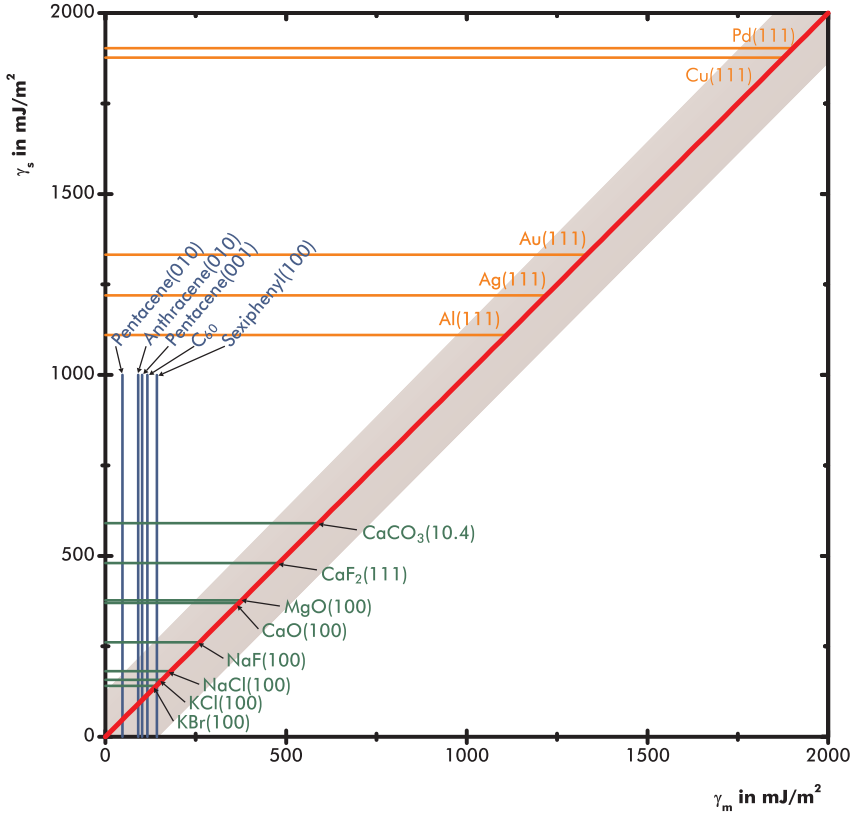

Figure 2.3.: Relation between the surface energies and the growth mode with specific data concerning typical substrates and molecules reported in literature. The values are taken from various references, a list is given in the Appendix Section A.

I choose the calcite $CaCO_3(10.4)$ surface as a promising candidate for studying molecular self-assembly. This promise is well-founded by the preceding analysis, because the surface energy of $CaCO_3(10.4)$ is with a value of $590\,mJ/m^2$ among the largest surface energies of insulators. The results presented in Chapter 6 will fully justify this promise. Consequently, I introduce the $CaCO_3(10.4)$ surface as a suitable substrate for studying molecular self-assembly with this work.

The preceding analysis discusses only one necessary condition for the successful formation of two-dimensional self-assembled molecular structures, as it only accounts for the wetting/dewetting process. Once adsorbed on the surface, however, every molecule is subject to the *kinetic processes* governing the self-assembly process. Of these processes, diffusion of a single molecules in two dimensions on the surface is the most important one. It is characterised by the *diffusion barrier* E_d a molecule has to overcome when it "jumps" from one energetic minimum to the next in the adsorption energy landscape, i.e. from one surface site to the adjacent. The structure formation itself might additionally undergo complicated processes involving various energy barriers [122]. For simplicity, I herein consider only one intermolecular binding energy E_{inter} as the relevant parameter. Dewetting and other multilayer growth processes are not discussed in the following.

The relations relevant for the energetics in a molecular self-assembly process have been analysed by Kühnle [104]. According to that study, a 2D self-assembled structure can only evolve, if the intermolecular interaction E_{inter} is in range but slightly larger than the diffusion barrier E_d. Additionally, the *rate* to overcome both energy barriers has to be sufficiently high at the temperature of request, usually room temperature. It has been proposed [104] to abstract this as a molecular thermal energy E_{mol}, an energy the molecule can overcome at a reasonable rate. This energy encompasses all relevant molecular excitations. Thus, the necessary conditions for all involved energetics are given by [104]:

$$E_b > E_{inter} \geq E_{mol} \geq E_d \tag{2.1}$$

where E_b is the binding energy of the molecule to the substrate.

This introduction revealed certain aspects relevant for the process of molecular self-assembly, with a focus on dielectric substrates. First of all, the macroscopic quantity "surface energy" is found to be decisive for the applicability of a substrate in terms of molecular wetting. The relations between the involved energy barriers govern the kinetic processes and the substrate templating effect influences the structural variety.

Surface energies for a large number of substrates and few molecular crystals are readily available in literature. In contrast, the interface energy γ_i as well as

the energy barriers E_d and E_b are rarely available for molecule/insulator systems initially, as this involves discussing the combined molecule/substrate system.

For the $CaCO_3$(10.4) surface, no molecular structure formation under ultra-high vacuum conditions has been observed so far, neither are data available for the energetics. A first attempt for studying molecular adsorption on $CaCO_3$(10.4) has been presented by Schütte [184]. He investigated the cytosine/$CaCO_3$(10.4) system, however, no stable structure formation has been observed at room temperature. The current work will, thus, present an important step in the context of molecular self-assembly on dielectric substrates.

3. Methods

Non-contact atomic force microscopy (NC-AFM) operated in the frequency modulation (FM) mode under ultra-high vacuum (UHV) conditions is the main experimental technique used within this thesis. This chapter will briefly introduce the measurement principle in Section 3.1 and describe the experimental setup in Section 3.2. A few remarks on the data analysis, processing and representation are given in Section 3.3 and error sources will be discussed in Section 3.4.

3.1. Non-contact atomic force microscopy

The atomic force microscope (AFM) is one technique from the large family of scanning probe microscopy (SPM). It has initially been developed by Binnig *et al.* [27] as a successor of the scanning tunnelling microscope (STM), which has been invented by Binnig and Rohrer [28] before. The AFM extends the SPM principle to insulating substrates, where *forces* are measured instead of a tunnelling *current* in the STM. In AFM, a force sensing tip is mounted to the free end of a cantilever and is rastered over a sample surface. The force on the cantilever tip due to the interaction with the sample is recorded for each spatial position. In the *beam-deflection* configuration [134], a laser is focused on the free cantilever end and is reflected to a photosensitive detector. The cantilever deflection is detected from the laser deflection on the photosensitive detector. In the *contact mode* AFM technique, this deflection is the main measurement signal.

Albrecht *et al.* [8] extended this principle to the so-called *frequency modulation* (FM) detection. Here, the cantilever is oscillated at its current resonance frequency f. The *frequency shift* Δf, often named *detuning*, is defined as $\Delta f = f - f_0$, where f_0 is the resonance frequency of the freely oscillating cantilever. The tip-sample interaction changes the cantilever's resonance frequency, and the frequency shift Δf is related to the tip-sample interaction force F_{ts} by the following equation [69, 67, 92]:

$$\Delta f(z) = \frac{f_0}{\pi k_0 A^2} \int_{-A}^{A} F_{\mathrm{ts}}\left(z + A - q\right) \frac{q}{\sqrt{A^2 - q^2}} \mathrm{d}q. \tag{3.1}$$

In this equation, k_0 is the cantilever stiffness and A is the oscillation amplitude. The Δf is dependent on the tip-sample distance z. With the frequency mod-

ulation technique, true[1] atomic resolution has first been demonstrated by Giessibl [66] on the Si(111) − (7 × 7) and, since then, NC-AFM has proven to be a powerful tool in surface science. A recent review by Barth *et al.* [16] summarises the achievements, which nowadays includes sub-molecular resolution [80].

Figure 3.1 depicts the typical setup for an NC-AFM operated in the FM mode. A laser beam is focused on the free end of a cantilever and the reflection is ad-

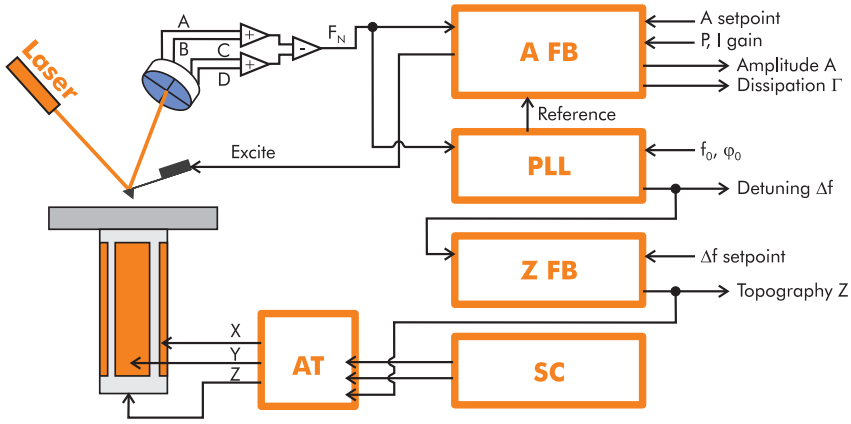

Figure 3.1.: Setup for FM NC-AFM used within this thesis. Left side: AFM scan head with piezo, light source and photosensitive detector. Right side: Electronics consisting of amplitude feedback (A FB), Phase-locked loop (PLL), distance feedback (Z FB), scan controller (SC) and atom-tracking system (AT).

justed to hit a photosensitive detector. Usually, this detector is a four quadrant photodiode. The deflection signal F_N is calculated as the intensity difference between the upper and the lower half. In good approximation, this signal is proportional to the cantilever deflection. In the FM NC-AFM mode, F_N is usually a sinusoidal signal. The frequency of this sine is detected by a phase-locked loop (PLL), which gives the difference $\Delta f = f - f_0$ between the current frequency to a preset frequency f_0 as an output. This signal is the main measurement signal in the FM NC-AFM mode and ideally contains the whole interaction information. It is fed into a feedback loop (Z FB), which keeps the frequency shift to a preset value $\Delta f_{\text{setpoint}}$. A second feedback loop (A FB) keeps the cantilever oscillation amplitude at a predefined value A_{setpoint} by adjusting the magnitude of the cantilever excitation signal (Excite).

[1] A subtle difference exists between lattice and true atomic resolution. While resolving the atomic lattice with the contact AFM is easily possible on substrates such as HOPG or mica, the identification of single surface defects usually remains to the high-resolution FM mode. This is accounted for the fact, that in contact mode a large tip averages the interaction over several surface sites, while in the FM mode ideally the front-most tip atom defines the predominant interaction.

The sample is positioned relative to the tip by means of piezo elements[2]. A scan controller generates respective waveforms to raster the tip systematically over the sample surface. Furthermore, the scan controller digitises all input signals and organises the data storage. The vertical positioning is governed by a *feedback loop*, which adjusts the tip-sample distance in order to nullify $\Delta f_{\text{setpoint}} - \Delta f$. Here, Δf is the current frequency shift of the cantilever oscillation.
The interaction between the AFM tip and the investigated sample is often highly complex and involves numerous physical interactions. Relevant for this work are the following:

Van–der–Waals forces These forces have a long-range character and are inevitably present. Even in the absence of permanent dipoles, dispersion forces cause always an attractive force under vacuum conditions between tip and sample. Dispersion forces are usually calculated from an integration over all atoms using cones, spheres or other geometries to model an AFM tip in front of a plane representing the sample surface [67]. For the case of a conical tip of infinite height, the force is given by [67]

$$F_{\text{vdW}}(z) = -\frac{A_H \tan^2(\alpha)}{6}\frac{1}{z} \tag{3.2}$$

with the Hamaker constant A_H and the half tip angle α. Formulae for van–der–Waals forces in different geometries are presented by Israelachvili [95].

Electrostatic forces Long-range electrostatic interactions contribute to the total force, if a potential is present between the tip and the sample. This includes applied voltages, different work-functions of the tip and sample materials and localised charges. Especially for *in-situ* cleaved insulators, usually charges remain on the sample surface after the cleavage process. The force for this electrostatic interaction is described by

$$F_{\text{ES}} = -\frac{1}{2}\frac{\mathrm{d}C(z)}{\mathrm{d}z}V^2 \tag{3.3}$$

with C being the capacitance of the tip-sample system and V being the potential difference between tip and sample. Determining the capacitance for a specific tip-sample geometry is often a challenging task, especially for the case of insulating substrates. However, in high-resolution NC-AFM experiments long-range electrostatic forces usually do not contribute to atomic contrast and are, thus, usually compensated by an applied tip potential V_{tip}. For the determination of V_{tip}, often the Kelvin-probe technique is employed. With this technique, the tip-sample voltage to minimise the electrostatic force is determined for each sample position and spatially

[2] In various systems, the sample is fixed and the tip is positioned by piezo elements.

mapped in addition to the other measurement signals. A recent review on this technique is given by Melitz *et al.* [133].

Chemical forces This interaction includes all contributions of short-range chemical interaction. This might involve chemical bond formation, charge transfer, orbital overlap or Pauli repulsion. It is difficult to give an abstract formulation, as the precise distance dependence is usually determined from *ab-initio* methods modelling the full tip-sample system.

In order to give an instructive visualisation, usually these contributions are condensed into well-known empirical potentials, such as the Lennard-Jones, Morse or Buckingham type. Using the Morse potential as an example, Figure 3.2 presents the relation between interaction force F_{ts} and the frequency shift Δf for typical experimental parameters.

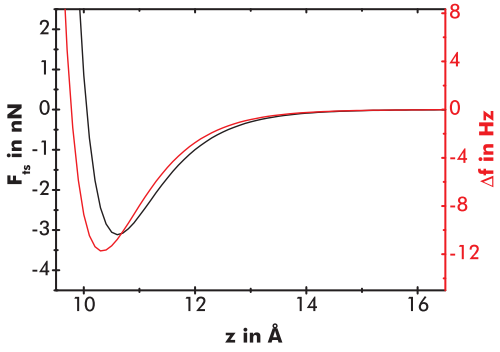

Figure 3.2.: Visualisation of an exemplary interaction force and the resulting frequency shift Δf. (Parameters: $f_0 = 300\,\mathrm{kHz}$, $k = 40\,\mathrm{N/m}$, $A = 10\,\mathrm{nm}$, potential parameters from [59]).

3.2. Experimental setup

For this thesis, a commercial AFM from Omicron Nanotechnology (Taunsstein, Germany) is used. The AFM is mounted in an ultra-high vacuum (UHV) system, where all experiments including sample preparation are performed. The UHV system contains three separate chambers: The AFM chamber, a preparation chamber and a load-lock to transfer AFM cantilevers or samples from atmosphere to UHV and vice-versa without breaking the vacuum. A photographic picture of the whole system and the scan head is given in Figure 3.3(a) and (b), respectively.

3.2.1. Ultra-high vacuum system

The base pressure of the UHV system is typically better than $1 \times 10^{-10}\,\mathrm{mbar}$. The preparation chamber is equipped with an ISE10 (Omicron Nanotechnology) ion

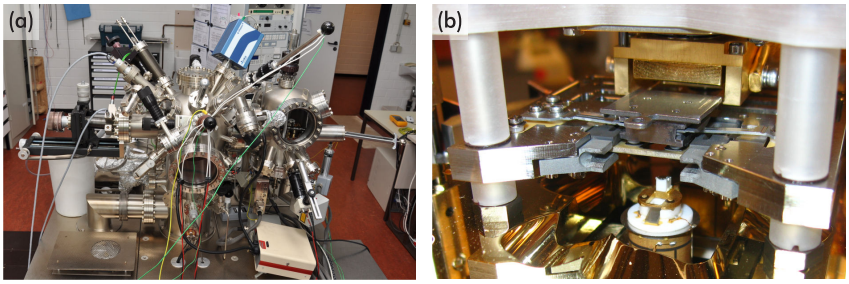

Figure 3.3.: Photographic images of the UHV system (a) and the AFM scan head (b). ((b) adapted from Ref. [184].)

source used for tip preparation and a quadrupol mass spectrometer eVision$^+$ from MKS Instruments (Andover MA, USA) for the residual gas analysis. The molecule deposition is realised by sublimators attached to the analysis chamber (two are depicted in Figure 3.3(a)) and they will be described in Section 3.2.4. The deposition rate is initially measured by a quartz crystal microbalance from Inficon (East Syracuse NY, USA). For variable temperature experiments, a manipulator (Omicron Nanotechnology) with heating and cooling capabilities is available.

3.2.2. AFM head and electronics

The VT AFM 25 (Omicron Nanotechnology) is a combined STM/AFM scan head, which operates in a temperature range of about 25 K to 1500 K. A front view of the tip and sample is presented in Figure 3.3(b). Standard Si cantilevers (type PPP-NCH from Nanosensors, Neuchâtel, Switzerland) with resonance frequencies around 300 kHz and quality factors around 20 000 are used in the beam-deflection detection configuration. All tips are initially bombared by Ar ions to remove contaminants and the oxide layer. The system has been optimised by R. Bechstein [24] for utmost performance. The optimisation steps included the usage of a new light source, the development of a new preamplifier and the usage of a PLL for the signal demodulation. R. Bechstein [24] reported upon a noise background of $(328 \pm 2)\,\mathrm{fmHz}^{-0.5}$ for the optimised system.

The system is equipped with the MATRIX (Omicron Nanotechnology) scan controller. A flexible atom-tracking system was developed within this thesis and is connected to this scan controller. Details about this atom-tracking system will be given in Chapter 4.

3.2.3. Sample preparation

All NC-AFM experiments within this thesis are performed with the calcite (10.4) surface as the substrate. The surface itself is introduced in Chapter 5.

Calcite single crystals of optical quality were bought from Korth Kristalle GmbH (Altenholz (Kiel), Germany) and were mechanically cut to the desired crystal size of $2 \times 4 \times 10\,\mathrm{mm}^3$ supported by the used sample holder. This sample holder has initially been designed by Tröger *et al.* [213] and has been adapted to the herein used system by J. Schütte [184]. It uses a clamping mechanism to fix the calcite crystal. Each crystal is cleaved *in-situ* [213] once and replaced by a new crystal usually latest after one week. Prior to each *in-situ* cleavage, sample holder including the uncleaved crystal are degassed to temperatures of at least 450 K for at least 1 h. The cleavage is performed by scoring lines parallel to the (10.4) plane along the 4 mm crystal side until the topmost part dismantles. A photographic image of the crystal and sample holder will be presented in Chapter 5 in Figure 5.8(f).

Cleaving dielectric samples under vacuum conditions usually leads to highly charged surfaces [224, 17]. AFM experiments on these highly charged surfaces is extremely difficult or even impossible due to huge electrostatic forces overriding the short-range chemical interaction. Therefore, UHV cleaved dielectric samples are usually heated to higher temperatures in order to diminish the surface charge. Even after the annealing procedure, it was necessary to apply voltages in the regime of $\pm 100\,\mathrm{V}$ to the tip to compensate the long-range electrostatic interaction.

It has been proposed by Barth *et al.* [17] that the ionic conductivity is responsible for the charge transport in alkali halides. For calcite $CaCO_3$, the specific conductivity at 300 K has been determined by Rao and Rao [165] to values of $\sigma_{\parallel} = 6 \times 10^{-9}\,\Omega^{-1}\,\mathrm{m}^{-1}$ and $\sigma_{\perp} = 1.7 \times 10^{-8}\,\Omega^{-1}\,\mathrm{m}^{-1}$ parallel and perpendicular to the c-axis, respectively. Using a simple model based on the decharging of a parallel plate capacitor, the surface charge Q decays exponentially with time:

$$\frac{Q(t)}{Q(0)} = \exp\left(-\frac{\sigma}{\epsilon}t\right) \tag{3.4}$$

with σ being the specific conductivity and ϵ being the dielectric permittivity. With the specific conductivities given above, the surface charge diminishes after a few seconds by orders of magnitude, even at room temperature. As this is not observed experimentally, either the crystals used in the study by Rao and Rao have been highly contaminated by dopants, or different processes are involved in the charge compensation process.

3.2.4. Molecule deposition

All molecules are deposited from a heated glass crucible mounted inside the UHV system. A photographic image of one cell including the support is presented in Figure 3.4. This principle follows the design of M. Schunack [183]: A tantalum wire is wound around a glass crucible as a heating coil and a thermocouple melted into one end of the crucible measures the achieved temperature. The molecular material is inserted into the crucible and protected from dropping out by glass wool. To avoid contaminations, a distinct cell is manufactured for each molecule.

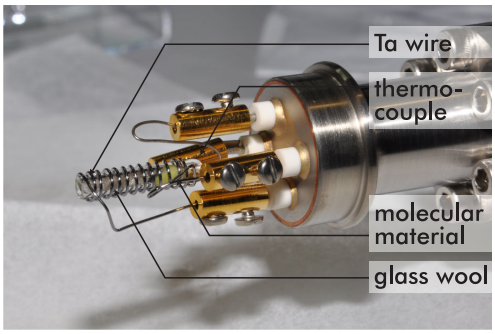

Figure 3.4.: Picture of a sublimation cell mounted to a UHV feedthrough. The Ta wire, the thermocouple, the yellow molecular powder and the glass wool are marked.

Molecular sublimation follows an Arrhenius law, the deposition rate r at a temperature T is given by [143]

$$r = r_0 \exp\left(\frac{E_S}{k_B T}\right) \tag{3.5}$$

where E_S is the sublimation enthalpy and k_B is the Boltzmann constant. For all molecules used within this thesis, Table 3.1 lists a suitable sublimation temperature and an appropriate rate on a $CaCO_3$(10.4) surface. To avoid molecular

Molecule	$T_{\text{sublimation}}$	$r^{-1}_{\text{deposition}}$	Source
HBC	660 K	20 min/ML	Group Prof. Müllen
C_{60}	664 K	15 min/ML	MER Corporation
TPA	383 K	30 min/ML	Fluka
TMA	400 K	25 min/ML	Sigma-Aldrich
[7]HCA	417 K	225 min/ML	Group Dr. Stará

Table 3.1.: Sublimation characteristics of the herein used molecules.

decomposition, which was especially important for the [7]HCA molecules, small sublimation rates were chosen throughout this work.

3.3. Data analysis, processing and representation

All acquired AFM data are initially stored in the proprietary MATRIX file format. To analyse and process these data, the open-source software Gwyddion [142] is used throughout this thesis. Reading the proprietary MATRIX file format was implemented by myself and is included into the official Gwyddion source code.

All frequency shift (Δf) data presented in this thesis are raw data unless stated otherwise. All topography (Z) data are plane-substracted raw data unless stated otherwise. The physical quantities are linearly mapped to a green colorscale, which is depicted in Figure 3.5. The minimum and maximum values are optimised for each data, thus, optimising the visual contrast. For the Δf data, the scale is inverted. With this convention, sample sites with large attractive interaction are depicted "bright", sites with small attractive or even repulsive interaction are depicted "dark".

Figure 3.5.: Color map used within this work for data representation.

3.4. Error analysis

The NC-AFM technique involves a large number of parameters, all of which have to be carefully adjusted. Most of all, care is taken to operate all involved feedback loops at their optimum. Optimising the amplitude feedback loop reduces disturbances in the Δf channel and, furthermore, ensures a pure FM NC-AFM mode with the Δf related to the force as given by Equation 3.1. This equation has been derived under the assumption of a constant amplitude. It is not necessarily valid in a mixed AM/FM NC-AFM mode.

The distance feedback-loop settings are chosen accordingly to the favoured imaging mode. In the constant-Δf mode, the feedback loop works at the optimum and ideally, the whole interaction information is given exclusively by the topography channel. In the constant-height mode, the feedback is deactivated and the whole information is given by the Δf data. This mode requires a most stable system, which is realised here with the newly developed atom-tracking technique (see Chapter 4 for details). Last, in a quasi constant-height mode, the distance feedback loop is set to a very low bandwidth and is, thus, ideally only compensating the sample tilt and thermal drift. The Δf signal is then accounted to be comparable to the true constant-height mode.

For a quantitative data analysis, several subtleties need to be considered in terms of systematic errors. First of all, the calibration of the piezo scanner was checked regularly by the whole team measuring the unit cell dimensions of samples such as $Si(111)-(7\times7)$, $CaF_2(111)$ and $CaCO_3(10.4)$ [184, 24, 159]. For both lateral dimensions X and Y, a correction factor of 0.87 ± 0.01 was determined and all data are recalibrated accordingly. Measured heights at the atomic scale might be severely wrong, because the "height" is solely defined by the same *interaction* difference. Especially measuring the height of adsorbed molecules is prone to large errors if electrostatic interaction is involved [178], and due to specific chemical interactions, there is even no guarantee that an adsorbed species is imaged as a protrusion [62]. Lateral dimensions are often highly distorted due to thermal drift. A recipe for a posterior data correction has been given by myself and coworkers [160] and is used within this work if necessary.

4. Atom tracking

In numerous fields, such as surface chemistry, thin film growth, molecular electronics or nanotribology, it is of especial interest to measure the entire three-dimensional interaction field of a tip-surface system [23]. Especially for the AFM, the force field is of utmost interest, because from this data physical and chemical information can be extracted [203, 80, 81]. An impressive example has been presented by Sugimoto *et al.* [203]. On a Si(111) surface, with some of the surface atoms replaced by single tin or lead atoms, they have succeeded in tagging the chemical identity of each surface atom, combining distance dependent force data with *ab-initio* calculations. Moreover, the short-range interaction on surfaces such as Si(111) [203, 202], KBr(001) [201, 174, 175], NaCl(100) [180, 99], NiO(001) [186, 94, 114], MgO/Ag(001) [87] and graphite [7] has been investigated at the atomic level by means of 3D NC-AFM imaging. Furthermore, 3D data has been taken on small molecules adsorbed on metal substrates such as PTCDA/Cu(111) [33] and PTCDA/Ag(111) [32] and on large structures such as carbon nanotubes [11]. Recently, also the acquisition of 3D data in a liquid environment on muscovite mica(001) [64] has been demonstrated.

Additionally, the use of a complete three-dimensional data set removes some of the peculiarities in analysing SPM image data, which especially might constitute a prerequisite for interpreting NC-AFM data. To mention one example, Loske *et al.* [124] have presented a contrast inversion [161] in the NC-AFM contrast formation on the $C_{60}/TiO_2(110)$ system. Especially, identifying the centre of a single C_{60} molecule is not unambigously possible from one single image.

There are two experimental difficulties in acquiring a complete three-dimensional data set: Tip stability and uncontrolled tip-sample movement. Both difficulties arise from the fact, that a long time is needed to record the data. The uncontrolled tip-sample movement is generally caused by thermal drift, while also electronic drift[1] as well as piezo creep and hysteresis may contribute. Both problems are reduced by orders of magnitudes when performing experimens at temperatures as low as 5 K in a bath cryostat [7, 94, 201, 80]. In these low-temperature environments, residual drift velocities between 0.1 pm/min and 1 pm/min have been reported in literature [7, 94, 201, 80], thus, thermal fluctuations are virtually absent. In contrast, for room-temperature environments drift velocities in the

[1] Nowadays, electronic drift is expected to be neglectible. The temperature coefficient of the herein used frequency detector "easyPLL plus" is 3.5 mHz/K [139].

order of 100 pm/min are found.

An elegant technique to virtually eliminate drift artifacts is the atom-tracking [153] and feedforward technique. For the NC-AFM, these techniques have first been adapted by Abe *et al.* [1] in 2005.

In this chapter, I present a most flexible, newly developed and home-built drift-compensation system. This system features drift measurement and compensation modules which use the atom-tracking and feedforward principles. Furthermore it provides routines for reliable and reproducible line (1D), true constant-height image (2D) and volume-data (3D) acquisition. Part of the development and results presented herein have recently been published in *Review of Scientific Instruments* in Ref. [164].

The chapter is organised as follows: First, the protocols for 3D data acquisition presented in literature so far are reviewed in Section 4.1. In Section 4.2, thermal drift is characterised from a theoretical model and the induced problems are adressed in more detail. The atom-tracking technique itself is introduced in Section 4.3, followed by the technical description of the herein developed system in Section 4.4. The performance of this system is analysed in Section 4.5 and, most important, the 3D NC-AFM data acquisition is presented in the last Section 4.6.

4.1. 3D data acquisition – a literature review

The effectiveness and robustness of acquiring dense 3D data is primary a question of the used protocol. For all "simple" protocols, the effective drift is minimised before data are acquired. Small drift is per-se the case in a low-temperature environment. Contrary, a feedforward technique is commonly necessary to minimise the large drift velocities under room-temperature conditions. This feedforward technique usually extrapolates a measured drift vector with a linear model. Having the drift minimised, the distance feedback loop is switched off and data recording is started. Comments on the maximum duration for reliable data acquisition is deferred to Section 4.2.

Data acquisition is often performed in form of constant height images at different tip-sample (Z) distances. This mode is depicted in Figure 4.1(a). Herein, I classify all protocols by the order of the fastest to the slowest scan direction, for Figure 4.1(a) this reads X-Y-Z. Comparable with this protocol is the sampling of Z-X slices as depicted in Figure 4.1(b), where the type is X-Z-Y. Both protocols have widely been used in literature and prominent examples are reviewed in Table 4.1. Albers *et al.* [7] have used consecutively acquired images comparable to the X-Y-Z type, but they acquired the images with the distance feedback loop active. The resulting data is not equally spaced and, thus, has been aligned and fitted by numerical means afterwards [6]. However, this strategy is highly disputable as it relies on a large number of assumptions for the investigated tip-sample system. A

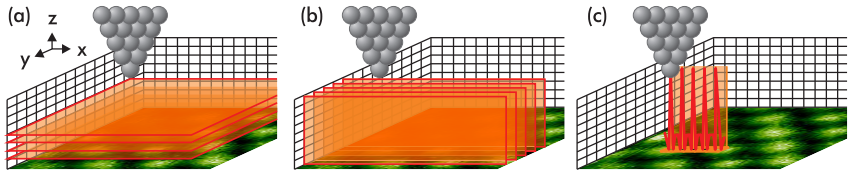

Figure 4.1.: "Simple" protocols for acquiring 3D data. (a) Numerous constant-height images are measured at varied tip-sample distance. (b) Follows the same strategy, but with the axes swapped. (c) The data space is sampled by the acquisition of single line data such as $\Delta f(z)$ curves.

third very common strategy is to acquire single line data such as $\Delta f(z)$ curves as type Z-X-Y. The curves are sampled systematically on a raster and combined to a three dimensional data set. This strategy is depicted in Figure 4.1(c) and literature demonstrations are included in Table 4.1. From a technical point, all these protocols use the standard scanner movements *imaging* and *spectroscopy*. Thus, these functionalities are usually available directly in any commercial scan controller.

Table 4.1.: Literature survey on 3D data acquisition. Only publications with a full 3D data space are considered. Values not deducable from literature are marked by "?".

sample system	environment duration	size	protocol
Hölscher, Schwarz, Langkat *et al.* [94, 186, 114] in 2002, 2003			
NiO(001)	UHV, 14.9 K 80 min total	$32 \times 32 \times 256$ pixel, $1 \times 1 \times 10\,\mathrm{nm}^3$	Z-X-Y
Heyde *et al.* [87] in 2006			
MgO/Ag(001)	UHV, 5 K	$1.5 \times 1.5 \times 0.95\,\mathrm{nm}^3$	Z-X-Y
Schirmeisen *et al.* [180] in 2006			
NaCl(100)	UHV, 300 K 15 min total	$34 \times 10 \times 481$ pixel, $2 \times 2 \times 1.1\,\mathrm{nm}^3$	Z-X-Y
Ruschmeier *et al.* [174, 175] in 2008, 2009			
KBr(001)	UHV, 300 K 10.2 min total	$38 \times 6 \times 477$ pixel, $\sim 2\times?\times 1.2\,\mathrm{nm}^3$	Z-X-Y
Gross *et al.* [80] in 2009			
Pentacene on NaCl/Cu(111)	UHV, 5 K $\sim$ 18 h total	$80 \times 40\times?$ pixel, $\sim 2.5 \times 1 \times 1.3\,\mathrm{nm}^3$	Z-X-Y (intermediate drift correction)

Table 4.1.: (continued)

sample system	environment duration	size	protocol
Albers *et al.* [7, 6] in 2009			
HOPG(0001)	UHV, 6 K 40 h total	$256 \times 119 \times 140$ pixel $1750 \times 810 \times 172\,\mathrm{pm}^3$	X-Y-Z (Z FB on, intense data processing)
Ashino *et al.* [11] in 2009			
SWCNT	UHV, < 13 K	$41 \times 41 \times 512$ pixel, $1.2 \times 1.2 \times 3\,\mathrm{nm}^3$	Z-X-Y (intermediate Z FB on)
Braun *et al.* [33, 32] in 2009, 2010			
PTCDA/Ag(111)	UHV, 300 K	not given	Z-X-Y (intermediate Z FB on)
Such *et al.* [201] in 2010			
KBr(001)	UHV, 5 K 85 s/image	$1.3 \times 1.3 \times 4\,\mathrm{nm}^3$	X-Y-Z
Fukuma *et al.* [64] in 2010			
Muscovite(001)	liquids, 300 K 53 s total	$64 \times 64 \times 155$ pixel, $4 \times 4 \times 0.78\,\mathrm{nm}^3$	Z-X-Y (Z Modulation)
Kawai *et al.* [99] in 2011			
NaCl(001)	UHV, 300 K 23.5 h total	$71 \times 71 \times 256$ pixel, $0.7 \times 0.7 \times 1\,\mathrm{nm}^3$	Z-X-Y (intermediate AT)
This Work in 2011			
$CaCO_3$(10.4)	UHV, 300 K ~ 3 h total	$85 \times 85 \times 500$ pixel, $1.74 \times 1.74 \times 2.18$ nm	Z-X-Y: (intermediate AT)

All "simple" protocols rely on virtually zero drift, which constitute their severe drawback. The duration of data acquisition, especially under room-temperature conditions, is usually limited to few minutes, resulting only in small data spaces. This limitation is circumvented by a more "advanced" data acquisition protocol, which I developed and implemented within this work. It is based on the atom-tracking principle and can handle large and especially non-linear drift. It will be described in Section 4.6.1 and examplary 3D data acquired on a $CaCO_3$(10.4) surface will be presented in Section 4.6.2. A similar approach to this protocol has very recently and independently been demonstrated by Kawai *et al.* [99] on a NaCl(001) substrate.

4.2. Thermal drift

Thermal drift, which is predominantly caused by the material's response to a temperature variation, prohibits a reliable and well-defined tip positioning in most scanning probe microscopy (SPM) experiments. It introduces distortions in SPM images and, most importantly, prohibits a long-lasting data acquisition with the distance feedback loop switched off.

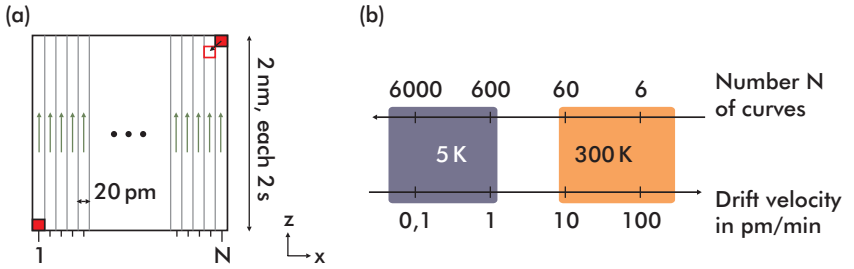

Figure 4.2.: Accurancy achieved under different thermal drift environments. (a) Visualises the considered data acquisition model (see main text for details). (b) The total number N of reasonable drift-free curves is calculated for different drift velocities present in typical environments.

Figure 4.2 exemplifies this problem in data acquisition. I consider line-data acquisition with the distance feedback loop switched off. A total of N single curves are sampled evenly spaced along the X-axis. This series of curves is expected to be reasonable drift-free, if the last acquired pixel in this series is offset by the pixel spacing. This spacing is assumed to a typical value of 20 pm and a total time of 2 s per curve is chosen. The numbers N for typical drift velocities are calculated as presented in Figure 4.2(b). For a dense three-dimensional data set, a curve number in the order of 10^3 is necessary and, thus, the effective drift velocity during this experiment has to be smaller than 1 pm/min to gain reproducible data.

Thermal drift originates from thermal compression or expansion of all materials integrated in an SPM head and microscope support, with the coefficient of thermal expansion α and the thermal diffusivity D being the relevant material constants. To illustrate the temperature-induced effects, the drift velocity is calculated for a simple model system as shown in Figure 4.3(a): two rods of length L are connected to a heat reservoir on the left side, while their right ends are free in vacuum and thermally isolated from the environment. The rods consist of two different materials and are assumed to be one-dimensional. At time $t = 0$, both rods are at a temperature ΔT lower than the heat reservoir. Consequently, the initial temperature distribution is a step function as depicted in Figure 4.3(b). Solv-

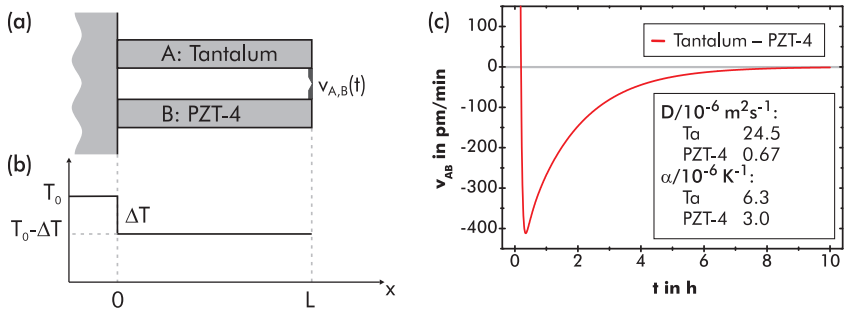

Figure 4.3.: (a) Model used for the drift velocity calculation. The velocity $v_{A,B}$ is modelled by the relative movement of the right ends of two rods. (b) Initial temperature distribution. (c) Drift velocity as a function of time for the materials combination tantalum – PZT-4 and $\Delta T = 100\,\mathrm{mK}$.

ing the heat equation, the velocity $v_{A,B}$ of the right rod ends relative to each other is given by the following equation (for the full derivation see Appendix Section C):

$$v_{A,B}(t) = \frac{\Delta T}{L} \sum_{n=1}^{\infty} \left[2D_A \alpha_A e^{-\frac{\pi^2}{L^2}\left(n-\frac{1}{2}\right)^2 D_A t} - 2D_B \alpha_B e^{-\frac{\pi^2}{L^2}\left(n-\frac{1}{2}\right)^2 D_B t} \right] \tag{4.1}$$

with α_A (α_B) being the coefficient of thermal expansion and D_A (D_B) being the thermal diffusivity of the upper (lower) rod, respectively. The movement of the two rod ends relative to each other represent the drift velocity due to a rapid temperature change ΔT.

Usually, the sample in an SPM is fixed by metals such as tantalum, copper or stainless steel whereas the piezo is made of ceramics such as PZT-4. As an example for the drift characteristics, the thermal drift velocity $v_{A,B}$ for the materials combination tantalum – PZT-4 is presented in Fig. 4.3(c).

The long-time behaviour of the drift velocity follows an exponential decay law with respect to time t, the behaviour is explicitly *not* linear. For the given materials combination and a temperature difference of $\Delta T = 100\,\mathrm{mK}$, the drift velocity exhibits a minimum and is, thus, even non-monotonic. After one hour of system relaxation, the drift is still as high as 300 pm/min. This simplified model demonstrates the displeasing thermal drift characteristics of non-linearity and non-monotonicity. Simple compensation methods based on long-term linear extrapolation have been presented throughout literature [160], but have yielded tolerable results only for short time intervals.

For measuring and compensating thermal drift, the strategies can be split in *online* (during the experiments) and *offline* (after finishing the experiments) procedures. A short review about these procedures has recently been given by myself

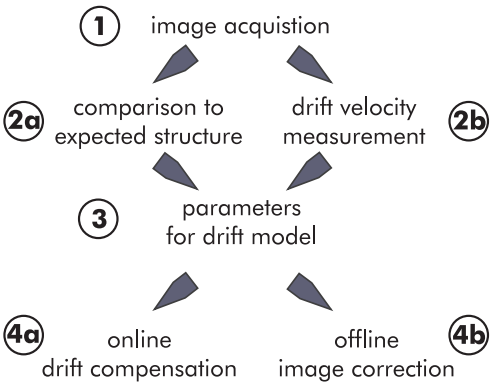

Figure 4.4.: Characterising the tasks of thermal drift compensation (adapted from Ref. [160]).

and coworkers [160]. The basic methodology for the whole correction process is presented in Figure 4.4, where the main tasks are the drift velocity measurement in step 2 and compensation in step 4. In this work, the atom-tracking technique handles step 2b in it's tracking module and step 4a in it's feedforward module.

4.3. Atom-tracking principle

The atom-tracking technique has initially been developed by Pohl and Möller [153] for the scanning tunnelling microscope (STM). It was mainly used to study the diffusion kinetics of atoms and molecules on metal surfaces by locking the STM tip to a single adsorbate and following its movement, while recording all three spatial positions. Most prominent, the diffusion and rotation kinetics of Si-Si and Si-Ge dimers on Si(001) have been studied by Swartzentruber *et al.* [204, 205, 157] and by Krueger *et al.* [108]. Using the STM, it was also possible to track single hydrogen atoms on Si(001) as presented by Hill *et al.* [89]. For the NC-AFM technique, Abe *et al.* [2, 1, 3] have first employed atom tracking for drift compensation. In contrast to the STM experiments, a stable surface feature is chosen as the tracking reference. Consequently, the relative movement between tip and sample is measured as a virtual feature movement.

The atom-tracking technique is usable for different SPM techniques, but herein exclusively explained and employed for the NC-AFM, using the frequency shift Δf as the input signal. Figure 4.5(a) presents the basic principle: the AFM tip is dithered on an elliptic trajectory around a surface protrusion, which is here accepted as a single surface atom. Depending on the experiment, however, surface depressions, adsorbed atoms or adsorbed molecules represent other feasible choices. Suitable values for the dithering amplitude $A_{\mathrm{x,y}}$ and frequency $f_{\mathrm{x,y}}$ are

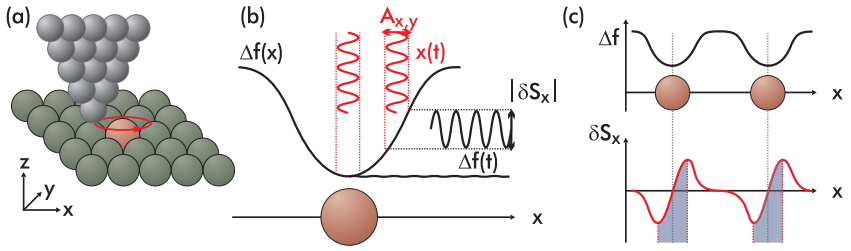

Figure 4.5.: Principle of atom tracking. A single surface feature is tracked by dithering the tip around the feature (a). For the X-direction, the dithering causes a nearly sinusoidal oscillation with amplitude $|\delta S_x|$ in the Δf channel, if the tip is offset from the feature centre (b). More specifically, the signal δS_x depends on the dithering centre position relative to the surface feature (c).

mainly given from by the size of the protrusion as well as the detection system bandwidth and protrusion movement velocity.

Without loss of generality, the elliptic trajectory of the tip is defined by two sine waveforms of equal amplitude and frequency, but with a phaseshift Θ:

$$x(t) = A_{\mathrm{x,y}} \sin\left(2\pi f_{\mathrm{x,y}} t\right) \tag{4.2}$$

$$y(t) = A_{\mathrm{x,y}} \sin\left(2\pi f_{\mathrm{x,y}} t + \Theta\right) \tag{4.3}$$

whereby $x(t)$ and $y(t)$ denote the time-dependent tip position in each lateral dimension. If the atom is perfectly circular and centred in the origin of the dithering circle, the tip follows a trajectory of equal interaction. Hence, the Δf signal is virtually constant in time[2] as depicted in Figure 4.5(b) for the X direction (lowest $\Delta f(x)$ point). However, if the atom is not perfectly centred in the dithering circle, a modulation with time is observed in the Δf channel. As an approximation, this signal is given by:

$$\Delta f(t) \approx |\delta S_{\mathrm{x}}| \sin(2\pi f_{\mathrm{x,y}} t) + \left|\delta S_{\mathrm{y}}\right| \sin(2\pi f_{\mathrm{x,y}} t + \Theta). \tag{4.4}$$

The amplitudes $|\delta S_{\mathrm{x}}|$ and $\left|\delta S_{\mathrm{y}}\right|$ depend on the lateral offset from the centre and the tip-sample interaction strength itself. The in-phase ($\mathrm{LIA_x}$) and quadrature ($\mathrm{LIA_y}$) signal of $\Delta f(t)$ can be extracted using a two-phase lock-in amplifier triggered to the $x(t)$ signal. The signals are in good approximation given by:

$$\mathrm{LIA_x} \approx \tfrac{1}{2} \delta S_{\mathrm{x}} \tag{4.5}$$

$$\mathrm{LIA_y} \approx \tfrac{1}{2} \delta S_{\mathrm{y}} \cos(\Theta) \tag{4.6}$$

[2] Depending on the feature outline and dithering amplitude, a small ripple might still present, especially if the tip is only dithered along one direction.

Here, it is obvious to choose the phaseshift to $\Theta = 90°$ to gain maximum sensitivity. The tip dithering trajectory becomes a circle in this case.

In the limit $A_{x,y} \to 0$, the relation between the lock-in input signal Δf and the in-phase signal δS_x (δS_y) is given by the derivation along the X (Y) direction, respectively. For X, this is visualised in Figure 4.5(c): Inside the blue shaded regime, the in-phase signal δS_x is zero for the centre position, while is is positive (negative) for the tip being misplaced to the right (left) of the surface atom, respectively. This monotonic relationship between tip misplacement and lock-in signal can be exploited to keep the tip right in the centre of the chosen protrusion by using two independent feedback loops. The feedback condition for the X (Y) loop is $\mathsf{LIA}_x = 0$ ($\mathsf{LIA}_y = 0$), respectively. Obviously, this principle only succeeds when operated in the blue shaded regime.

With this technique, the tip of the NC-AFM is *locked* to a single surface atom and, as the surface atom is immobile on the surface, the tip positioning data are identical to the drift movement. These positioning data are extracted from the actuating variables of both lateral feedback loops in form of path-time data $x_{\text{drift}}(t)$ and $y_{\text{drift}}(t)$. Along the third dimension, which is the Z direction, the drift movement $z_{\text{drift}}(t)$ is given by the output of the Z feedback loop. It should be reminded, this feeback loop adjusts the tip-sample distance by keeping the detuning setpoint constant. It's bandwidth is set to values smaller than $f_{x,y}$ herein.

The thermal drift data are given in form of $x_{\text{drift}}(t)$, $y_{\text{drift}}(t)$ and $z_{\text{drift}}(t)$ path-time diagrams by the tracking technique. To compensate for this movement, usually linear least-squares fits are applied to the data, thus, extrapolating the actual drift with a linear model. In a next step, time-varying signals are added to the scan voltages in a feedforward routine [3], which countersteer the drift induced misplacement. This strategy, however, may not be successful for a time span larger than several minutes. This statement especially holds for room-temperature conditions, where the drift is usually non-linear. Therefore, more advanced strategies are required and one solution will be presented in Section 4.6.1.

4.4. Implementation

To the author's best knowledge, the atom-tracking technique is so far only implemented in one commercially available scan controller [193], and a comparable approach based on different tip trajectories is realised in a second commercial controller [140]. Most importantly, a flexible stand-alone solution is not available. Thus, a drift-compensation system based on the atom-tracking principle is developed within this work, which can be added to the existing SPM controller. The system relies on electronics designed by [Name removed][3] and the programming was performed by myself. The system implements all drift compensation

[3] Werkstatt für Elektronik und IT at the University of Osnabrück

tasks such as atom-tracking and feedforward and, furthermore, it provides protocols for reproducible line, image and volume data acquisition in combination with the MATRIX scan controller.

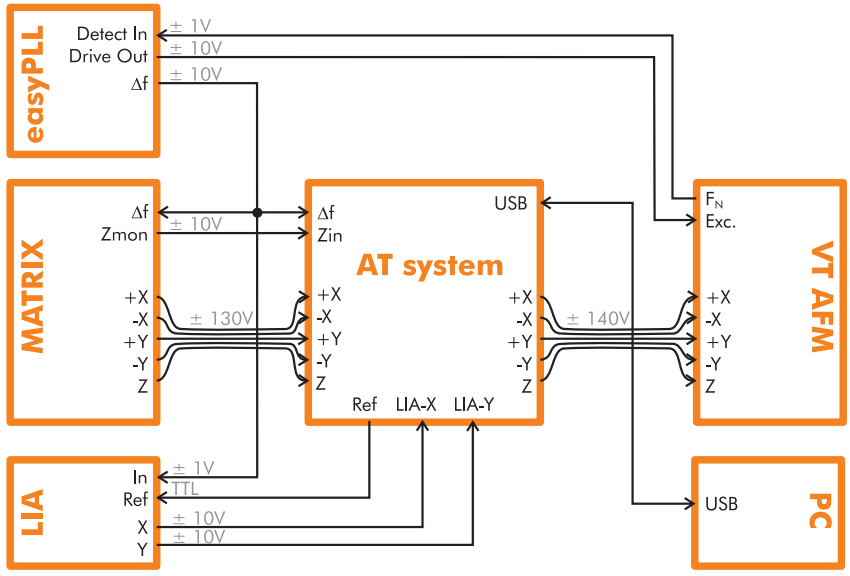

Figure 4.6.: Signal path between the scan controller (MATRIX), the AFM and the atom-tracking (AT) system. The voltage level of each signal is given as well as the direction of signal flow.

The system uses an ATMega 2560 microcontroller from Atmel [12] with self-written algorithms for data flow control, status handling and dynamic procedure generation. The circuit itself is connected to the Omicron VT AFM 25 system, described before in Section 3.2. The central idea of this atom-tracking system is to loop the signals for drift compensation in the high-voltage signal path from the scan controller (MATRIX) to the scanner piezos as depicted in Figure 4.6. The summation circuitry is in detail depicted in Figure 4.7(b). With this summation circuitry, no changes in the scan controller electronics are required. Especially, this circuitry allows for connecting this atom-tracking system to a large variety of scan controllers. For the present controller, the X- and Y-directions are differential channels, whereas the single Z-channel is referenced to the X- and Y-electrodes on the piezo tube.

The atom-tracking system generates five signals[4], each of which is added to a high-voltage channel from the scan controller. For the digital-analog conver-

[4]Additionally, a sixth spare output channel is provided.

sion of these signals, 16 bit converters (Burr-Brown DAC712 [37]) are used. The digital signal lines for each of these digital-analog converters (DAC) are galvanically decoupled using digital isolators[5] (ADuM1400 from Analog Devices, Norwood MA, USA [9]). With these couplers, the resistance and capacitance between the high-voltage signal and the low-voltage circuitry is given to 1 TΩ and 2.2 pF, respectively [9]. A low-voltage low-noise operational amplifier (OPA604 from Burr-Brown [36]) is connected to the output channel of each DAC. For each channel, this operational amplifier (OPA) adds the ±10 V signal from the DAC to the high voltage signal from the scan controller. This circuit is depicted in Figure 4.7(b). The voltage feed for both, the DAC and OPA, is isolated against ground potential for each channel by using DC/DC converters (THI2M and TES1 from Traco Electronic AG, Zurich, Switzerland [211]). With these couplers, the residual resistive and capacitive coupling amounts to at least 1 GΩ and at most 40 pF, respectively [211]. The isolation is robust for potential differences up to 1 kV.

This principle produces scan signals with low output noise and high stability, as low-noise operational amplifiers[6] with increased temperature stability[7] and appropriate precision[8] are feasible. The bandwidth of the operational amplifiers is limited to a maximum frequency of about 20 kHz. This frequency is larger than typical scan waveforms, but noise in the high-frequency regime is suppressed. In conclusion, the advantages of low-noise operational amplifiers are fully utilised and lead to an overall low-noise performance of the system with this circuit.

On the analog input side, numerous low-voltage connections are available at the atom-tracking system. All channels either accept voltages in the regime ±10 V or are of TTL type. As none of the used analog-digital converters (ADC) provide an input range of ±10 V firsthand, suitable amplifier circuits are connected to each input line. Additionally, these circuits protect the ADCs against excess voltages.

In the first hardware version ("version 1"), the 10 bit ADC embedded in the ATMega 2560 microcontroller [12] is used for the analog-digital conversion. The overall performance of this ADC emerged to be poor and, consequently, some signals are sampled by a two-channel external 16 bit ADC in a revised hardware version ("version 2"). However, the experiments presented within this work are

[5] The herein used isolators transfer the logic signals by inductive coupling between miniaturised coils inside the isolators.

[6] The voltage noise at the output of the OPA604 is specified to 1.5 μV_{pp} (20 Hz to 20 kHz) [36], compared to the output noise of a high-voltage amplifier (such as PA15 from APEX[41]) of 30 μV_{rms} (10 kHz bandwidth).

[7] The OPA604 has a voltage drift of ±8 µV/K (0.2 pm/K in X,Y and 0.07 pm/K in Z for herein used AFM), whereas a PA15 presents an output drift of up to 750 µV/K (20 pm/K in X,Y and 6.3 pm/K in Z).

[8] The physical tip movement due to one bit step is defined by the amplification gains and the piezo sensitivity. For the present system, adding the signals before the high-voltage amplifiers would lead to a signal gain of 15 and, consequently, one bit step would correspond to 120 pm in X,Y-direction and to 38 pm in Z-direction.

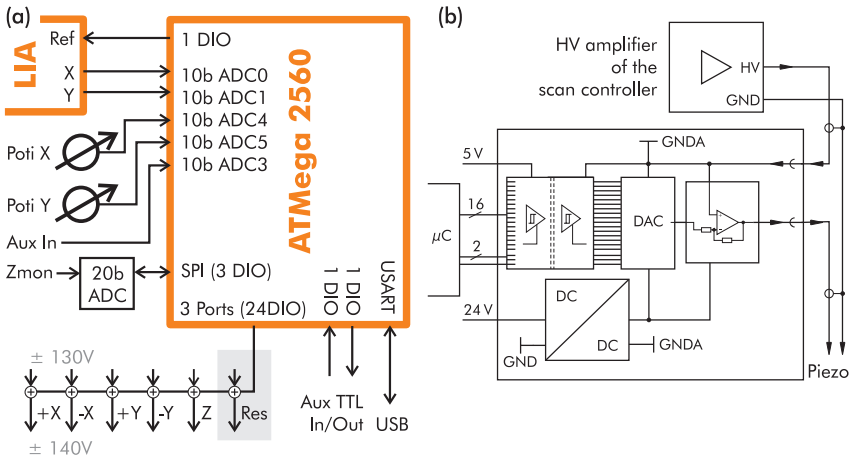

Figure 4.7.: (a) Internal configuration for the used microcontroller ATMega 2560 for hardware version 1 (without the additional 16 bit ADC). (b) High-voltage summation circuitry used for each output channel.

exclusively performed with the first hardware version and the usage of the new ADC is left as an outlook. The basic functionality remains completely the same, but significant improvements are achieved in terms of the stability and performance of the lateral feedback loops.

For the Z position signal, which is generated by the MATRIX scan controller, a high-precision 20 bit converter (LTC2420 from Linear Technology, Milpitas CA, USA [118]) is used. This converter is connected via a serial peripheral interface (SPI) to the microcontroller.

Besides the analog in- and output channels, three TTL signals are available. Most importantly, the reference signal (LockIn Ref) for the lock-in amplifier (LIA) is given as a TTL output and is connected to the LIA. Furthermore, one input and one output TTL channel (Aux TTL In, Aux TTL Out) are available, mainly for debugging purposes. However, these channels may be employed in future as trigger signals for synchronising the atom-tracking system with another scan controller.

Last, the connection between the microcontroller and a computer (PC) is realised using a serial data connection emulated on a universal serial bus (USB) interface. A complete block diagram of the internal schema is depicted in Figure 4.7(a).

I now briefly discuss the software needed to operate the atom-tracking system. For the microcontroller side, a C code is used and compiled by the avr-gcc software development tools [221] is used, while the controlling PC runs a Lab-

view [141] code. Both codes in C and Labview were programmed within this work by myself.

The microcontroller programme is in general implemented as a collection of modules. Most of the modules are implemented as finite state machines. The module states are stored in individual registers and most of these registers are centralised in either the C struct[9] `status` or in a struct of the respective module. The programme is interrupt driven for all time-critical tasks, however, time-consuming tasks are executed in the main programme loop. The synchronisation for the latter functions is realised by interrupt driven trigger variables. For each single module, a function with the name `<modulename>_checkstate()` is defined, which is called continuously inside the main loop. Inside this function, the module functionality is executed in case the respective trigger is set. The following code listing presents the main function:

```
1  int main() {
2    // Load the configuration
3    settings_load();
4
5    // Initialise all modules
6    init();
7
8    // Main Loop
9    while(1) {
10     /* Execute each module: */
11     // ... communication
12     comm_checkstate();
13     // ... tracking module
14     tracking_checkstate();
15     // ... feedforward module
16     ff_checkstate();
17     // ... tip positioning
18     potis_checkstate();
19     // ... oscilloscopes
20     oscis_checkstate();
21     // ... status reporting
22     status_checkstate();
23   }
24
25   // Never reached
26   return 0;
27
28 }
```

The function `main()` is executed directly after booting the microcontroller. At first, the system's settings are loaded in the function `settings_load()`. Second, the initialisation of all modules and the activation of all interrupts is performed in the function `init()`. The system is now ready to handle all module function-

[9] In C, a struct is a type that pools a fixed set of named objects into a single type.

alities. The main loop sequently calls the worker function for every module. The interrupt routines for the time-critical tasks are not included here. Technical details for each module are included in the appendix Section B.

4.5. Performance

The performance of the newly developed system is mainly manifested by the signal quality of the in- and output channels. In this section, I first present the analysis of these signal lines and address the effective tracking and feedforward precision based on experimental data.

4.5.1. Input signal quality

In hardware version 1, the 10 bit ADC in the microcontroller is used for nearly all analog input channels. This ADC digitises an analog signal by successive approximation. It's speed and precision is governed by two parameters: the prescaler `pre` and the sample count N. The ADC clock is defined by the division of the CPU clock by `pre`, and the oversampling is governed by the number N of averages.

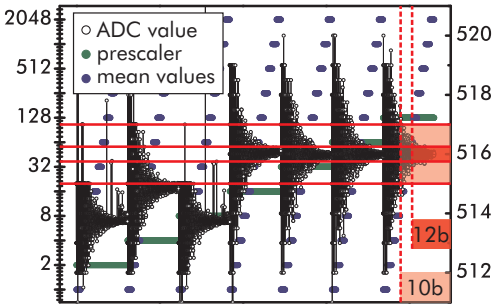

Figure 4.8.: Precision of the ATMega 2560 ADC converters analysed by systematically changing the prescaler `pre` and number of averaged samples N. `pre` and N are referenced to the left scale, sampled values to the right scale.

Figure 4.8 presents the influence of these two parameters on the resulting bit stability in a systematic manner. For all possible prescaler values 1 to 128 (`pre` in green, left scale), the average value from $N = 1 \ldots 2048$ samples (N in blue, left scale) is formed in floating point arithmetic (each value in black, right scale). The red horizontal lines mark the upper and lower level of fluctuations of the least significant bit (LSB) for a numerical precision of 10 bit and 12 bit. From first tests using the in-phase and quadrature signals of an SR830 lock-in amplifier (Stanford Research Systems, Sunnyvale CA, USA) it became evident, that an input sensitivity of 20 mV/LSB as given firsthand by the 10 bit ADC is not sufficient for stable lateral feedback loops. This issue is solved by oversampling, resulting in an effective resolution of 12 bit. While this strategy increases the input sensitivity to 5 mV/LSB, it reduces the sampling rate to about 23 Hz.

Although all data presented in this work are acquired with this analog-digital conversion principle, the system is supplemented by an external two channel 16 bit ADC in hardware version 2. The conversion characteristics of this ADC are included in Table 4.2 besides the former described converters.

For the ZIn channel, a high-precision 20 bit converter is used. The converter uses the delta-sigma technology for generating high-precision values. The characteristics of this converter are listed in Table 4.2. With the respective calibration factors, the input precision in terms of pm is determined to 1.7 pm/LSB.

ADC	signal	voltage	`pre`	N	bit	V precision	rate
ADC0	LIA-X	±10 V	128	128	12	5 mV/LSB	23 Hz
ADC1	LIA-Y	±10 V	128	128	12	5 mV/LSB	23 Hz
ADC3	Aux In	±10 V	128	128	12	5 mV/LSB	23 Hz
ADC4	Poti-X	0…5 V	128	16	10	5 mV/LSB	23 Hz
ADC5	Poti-Y	0…5 V	128	16	10	5 mV/LSB	23 Hz
LTC2420	ZIn	±10 V	—	—	20	0.02 mV/LSB	6 Hz
Hardware version 2:							
16b ADC	LIA-X	±10 V	—	10	12	5 mV/LSB	100 Hz
16b ADC	LIA-Y	±10 V	—	10	12	5 mV/LSB	100 Hz
ExtPotis	Poti-XYZ	0…5 V	128	16	10	5 mV/LSB	∼200 Hz

Table 4.2.: Precision of the ADC converters. `pre` denotes the prescaler used for the ADC, N is the number of averaged samples, bit is the effective bit resolution and rate the effective sample rate. The table is supplemented by the converters used in hardware version 2.

4.5.2. Output signal quality

The positioning precision of the microscope tip is defined by the sensitivity of the piezo scanner and the signal quality of the DAC. The theoretical minimum of the tip positioning is given by the smallest adressable bit step, while the maximum range is limited by the DAC output range. These theoretical extrema are listed in Table 4.3, calculated for the herein used system.

However, these theoretical minima are drowned by the electronic noise present in the signal channels. The effective signal quality at the output channels is now analysed by means of signal analysis. In a first step, a spectrum analyser[10] is connected to the X^+ channel of the scan controller, measuring the signal relative to

[10] The FFT routine of a MFP scan controller is used. The input channel for this controller was calibrated using a DS345 function generator (Stanford Research Systems, Sunnyvale CA, USA).

channel	sensitivity	output voltage range	LSB step	maximum range
X, Y	26.36 nm/V	±10 V	8 pm	±264 nm
Z	8.4 nm/V	±10 V	2.6 pm	±84 nm

Table 4.3.: Precision of the output DACs using the sensitivities for the Omicron VT AFM 25.

ground. The noise amplitude spectral density $d^{\mathrm{U}}_{\mathrm{SC}}$ of this signal is presented as the red solid curve in Figure 4.9. Despite a few peaks at 50 Hz and multiples, the spectral amplitudes in these data remain well below 1 mV/$\sqrt{\mathrm{Hz}}$. In a second step, the atom-tracking summation circuitry is connected to the scan controller output and the X^+ signal after the summation circuitry is analysed again. The respec-

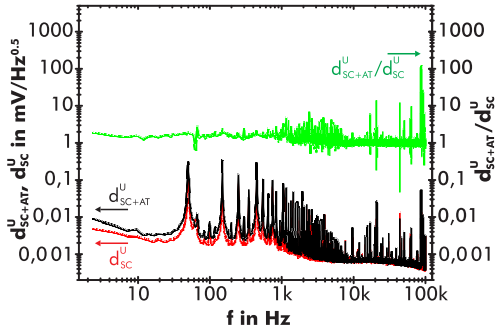

BW	$\Delta x^{\mathrm{RMS}}_{\mathrm{SC}}$	$\Delta x^{\mathrm{RMS}}_{\mathrm{SC+AT}}$
100 Hz	6.7 pm	12.5 pm
1 kHz	13.1 pm	25.4 pm
10 kHz	13.7 pm	26.3 pm
50 kHz	14.1 pm	26.6 pm
100 kHz	14.5 pm	34.4 pm

Figure 4.9.: Signal quality at the X^+ high-voltage output of the scan controller (in red) and of the combined scan controller and atom-tracking system (in black). The quotient is presented in green. To the right, the piezo dislocation noise is calculated for different piezo bandwidths.

tive data $d^{\mathrm{U}}_{\mathrm{SC+AT}}$ indicate a slightly increased noise level, which is directly evident from the quotient $d^{\mathrm{U}}_{\mathrm{SC+AT}}/d^{\mathrm{U}}_{\mathrm{SC}}$ (green curve referenced to the right scale in Figure 4.9). For the relevant low-frequency regime, an increase in noise by a factor of about two is observed. Additionally, in the upper kHz regime peaks evolve, they are most likely caused by the DC/DC converters. In the frequency regime above 100 kHz (not shown), a few sharp peaks are prominent, which are most likely also caused by the DC/DC converters. From the electronic noise I determine the root mean square displacement of the piezo ("piezo dislocation noise") by integrating the power spectral density over different bandwidths and multiplying by the piezo sensitivities. The values for the scan controller and the combined scan controller and atom-tracking system are given additionally in Figure 4.9. The other output channels are checked as well and reveal a comparable behaviour (not shown).

However, due to an increased piezo sensitivity, the dislocation noise in the Z-channel is smaller by about a factor of two.

4.5.3. Tracking functionality

The basic functionality is to measure the relative tip-sample movement and to compensate for this displeasing drift by the feedforward technique. Figure 4.10(a) shows an atomically resolved image of a $CaCO_3(10.4)$ surface with typical distortions present due to large thermal drift. Although the interaction regime is suitable for atomic resolution, single atoms are hardly revealed as their circular shape is elongated to stripes. In Figure 4.10(b), the raster movement is paused after scanning a few lines from top of the image. During this pause, tracking of a single surface atom is performed and the drift-velocity vector is determined from the feedback-loop data. The velocities are used in the feedforward routine to compensate for linear drift and, consequently, distortion-free imaging at the atomic scale is possible as presented in Figure 4.10(c). The precision of the drift velocity measurement depends on the tracking duration and, as present in the middle part of Figure 4.10(b), a residual distortion is present if the time span is chosen too small. Therefore, the feedforward parameters are optimised in a second tracking step as indicated in Figure 4.10(b). With the thermal drift minimised, the unit cell dimensions are measured to $(10.0 \pm 0.2) \times (8.1 \pm 0.2)$Å^2 in excellent agreement with the crystallographic bulk data [51] of 10.0×8.1Å^2.

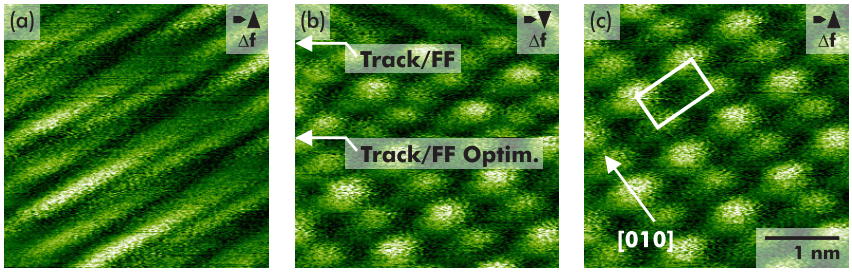

Figure 4.10.: Basic tracking and feedforward functionality: In (a), large thermal drift is present while imaging the surface. Severe deformations of the imaged surface unit cell are apparent. In (b), the imaging is paused and by using the atom-tracking and feedforward techniques, drift is measured and compensated ("Track/FF"). The drift parameters are optimised in a second tracking step ("Track/FF Optim."). With compensated drift, distortion-free imaging as presented in (c) is possible for a short time.

4.5.4. Drift characteristics and effective tracking precision

A single surface atom on a $CaCO_3$(10.4) surface is tracked for a period of about 75 min to investigate the long-term drift characteristics and the effective tracking precision. The corresponding data are presented in Figure 4.11 in the form of path-time diagrams. Each curve represents the feature position along the X, Y and Z direction, respectively. As an immobile feature is chosen, each curve directly describes the relative drift movement between tip and sample. The well-known non-linear behaviour, which became evident from the model calculation in Section 4.2, is most pronounced for the X and Z directions. Additionally, the movement in Z direction is even non-monotonic, hoever, the non-monotonicity may be enhanced by piezo creep in this experiment. Exemplary for the X direction, the

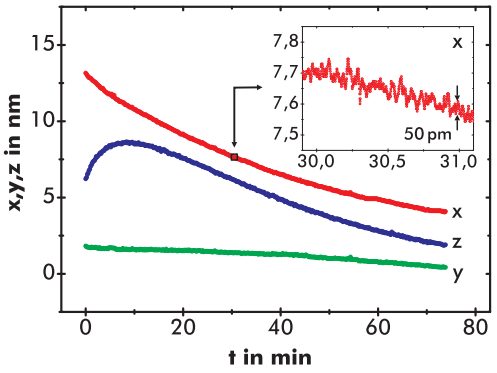

Figure 4.11.: Drift characteristics and positioning precision of the atom-tracking system. The inset presents a zoom to the $x(t)$ curve, a positioning noise of about 50 pm is present. Simultaneously, the temperature at the sample stage is measured to drop from 302.91 K to 302.86 K by 50 mK over the total time of 75 min.

approximated linear drift velocity is found from a linear least-squares fit to about -117 pm/min, while the curvature is calculated from a quadratic least-squares fit to be about 1.18 pm/min^2. Predicting the long-term drift behaviour would be a simple task if these values were constant in time. This, however, is usually not the case even for small temperature changes. During this experiment, the temperature changes by a value as small as 50 mK measured at the sample stage[11]. Taking the simplicity of the drift model from Section 4.2 into account, these data are in very good agreement with the predicted drift behaviour. Especially, the predicted long-term exponential decay is directly apparent in these data for the X and Z channel.

From the root mean square dislocation noise in the data, a tip positioning precision better than 50 pm as marked in the inset of Figure 4.11 is found. The effective positioning precision is somewhat larger than the tip dislocation noise caused by the electronic circuitry. Most likely, this is a result of the large bandwidth settings for the lateral feedback loops and the poor input signal quality.

[11] A Si-diode mounted at the top of the sample stage inside the UHV system is read out with a Lakeshore 331 Temperature Controller (Lake Shore Cryotronics Inc, Westerville OH, USA).

The latter problem is addressed in hardware version 2, where the input signals for the feedback loops are of higher quality. The theoretical limit in tip positioning precision amounts to 8 pm in lateral and 2.6 pm in vertical direction, given by the single bit step of the output DACs.

4.5.5. Reproducible line-data acquisition

Besides the drift-free NC-AFM imaging, the atom-tracking technique can be employed to perform reproducible line-data acquisition. For this purpose, Abe *et al.* [2] described the following protocol: First, a surface species is tracked and the actual drift is compensated by means of the feedforward technique. In a second step, the tracking is paused and the tip is brought to the centre of the dithering circle. At this position, the recording of one $\Delta f(z)$ curve is triggered. The absolute tip position is well-defined for several seconds during this data sampling, because the actual drift is compensated by the feedforward technique. After finishing the data acquisition, the tracking is restarted and it recentres the tip excellently on the surface species. Simultaneously, it compensates for non-linear drift by updating the actual drift vector.

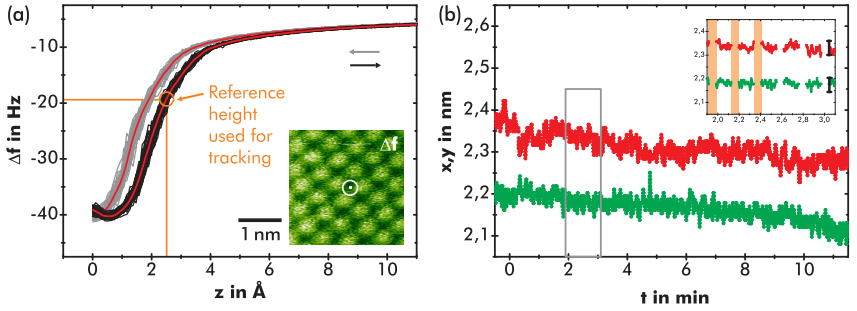

Figure 4.12.: Reproducible line-data acquisition on a $CaCO_3(10.4)$ surface. (a) A total of 51 $\Delta f(z)$ curves is acquired. The orange circle marks the reference height where the tracking and imaging is performed. Red curve: average of all 51 curves (raw data in black and grey). Inset: NC-AFM image with the white circle marking the dithering circle and a small white rectangle visualising the lateral extent of the 60 pm tip positioning noise. (b) Tip-positioning data from the $\Delta f(z)$ curves acquisition. Inset: zoom-in at the indicated position. The vertical bars have a length of 60 pm. Three orange rectangles identify three of the 51 data acquisition pauses, in which no tip-positioning data are available.

Figure 4.12 presents an example from a $CaCO_3(10.4)$ surface. In this experiment, a total of 51 curves is acquired. Each curve covers a range of 5.25 nm along Z (long-range part not shown) with a resolution of 500 pixel in both, forward and

backward direction. The total time per curve is 1 s. The data of the black curves in Figure 4.12(a) are sampled while moving the tip away from the sample, the grey curves represent the data while moving the tip towards the sample. A difference in between these curves, most likely caused by creep and hysteresis of the piezo scanner, manifests itself by a shift of about 60 pm of the $\Delta f(z)$ curves. For data analysis, always the forward $\Delta f(z)$ curves are used within this work.

Figure 4.12(b) shows the tip positioning data for the whole experiment. The feedforward parameters are updated before starting the data acquisition and, consequently, only small variations in the positioning data are apparent. Nevertheless, the used scan protocol compensates also for these subtle irregularities. From the positioning data, here a tip misplacement noise of 60 pm is estimated, which is consistent with the noise analysis in Section 4.5.4. To illustrate the smallness of this value, a rectangle with sidelengths of 60 pm is included centred in the dithering circle in Figure 4.12(a).

4.6. 3D data acquisition

In this section, I present the benefits emanating from the atom-tracking system in terms of high-resolution three-dimensional data acquisition. The first Section 4.6.1 describes a new 3D data acquisition protocol, capable of non-linear drift. This advanced protocol is demonstrated on a $CaCO_3(10.4)$ surface in Section 4.6.2. The last Section 4.6.3 briefly discusses the data post-processing, especially the conversion of the detuning data to the interaction force and potential.

4.6.1. Protocol for 3D data acquisition

The protocol employed for reproducible line data acquisition (described in Section 4.5.5) is extended to a new protocol for the acquisition of an entire 3D data set. The main extension is, that instead of choosing the centre position of the dithering circle for the $\Delta f(z)$ curve data acquisition, the tip is moved systematically to grid positions.

The timing for the different steps followed in this protocol are depicted in Figure 4.13(b). Additionally, the resulting tip trajectory is skizzed in Figure 4.13(a). In a first step, atom tracking is started and a single surface species is tracked for a short time span. From this tracking data, the actual linear drift in all three spatial directions can be obtained and compensated. However, this compensation is not capable of handling the non-linear drift present over a longer time span unless the precise drift behaviour is known – which is usually not the case. After the initial drift compensation, the 3D data acquisition procedure itself is started. Here, I discuss the sampling in form of $\Delta f(z)$ curves, but recording single images

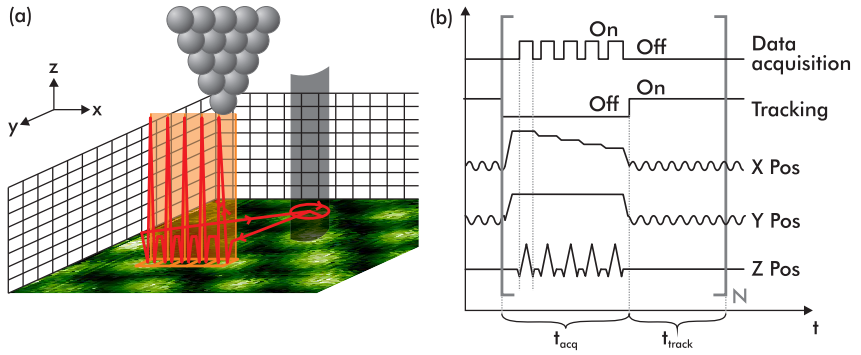

Figure 4.13.: New protocol for acquiring an entire 3D data set. The tracking position acts as the point of origin for the 3D data set. The tip always returnes to this point of origin in between data acquisition and, thus, refines the offset position. The timing diagram for this protocol is depicted in (b).

(or parts of it) is also possible. For each of the N data acquisition steps (one depicted by a bracket in Figure 4.13(b)), first the tracking is paused by stopping the lateral feedback loops and the tip dithering. The tip is brought to the centre of the dithering circle. At this time, the reference point of the tip is well-defined with respect to the previous tracking position and remains valid with highest precision for a short time interval. As the next step, $\Delta f(z)$ data is recorded systematically by relocating the tip to the desired grid position and executing the $\Delta f(z)$ curve measurement, which moves the tip in Z direction while sampling data. Several curves can be sampled during a single pause, however, the duration t_{acq} of data acquisition is limited as will be discussed later. To account for the non-linearity of the drift and the consequent tip misplacement, the absolute position needs to be redefined in a next step. Hence, the tip is moved back to the position where the tracking was paused and, at last, the tracking is restarted by dithering the tip and reactivating the feedback loops. During a time span of t_{track}, the tracking module perfectly centres the tip on the selected protrusion and, thus, non-linear drift contributions are automatically compensated for. The procedure is repeated N times until all data points are sampled.

Due to the non-linearity of the drift, an upper limit for the acquisition time t_{aqc} exists. I estimate this limit from the relation

$$r_{\mathrm{drift}}(t_{\mathrm{acq}}) - r_{\mathrm{drift}}(0) < \Delta g \tag{4.7}$$

where $r_{\mathrm{drift}}(t)$ is the misplacement at time t due to thermal drift and Δg is the desired positioning precision. With this equation, the total tip-sample misplacement occuring during the acquisition step is assumed to be smaller than Δg, a

quantity which can be chosen accordingly to the grid or surface unit cell size. Assuming a quadratic behaviour $r(t) = \frac{1}{2} a_{\mathrm{drift}} t^2$ with an acceleration a_{drift}, an upper limit for the acquisition time t_{acq} is found to:

$$t_{\mathrm{acq}} < \sqrt{\frac{2\Delta g}{a_{\mathrm{drift}}}} \tag{4.8}$$

With a desired precision of $\Delta g = 1\,\mathrm{pm}$ and a curvature of $a_{\mathrm{drift}} = 1\,\mathrm{pm/min^2}$, a maximum acquisition time of $t_{\mathrm{acq}} = 85\,\mathrm{s}$ would be possible until the tip is misplaced by more than the expected precision. However, this calculation is performed with the assumption of zero drift at $t = 0$. This can only be assured, if the drift vector for the feedforward module is updated frequently. The update interval t_{update} is also dependent on the curvature a_{drift}. To give an example, after 10 min the residual drift is in the order of $v_{\mathrm{drift}} = a_{\mathrm{drift}} \times 10\,\mathrm{min} = 10\,\mathrm{pm/min}$. Therefore, by defining a maximum tolerable drift v_{drift}, an upper limit for the update interval t_{update} is directly given.

Another constraint for the acquisition time t_{acq} arises from the feature dimension: During the complete experiment, the atom-tracking technique can only recentre the tip to the correct feature position, if the lateral displacement remains inside the operating regime. This regime is shaded blue in Figure 4.5.

4.6.2. Demonstration on Calcite

The new protocol was implemented in the atom-tracking system within this work by myself. Technically, it is necessary to synchronise the atom-tracking and feedforward system with the MATRIX scan controller. In the atom-tracking system I, therefore, extended the tracking module by a fast method to pause and resume the tip dithering. The relevant commands are send by the scan controller, synchronised with the line data acquisition. For the scan controller, the scripts are implemented by myself using the "MATRIX automated task environment" (MATE), a scripting language for advanced scan control in SPM experiments [147]. The post-processing of the data will be discussed in Section 4.6.3 and is implemented by myself in several MATLAB programmes.

A total of 7225 $\Delta f(z)$ curves are acquired on a grid of 85×85 pixel, having a lateral size of $1.74 \times 1.74\,\mathrm{nm^2}$ on the surface. In vertical direction, a total of 500 pixel along 2.18 nm are sampled per Z forward and backward tip movement, while the sampling time per point is chosen to 1 ms. A total of 17 curves are acquired during each acquisition interval of $t_{\mathrm{acq}} \sim 18.5\,\mathrm{s}$. The tracking is restarted for $t_{\mathrm{track}} = 5\,\mathrm{s}$ in between the acquision of 17 curves to recentre the tip at the point of origin. The tracking and acquisition steps are repeated $N = 425$ times during a total measurement time of about 3 h. For the tracking procedure, a surface depression is chosen while the dithering amplitude amounts to $A_{\mathrm{x,y}} = 1.2\,\text{Å}$ at a frequency of $f_{\mathrm{x,y}} = 20\,\mathrm{Hz}$. The tracking position is marked by a circle in Figure 4.15(e).

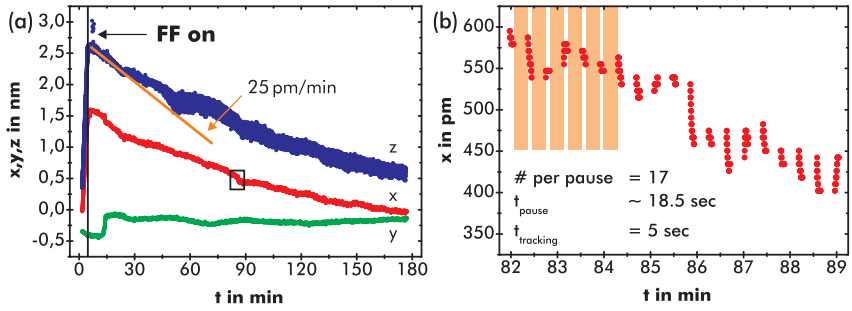

Figure 4.14.: Tip-positioning data from the 3D data acquisition. (a) After an initial drift measurement, the residual drift is at any time smaller than 25 pm/min. (b) zoom-in of the $x(t)$ data at the indicated box in (a). Some of the tracking pauses, in which line data are acquired, are shaded in orange.

Before discussing the Δf data itself, Figure 4.14 presents the tip-positioning data from the tracking system. From these data, the initial drift is found to be 525 pm/min, −23 pm/min and 754 pm/min in X, Y and Z direction, respectively, and initially compensated by the feedforward module. The origin for the drift might be thermal material relaxation, although the temperature gradient measured at the sample stage was as small as about 8 mK/h. During the experiment, drift velocities are optimized periodically to ensure residual drift velocities smaller than 25 pm/min. This parameter update is performed about every 15 min as this time span is expected to meet the requirement of the positioning precision as discussed before.

In Figure 4.15, different representations of the $85 \times 85 \times 500$ pixel data space are reproduced. With a 3D data set (Figure 4.15(a)) available, it is straightforward to extract lateral constant-height X-Y images at different Z positions (Figures 4.15(e) and (f)), vertical Y-Z (Figure 4.15(b)) or X-Z (Figure 4.15(c)) slices as well as $\Delta f(z)$ line data (Figure 4.15(d)). In all representations, $z = 0$ is arbitrarily set to the point of closest approach. This principle is followed throughout this work. The dithering circle is visualised by a circle in Figure 4.15(e). In this image, also tip changes are marked by white triangles. Although tip changes are usually most undesirable in AFM experiments, here they demonstrate the stability of the drift-compensation protocol.

Further analysis of these data is postponed to Chapter 5, where the calcite substrate itself is discussed. For this forthcoming analysis, only a subspace of the 3D data is used, which is assumed to be acquired with the same tip termination. The lateral extent of this data space is the upper half in Figure 4.15(e). To conserve an atomically sharp tip, it was refrained from acquiring Δf data up to the lower turning point of the $\Delta f(z)$ curve or even in the repulsive regime. In the AFM images

before and after the 3D data acquisition, an atomic-size defect was identified, indicating the existence of an atomically sharp AFM tip throughout the experiment.

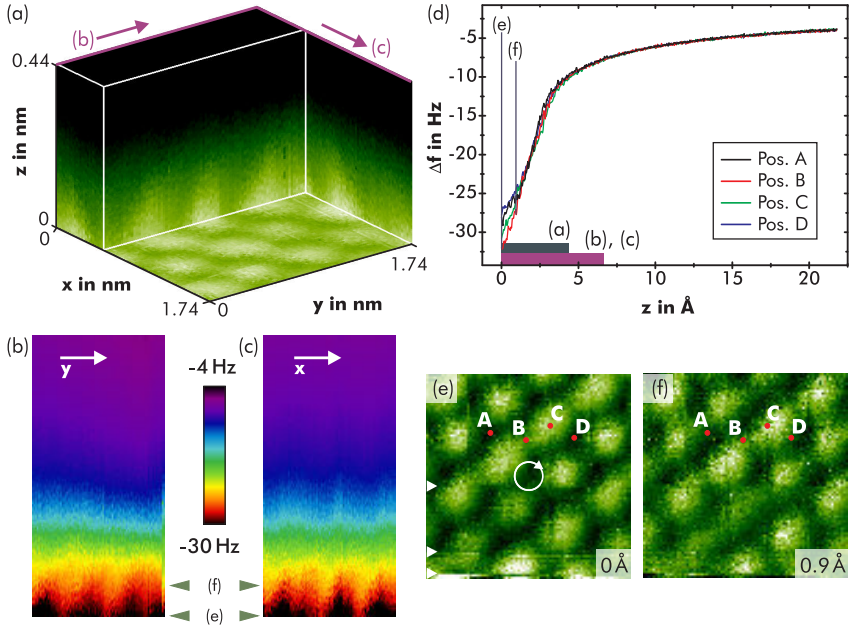

Figure 4.15.: Different representations of the $CaCO_3(10.4)$ results: (a) presents a cropped 3D view of the data acquired. Planes along different axes are extracted and presented in (b), (c), (e) and (f). Furthermore, it is possible to extract $\Delta f(z)$ curves from different surface sites as depicted in (d). The trajectory of the tip dithering is depicted in (e) as well as easy-to-identifyable tip changes by white triangles.

4.6.3. Post-processing

For the herein used experimental setup, the data are stored in form of $\Delta f(z)$ curves, encoded in the Omicron Nanotechnology MATRIX file format [159]. As the further processing is performed with MATLAB, the tool Vernissage [148] from Omicron Nanotechnology is employed to convert the raw data files to ASCII readable data. An initial MATLAB script `run_raw_load.m` loads these data into a matrix, on which all other MATLAB scripts operate.

For the conversion to force and potential, the formulae presented by Sader *et*

al. [177] are employed:

$$F(z) = \frac{2k}{f_0} \int_z^\infty \left(1 + \frac{\sqrt{A}}{8\sqrt{\pi(t-z)}}\right) \Delta f(t) - \frac{A^{3/2}}{\sqrt{2(t-z)}} \frac{\mathrm{d}\Delta f(t)}{\mathrm{d}t} \mathrm{d}t \tag{4.9}$$

$$U(z) = \frac{2k}{f_0} \int_z^\infty \Delta f(t) \left((t-z) + \frac{\sqrt{A}}{4}\sqrt{\frac{t-z}{\pi}} + \frac{A^{3/2}}{\sqrt{2(t-z)}}\right) \mathrm{d}t \tag{4.10}$$

These formulae are converted into a discretised formulation and are implemented in MATLAB scripts.

For a reliable usage of formulae 4.9 and 4.10, it is necessary to use $\Delta f(z)$ data with a Z-range larger than twice the cantilever oscillation amplitude or a Z-range, where the frequency shift Δf is virtually zero at maximum Z. The interaction in the long-range regime is usually assumed to be site-unspecific. Consequently, only one $\Delta f(z)$ curve from a single position is acquired over a larger Z range, and is mended to the high-resolution short range data.

For the long-range curve acquisition, the strategy described in Section 4.5.5 is employed. A total of 20 $\Delta f(z)$ curves are sampled directly after finishing the 3D data acquisition. Each curve spans a Z range of 20.18 nm. The oscillation amplitude in these experiment is (13.6 ± 0.1) nm, the peak-peak distance is therefore slightly larger compared to the covered $\Delta f(z)$ distance regime. However, the Δf values are zero within the experimental noise at maximum Z and, thus, the usage of Equations 4.9 and 4.10 is justified. The averaged long-range curve from this experiment is presented in black in Figure 4.16(a).

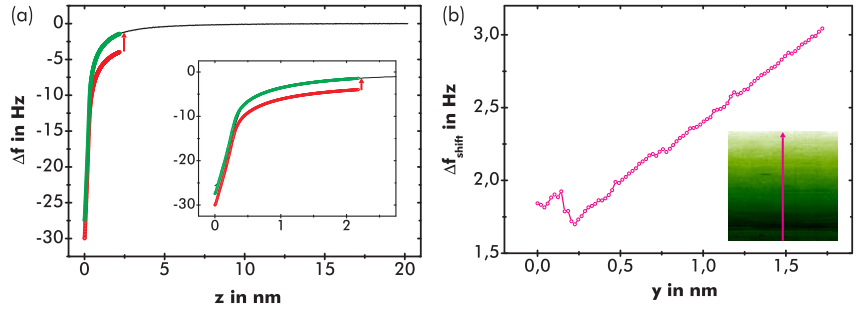

Figure 4.16.: (a) Short-range data (one $\Delta f(z)$ curve exemplary in red) are joined with the long-range $\Delta f(z)$ curve (black) by shifting the short-range data along the Δf axis (result in green). (b) The shift for each curve is mapped to the lateral grid positions in the inset, while the graph denotes the linewise average curve.

This long-range curve is joined with the short-range data by shifting each short-range curve (one exemplary depicted in red) along the Δf axis. The criterion for

each shift is the minimum deviation of ∼ 100 outmost points of the short-range with the long-range data. The resulting short-range curve for the former example is depicted green in Figure 4.16(a). The shift is calculated specific for each of the 7225 $\Delta f(z)$ curves. For each curve, this shift is represented in the inset of Figure 4.16(b), while the according graph presents the linewise averaged shift. From this data, thermal drift of the resonance frequency is found to ∼ 0.5 Hz/h. This drift is most likely induced by a temperature change in the cantilever material. For rectangular silicon cantilevers, Giessibl [68] has calculated the relative frequency shift due to temperature variations to $-5.8 \times 10^{-5}\,\mathrm{K}^{-1}$. Using this value, a temperature shift of −86 mK at the cantilever beam is found for this experiment.

Two aspects about this data processing should clearly be mentioned. They fully justify this procedure: First, my approach does not shift data along any of the three spatial directions, it only adds offsets to the Δf data itself. Thus, it does not include any assumption on the sample system such as other processing strategies [6]. Second, the resulting correction curve in Figure 4.16(b) is excellently linear[12] and, therefore, in full agreement to a thermal shift of the resonance frequency f_0.

The usage of Equations 4.9 and 4.10 requires the knowledge of the spring constant k, the resonance frequency f_0 and the physical amplitude A of the cantilever. The resonance frequency f_0 is measured with highest precision by the PLL. For this experiment, it is determined to $f_0 = 303\,950$ Hz. The amplitude A is obtained by a method known as the "constant normalised frequency shift mode" reported by Simon *et al.* [191]. Here, the result is $A = (13.6 \pm 0.1)$ nm. The spring constant k is given by the datasheet of the manufacturer to $k = (35 \pm 11)$ N/m. It is calculated from the geometric cantilever dimensions [137]. This value is expected to be correct within an error of 30 % [125]. A determination using the thermal method is expected to yield a smaller error, however, no suitable spectrum analysator was available during this experiment. Details on different strategies to determine k will be available in future in Reference [126].

The calculated force and interaction potential are linear related to k and f_0. Thus, a systematic error in their determination only globally scales the force and potential, but the relative differences in one 3D data set remain unaltered.

4.7. Conclusions

Within this chapter, I presented a newly developed, most flexible atom-tracking system. This system features an absolute tip positioning with a lateral precision of at least 50 pm. It allows for data acquisition with the distance feedback loop

[12] The steps at $y \sim 0.2$ nm are caused by tip instabilities.

deactivated in either line data (1D), constant height imaging (2D) or volume data (3D) mode. Second, a new protocol for the 3D volume data acquisition despite the presence of severe drift was developed and implemented. This protocol is capable of large non-linear drift and allows, for the first time, dense 3D data acquisition at room-temperature. An example on a $CaCO_3$ surface at the atomic scale was given, with the resulting data space having a size of $85 \times 85 \times 500$ pixel. The data acquisition was performed under large drift conditions over a timespan of 3 h.

5. The calcite (10.4) surface

Calcium carbonate ($CaCO_3$) is one of the most abundant simple salts in nature. It is found in the shells of molluscs such as slugs or sea shells, where it forms the predominant phase. Especially calcite, the most stable polymorph of $CaCO_3$, combines with organic material to an organic/inorganic mixture, forming materials with both, outstanding material properties and amazing elegancy. These *biominerals*, which are formed in the process of *biomineralisation*, were the focus in a large number of studies during the last decades. The motivation is to understand, imitate and control the formation process [4]. Especially understanding the interaction of the inorganic calcium carbonate phase with organic molecules is of utmost importance. This interaction has been investigated by means of experimental studies as well as theoretical modelling [149, 50]. Besides this important aspect of biomineralisation, calcium carbonate is used in many industrial products such as paints, paper chemicals, cement as well as cosmetics and pharmaceuticals [43]. Due to its birefringence [70] it is furthermore present in optical devices [90]. In contrast, calcite precipitation upon scaling is usually undesired in industrial and daily life applications such as water desalination and laundry and often avoided by addition of suitable polyelectrolytes [167, 82]. Besides these application-oriented aspects, calcium carbonate is discussed as a possible origin for the homochirality of life [5]. This suspect is evident from studies, where the adsorption of amino acids has been demonstrated to be enantiospecific [85] and, furthermore, to influence enantiospecific the macroscopic growth [149].

In this chapter, first the bulk and (10.4) surface properties will be critically reviewed. For the surface properties, the focus will be on the current understanding and controversy of surface reconstructions and symmetry properties. In a second part, the contrast formation in NC-AFM data will be classified and related to the surface properties.

5.1. Bulk properties

Calcite is the most stable polymorph of calcium carbonate ($CaCO_3$). It crystallises in a trigonal crystal system (rhombohedral holohedral $\bar{3}2/m$) and its symmetry is described by the space group $R\bar{3}c$ [166]. Two more modifications of $CaCO_3$ have been found in nature [45]: Aragonite and vaterite. Aragonite, which exhibits a orthorhombic crystal structure described by the space group *Pmcn*, is thermo-

dynamically unstable and alters on the timescale of centuries to calcite. The second metastable phase, vaterite, forms a hexagonal crystal system described by the space group $P6_3/mmc$ and converts much more rapidly to calcite or aragonite. Therefore, its occurance in nature is scarce. Additionally, at least five synthetic modifications are known transforming at high pressure and/or high temperature: Calcite I to V. A pressure-temperature phase diagram has been presented by Mirwald *et al.* [136].

$CaCO_3$ is composed of calcium ions and carbonate (CO_3) groups. Inside each carbonate group, covalent bonds are formed between the carbon and oxygen atoms. The bond formation between each carbonate group with the surrounding calcium atoms is of strong ionic character. Usually, the charge states of the different elements are characterised as Ca^{2+} and CO_3^{2-}. [192]

Calcite exhibits a trigonal crystal system, the unit cell is a rhombohedron with side length $a_{\mathrm{rh}} = 6.375\,\text{Å}$ and interaxial angle $\alpha_{\mathrm{rh}} = 46.08°$ [166, 45]. This is the primitive unit cell, usually named *structural* or *acute* unit cell. Often, the hexagonal representation of this unit cell with sides of length $a_{\mathrm{hex}} = 4.9896\,\text{Å}$ and $c_{\mathrm{hex}} = 17.0610\,\text{Å}$ is chosen in literature, where the most stable cleavage plane is denoted the (10.4) surface. This hexagonal unit cell including the relation to the rhombohedral cell is depicted in Figure 5.1.

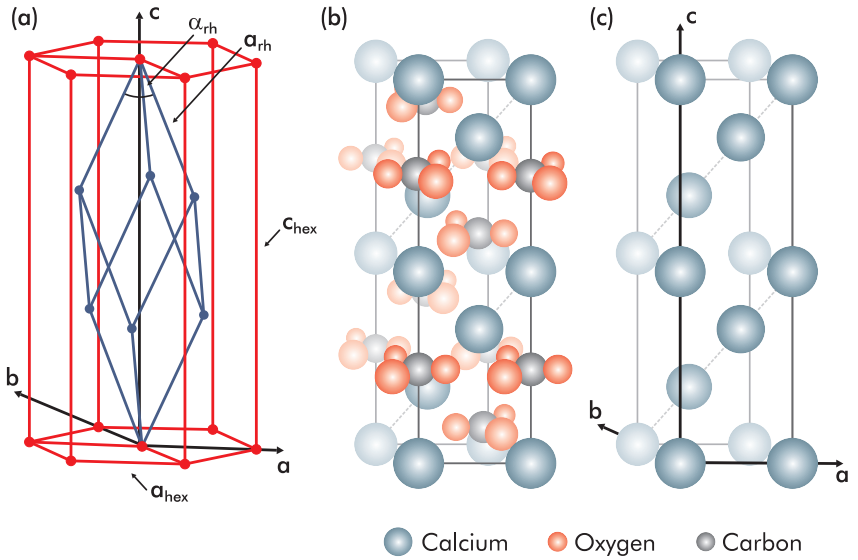

Figure 5.1.: (a) Relation of the rhombohedral (blue) to the hexagonal (red) *structural* unit cell. The hexagonal unit cell is depicted in (b) and (c), while only the Ca sublattice is presented in (c) for visualisation purposes.

Two more unit cells are present in literature, causing confusion in naming bulk directions and surface planes. Winchell [222] suggested in 1965 that this confusion is originated in the initial description of the calcite structure by Bragg in 1914 [31, 30], where a comparison to a halite structure results in a rhombohedral calcite unit cell with side length $a_{\mathrm{rh,pseudo}} = 6.42\,\text{Å}$ and interaxial angle $\alpha_{\mathrm{rh,pseudo}} = 101.55°$. This unit cell is not a true bulk unit cell, as it does not account for the different orientations of the CO_3 groups. After realising this mistake, a *morphological* rhombohedral unit cell has been proposed in literature, where the side length of the pseudo unit cell is doubled to $a_{\mathrm{rh,morph}} = 12.85\,\text{Å}$. This rhombohedral unit cell nicely describes the macroscopic crystal shape terminated by the most stable crystal planes, in this system denoted as $(100)_{\mathrm{morph}}$. Both of these unit cells can be expressed in terms of hexagonal coordinates, which makes a total of six different descriptions in literature as summarised in Table 5.1. The relation of the rhombohedral unit cells to each other is depicted in Figure 5.2.

	structural	pseudo	morphological
Rhombohedral axes			
a_{rh}	6.38 Å	6.42 Å	12.85 Å
α_{rh}	46.08°	101.92°	101.92°
most stable plane	(211)	(100)	(100)
Hexagonal axes			
a_{hex}	4.99 Å	9.98 Å	19.96 Å
c_{hex}	17.06 Å	8.53 Å	17.06 Å
most stable plane	$(10\bar{1}4)$	$(10\bar{1}1)$	$(10\bar{1}1)$

Table 5.1.: Dimensions for the different unit cells used to describe the calcite crystal structure. Values are taken from Refs. [166, 45, 51]. The relevant description for this work is shaded in grey.

In this work, exclusively the *structural hexagonal* unit cell will be used. This hexagonal unit cell is depicted in Figures 5.1(b) and (c). The unit cell sizes have, besides others, been determined by Effenberger *et al.* [51] using X-ray diffractometry and will be used herein. The unit cell vectors $\vec{a}_{\mathrm{hex}}, \vec{b}_{\mathrm{hex}}$ and $\vec{c}_{\mathrm{hex}}$ are oriented along the [10.0], [01.0] and [00.1] crystal axes of the hexagonal system, respectively[1], and the most stable cleavage plane is identified as (10.4).

Calcite is a fairly wide gap insulator with an experimentally determined bandgap of $E_g = 6.0\,\text{eV}$ [13]. It is, therefore, transparent in the visual regime and the onset of optical absorption has been determined to about 214 nm ($\sim 5.9\,\text{eV}$) [25].

[1] The four-symbol Miller-Bravais indices $[hkil]$ are used, leaving no doubt about the crystal system. However, the index $i = -h - k$ is usually abbreviated by a dot in this work.

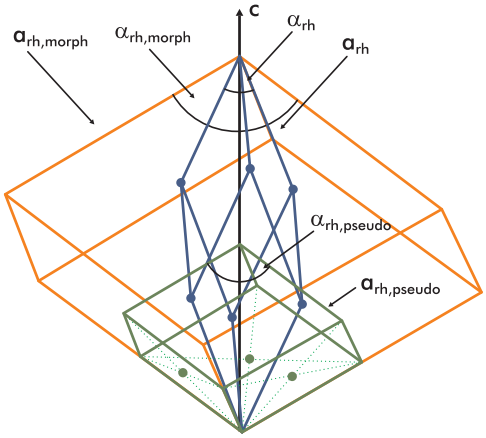

Figure 5.2.: Relation of the rhombohedral unit cells to each other: *structural* unit cell depicted in blue, *pseudo* unit cell in green and *morphological* unit cell in orange.

Calcite is well-known for its intense birefringence [70] with the refractive indices and the static relative permittivities for optical main axes given in Table 5.2.

Electronic properties			
band gap	E_g	6.0 eV	Ref. [13]
Refractive indices (at $\lambda = 590$ nm)			
ordinary ray	n_o	1.658	Ref. [219]
extraordinary ray	n_e	1.486	Ref. [219]
Static relative permittivities (at 25 °C)			
$\vec{E}$ parallel to $\vec{c}$	$\epsilon_{\parallel}$	7.8	Ref. [165]
$\vec{E}$ perpendicular to $\vec{c}$	$\epsilon_{\perp}$	8.2	Ref. [165]

Table 5.2.: Various material constants for calcite $CaCO_3$.

5.2. The (10.4) surface

The most stable cleavage plane of calcite is the (10.4) surface. Cleaving a bulk calcite crystal along this plane, the fewest Ca–O bonds are broken [105]. To my best knowledge, no surface has been reported upon which formation C–O bonds are broken. The surface energy is calculated to 590 mJ/m^2 [105] and is smallest compared to other calcite crystal surfaces [103]. Furthermore, the surface has a non-polar character as the same number of ions is present on this cleavage plane.

Within the (10.4) surface both, calcium atoms and carbonate groups form a rectangular unit cell with dimensions of 4.99×8.10 Å^2. These dimensions are cal-

culated from the crystallographic bulk data and have been confirmed by early LEED [197] and AFM [158] experiments within the experimental error. The unit cell vectors $\vec{a}$ and $\vec{b}$ of the surface unit cell are oriented along the [01.0] and [$\overline{42}$.1] crystallographic directions, respectively. A graphical representation of the truncated bulk structure is given in Figure 5.3.

If the surface unit cell is arranged with the rectangular calcium sublattice, two carbonate (CO_3) groups are located within the unit cell. In the truncated bulk structure, the carbon atom of each CO_3 group is perfectly centred along [01.0] in the surface unit cell and both carbon atoms lie equally spaced along [$\overline{42}$.1]. Both groups are rotated by 44.63° with respect to the surface plane such that one of the three oxygen atoms protrudes the plane, one lies in the plane and one is beneath the plane. The vertical distance of each oxygen atom to the surface plane amounts to 0.78 Å, calculated from a C–O distance of (1.2815 ± 0.0006) Å as determined by Effenberger *et al.* [51]. Furthermore, the two carbonate groups inside one surface unit cell are rotated with respect to each other by 180°, thus the upmost oxygen atom points either to the left or to the right. Following the position of these protruding oxygen atoms, a zig-zag line becomes apparent and is included in Figure 5.3. The amplitude of this zig-zag line is calculated accordingly to 0.64 Å.

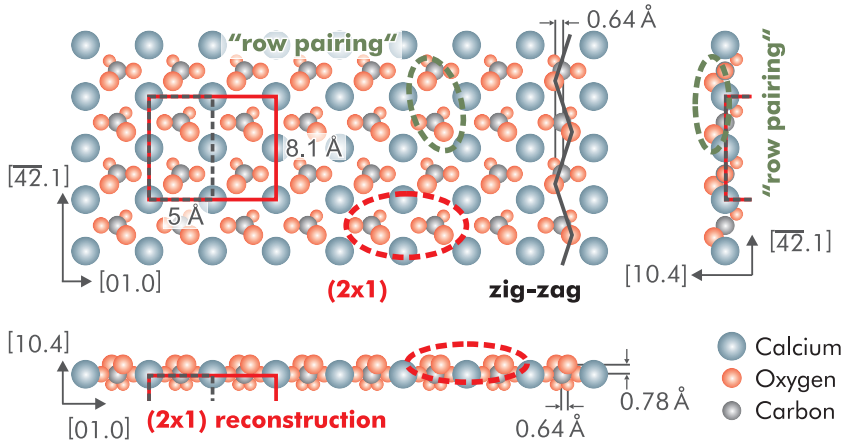

Figure 5.3.: Bulk truncated structure of the calcite (10.4) surface including projections along the [10.4], [01.0] and [$\overline{42}$.1] direction. The unit cell as well as several surface characteristics (discussed later) are included.

The monomolecular step height is calculated to 3.0356 Å. Due to the calcite crystal structure, a shift of the surface unit cell of 2.495 Å along [01.0] and 3.075 Å along [$\overline{42}$.1] is present comparing monomolecular layers n with $n-1$, as visualised in Figure 5.4. Due to the rhombohedral crystal structure, two types of step

edges are present on the $CaCO_3$(10.4) surface. They are named *obtuse* and *acute*, according to the angle the front atoms draw with the crystal. This is indicated by a dash-dotted green line in Figure 5.4(a).

The energetics upon step-edge and kink-site formation has been investigated by means of theoretical calculations by Kristensen *et al.* [105]. Steps along the $[\overline{4}4.1]$ and $[\overline{4}8.1]$ direction, which intersect the (10.4) plane forming a rhombohedron, are expected to be the predominant steps [105]. Along these steps, alternating CO_3 groups and Ca atoms are present, however, the calculations point to intense relaxation processes especially for the obtuse step. The step directions and several high-symmetry directions are depicted in Figure 5.4.

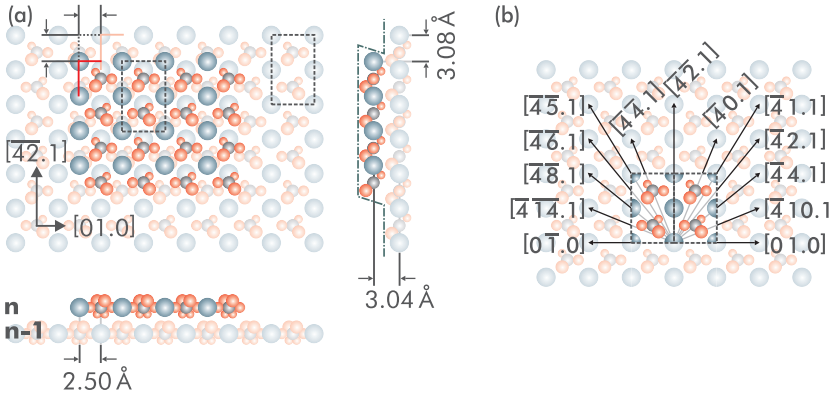

Figure 5.4.: (a) Monomolecular layers on a calcite (10.4) surface. (b) Various high-symmetry directions for the calcite (10.4) surface.

Table 5.3 summarises all bulk-truncated surface dimensions relevant for this work. All values are calculated from the crystallographic bulk values and the C–O distance determined by Effenberger *et al.* [51].

5.3. Surface reconstructions

For the calcite (10.4) surface, early AFM and LEED experiments witnessed two reconstructions, the first named *row-pairing* and the second identified as a (2×1) reconstruction [197, 158].

The row-pairing has first been reported by Rachlin *et al.* [158] in 1992 from contact AFM data. Amongst others, it has been confirmed in consecutive experiments by Stipp *et al.* [198], Jin *et al.* [96], Rode *et al.* [169] and Schütte *et al.* [185]. It is characterised either by a pairing or an apparent height difference of two spots aligned along the $[\overline{4}2.1]$ direction *inside* the surface unit cell. This pairing breaks

Unit cell (bulk truncated)		
$\vec{a} = [01.0]$	a	4.9896 Å
$\vec{b} = [\overline{42}.1]$	b	8.0955 Å
Carbonate groups (using Ref. [51])		
C-O distance	$d_{\text{C-O}}$	(1.2815 ± 0.0006) Å
angle to plane	α_{CO_3}	44.63°
O-plane distance	$d_{\text{O-plane}}$	0.7797 Å
zig-zag amplitude	$A_{\text{zig-zag}}$	0.6408 Å
Step edges		
monomol. height	h_{mono}	3.0356 Å
hex. unit cell height	h_{unitcell}	12.1422 Å $(4 \times h_{\text{mono}})$
shift along [01.0]	$s_{[01.0]}$	2.4948 Å
shift along $[\overline{42}.1]$	$s_{[\overline{42}.1]}$	3.0753 Å

Table 5.3.: Various surface dimensions for the calcite (10.4) surface.

a symmetry element on the surface as will be discussed in the next section.
In contrast, the (2×1) reconstruction, first observed by Stipp *et al.* [197] in 1991, leads to a supercell with double length along the [01.0] direction. This effect, though controversly discussed in literature [169, 185, 158, 105, 170, 117], is nowadays accounted to be a true surface property. The physical origin for this reconstruction is still unclear. Both reconstructions and their current understanding are depicted in in Figure 5.5.

The orientation of the upmost oxygen atom changes with every next CO_3 group along the $[\overline{42}.1]$ direction. The centre positions of the oxygen atoms consequently form a zig-zag line along this substrate direction with an amplitude of 0.64 Å. Interestingly, based on AFM data, values in the range of 0.35 Å to 1.05 Å have been reported in literature [117]. Additionally to this zig-zag observation, a pronounced height difference along the $[\overline{42}.1]$ direction, referred to as *row-pairing*, has been observed in experimental AFM studies. When considering the bulk truncated structure, however, all upmost oxygen atoms would exhibit the same distance of 0.78 Å to the plane spanned by carbon and calcium atoms. The observed height difference, therefore, seems not to be explainable by the different oxygen orientations alone and might point to an additional reconstruction process.
A possible explanation for the observed height difference has been given by Jin *et al.* [96]. They have proposed a rotation of every second CO_3 group. The angle of this rotation has been calculated by geometric means from the apparent height in contact AFM data to a value of $(35 \pm 5)°$. However, I would like to stress the ambiguity in measuring heights on the atomic scale. For the NC-AFM I will present

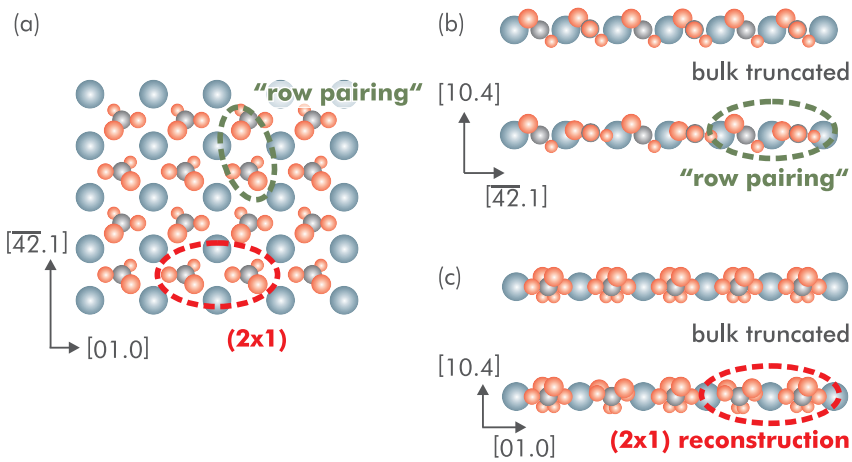

Figure 5.5.: Reconstructions on the $CaCO_3(10.4)$ surface (a): (b) row-pairing and (c) (2×1) reconstruction. The row-pairing is depicted following the model proposed by Jin *et al.* [96], while the (2×1) reconstruction is drawn according to recent calculations by J. Gale [65].

later that the measured "height" strongly depends on the interaction regime. Additionally, Foster *et al.* [63] have discussed relaxation processes occuring in presence of an AFM tip. They have concluded that the displacement of the upmost oxygen atom is up to 0.45 Å for a tip scanned at constant height. Due to these arguments, the calculated rotation angle by Jin *et al.* [96] should not be taken literally. A visualisation of this rotation according to the model by Jin *et al.* [96] is given in Figure 5.5(b).

The existence of the second effect, the (2×1) reconstruction, is controversially discussed in literature after initial LEED experiments by Stipp *et al.* [197], because subsequent contact AFM experiments did not reveal its existence [158, 169]. For the NC-AFM technique, Schütte *et al.* [185] first pointed out that the visibility of the (2×1) reconstruction might depend on the imaging conditions by presenting quasi constant-height images. This mechanism will be further analysed in Section 5.6.
The physical origin for this reconstruction is still under debate. In 2003, Rohl *et al.* [170] have presented *ab-initio* calculations which included evidence for a (2×1) reconstruction. The existence has been deduced from "the presence of an imaginary phonon mode at $(\frac{1}{2},0)$ in the 2D Brillouin zone for a single surface cell" [170] and in the same study, the exothermic energy change upon forming has been calculated to 0.003 eV. Furthermore, they pointed out that previous calculation

might not have been able to resolve the reconstruction. A second explanation has been proposed by Kristensen *et al.* [105] in 2004, where steps and kink sites have been analysed by means of numerical calculations. Modelling the reorientation of carbonate groups at the most prominent $[\bar{4}4.1]$ and $[\overline{48}.1]$ step edges, an influence on the orientation of carbonate groups on the terraces next to the step edges have been discussed as the origin for the (2×1) reconstruction. However, they identified this effect to be neglegtible at terrace sizes of larger than 4.5 nm.

5.4. Symmetry and chirality

The (10.4) surface of calcite is described by a rectangular surface unit cell with a basis of two calcium atoms and two rotated CO_3 groups. The plane symmetry group for this surface is *pg* [84, 113]. This primitive group contains only glide reflections. A glide reflection is a combination of a reflection with respect to a given line and a translation along that line. For $CaCO_3$(10.4), a glide reflection with the line oriented along the $[\overline{42}.1]$ substrate direction and a shift of $a/2$ is found as an isomorphism for the surface structure. This is depicted in Figure 5.6. This isomorphism is still valid for a (2×1) surface reconstruction.

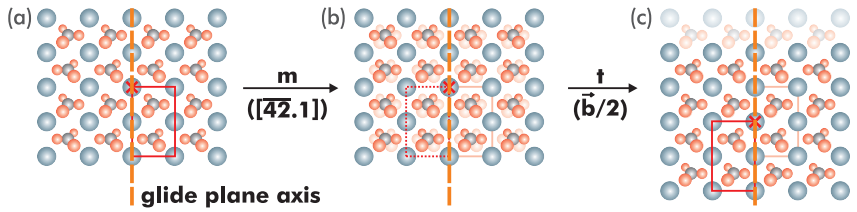

Figure 5.6.: Glide reflection on the $CaCO_3$(10.4) surface. (a) The initial configuration with the glide axis (orange). (b) The mirrored structure, (c) the structure translated by $b/2$ along the glide axis. The latter structure is isomorph to the initial structure.

The glide reflection axis is a symmetry element of the second kind and, thus, the $CaCO_3$(10.4) is an achiral surface according to the IUPAC definition [132]. Interestingly, the symmetry is broken when considering the row-pairing. With the assumption that the row-pairing is an effect present along one row parallel to the [01.0] direction, let it be a rotation of the CO_3 groups as proposed by Jin *et al.* [96] or any other structural or electronic reconfiguration, the glide reflection is no longer an isomorphism for this surface. This is depicted in Figure 5.7, where the row-pairing is simply visualised as a blue colored row. After the glide plane operation, the position and orientation of the blue carbonate groups is different compared to the initial structure. Thus, the glide reflection is no longer an isomorphism for the reconstructed surface. As, additionally, no other symme-

try operations of the second kind are found for this reconstructed surface, the $CaCO_3$(10.4) is now a chiral surface. The two enantiomers named R and S are depicted in Figures 5.7(d) and (e).

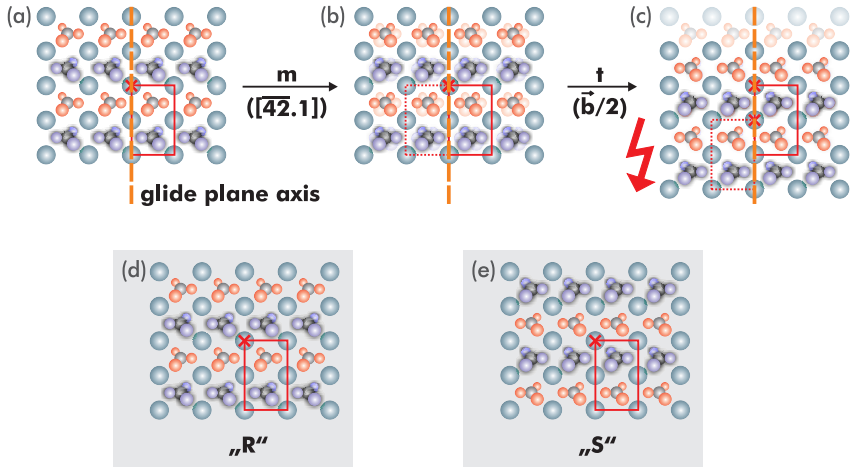

Figure 5.7.: Glide reflection for the $CaCO_3$(10.4) surface with row-pairing: the glide reflection (a) to (c) is no longer an isomorphism for the surface structure. Two enantiomers (d) and (e) are found. The row-pairing is simply visualised by a blue colored and shaded row.

This finding is quite surprising and in controversy to the current literature understanding. Currently, the $CaCO_3$(10.4) surface is accounted as an achiral surface [84, 113], which is in agreement with the bulk-truncated structure. In contrast, the row-pairing itself has been observed experimentally by means of AFM before, but the implications for the surface chirality has, to my best knowledge, not been deduced so far.

The identification of the enantiomers by means of NC-AFM is possible by resolving both, the row-pairing and the zig-zag, at the atomic level. From these data, the type of enantiomer can be identified unambiguously. This strategy will be presented for one enantiomer in Section 5.6, however, the unambiguous identification of both enantiomers was not succeessful within this work.

In conclusion, this finding leaves only two possibilities for the row-pairing reconstruction: Either the experimentally observed row-pairing originates from a scanning artifact, which has not been realised in literature, or the calcite surface truly reconstructs to a chiral surface. The latter finding has so far not been discussed in literature, but it could explain some literature controversy about the enantiospecific adsorption of amino acids [223, 113, 121].

5.5. Identification of the surface orientation by optical means

The identification of the *absolute* surface orientation, herein considered as the absolute orientation of the [01.0] and [$\overline{42}$.1] surface directions, is of utmost importance when investigating the surface properties.

The identification of the herein named *general* orientation, which leaves the orientation of the CO_3 groups unknown, is usually performed by analysing AFM data in consideration of the scanner calibration and thermal drift. This procedure is visualised in Figures 5.8(a) to (d), where AFM topography data with atomic resolution is presented. The scanner is carefully calibrated at the atomic scale, using the atomic lattices on TiO_2(110) and Si(111). The two-dimensional Fourier transformation (2D-FT) for both images are given in Figures 5.8(c) to (d) and the $CaCO_3$(10.4) unit cell dimensions are directly revealed within the experimental error. The average of two values originating from consecutive AFM images with a different orientation of the slow scan axis is a good measure for compensating for linear thermal drift [160]:

$$\overline{a} = (5.05 \pm 0.20)\text{Å} \tag{5.1}$$

$$\overline{b} = (8.15 \pm 0.40)\text{Å} \tag{5.2}$$

From this analysis, however, the orientation of the carbonate groups cannot be identified and, thus, the *absolute* sample orientation is unknown. Although an identification of the carbonate group orientation will be suggested by high-resolution data in Section 5.6.6, currently, the unambiguous identification remains unclear.

Fortunately, another strategy supported by the birefringence properties can be followed. In Appendix Section D, the Poynting vector $\vec{S}_o$ ($\vec{S}_{ex}$) for the ordinary (extraordinary) ray, respectively, is calculated for the case of light rays passing perpendicular the (10.4) surface. After passing a crystal of thickness t, the extraordinary ray is found to be misplaced by

$$d = \frac{2\sqrt{3}\,a\,c\,t(\epsilon_1 - \epsilon_3)}{12a^2\epsilon_3 + c^2\epsilon_1} \tag{5.3}$$

$$\sim 0.87\,\text{mm}. \tag{5.4}$$

with a, c: $CaCO_3$(10.4) unit cell dimensions, ϵ_1, ϵ_3: relative dielectric permittivities for the visual regime. The numerical value is calculated for $t = 8\,\text{mm}$. Most importantly, this split occures along the [42.$\overline{1}$] crystal direction when projected into the (10.4) plane. Furthermore, if the split is defined as the vector $\vec{p}$ from the ordinary to the extraordinary ray at their points of intersection with the (10.4) surface plane, $\vec{p}$ points into the same direction as the [42.$\overline{1}$] direction. Thus, from de-

termining vector $\vec{p}$ it is unambiguously possible to determine the *absolute* sample directions and, thus, the orientation of the CO_3 groups.

Figures 5.8(f) to (h) present three photographic images (topview on the (10.4) surface) taken of a calcite sample inside the sample holder. The clamping L of the sample holder is removed. Beneath the sample, a paper stripe with a printed plus

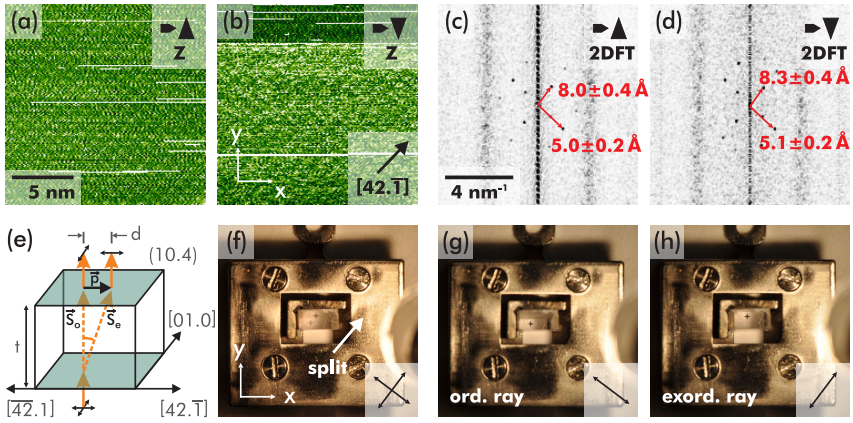

Figure 5.8.: Relating the birefringence properties with the surface properties: (a) and (b) are consecutive topography NC-AFM images, (c) and (d) their 2D-FT, respectively. (f) to (h) are photographic pictures, (g) and (h) taken using a linear polarising filter with the transmission direction given in the lower right inset. The split vector $\vec{p}$ points along the $[42.\bar{1}]$ crystal direction and, therefore, allows for an unambiguous sample orientation identification ((a) and (b) courtesy of [Name removed]).

symbol is placed such that both images produced by the ordinary and extraordinary ray are visible in the picture. Figures 5.8(g) and (h) are pictures taken with a linear polarising filter in front of the camera lens, the transmission direction of this filter is denoted in the lower right corner. The ordinary ray in Figure 5.8(g) is linearly polarised perpendicular to the birefringence split, while for the extraordinary ray in Figure 5.8(h), the polarisation direction is oriented parallel to the split.

The split vector $\vec{p}$, which points along the $[42.\bar{1}]$ direction, is determined from the crossing points of the ordinary and the extraordinary ray with the (10.4) surface plane. As the scanner coordinate system is oriented as indicated in Figures 5.8(b) and (f), the absolute sample orientation in the NC-AFM experiments can unambiguously be determined by optical means.

This relation, to my best knowledge here presented for the first time for the (10.4) surface, elegantly allows to find the *absolute* crystal orientation by optical means. The *absolute* crystal orientation includes the orientation of the carbonate

groups. This identification is of utmost help, as the different NC-AFM contrasts hinder unambiguous assignment of the absolute orientations from the NC-AFM data. From these data, only the *general* orientation of the crystal without the CO_3 group orientation is usually determined by measuring the unit cell sizes.

Unfortunately, the absolute orientation has not been identified by this optical strategy for a large number of samples within this work. In the majority of cases, atomically resolved AFM data are used to identify the *general* orientation. In the following, this fact will be accounted for by depicting two arrows at each end of the [01.0] direction vector in the NC-AFM data.

5.6. NC-AFM study of the calcite (10.4) surface

The $CaCO_3$(10.4) surface has, to my best knowledge, so far only been investigated twice by means of NC-AFM under ultra-high vacuum conditions, namely in a first study by C. Barth [15, 61] in 2002 and in a second study by J. Schütte [184, 185] in 2009. Barth has been the first to image the $CaCO_3$(10.4) surface with atomic resolution under ultra-high vacuum conditions. He assumed that the bright species in the frequency shift (Δf) channel represent the positions of the topmost oxygen atoms of the CO_3 groups. Furthermore, he has investigated the imaging in a quasi constant-height mode under different scan angles. From one image series, where the scan angle was systematically changed from 0° to 360° in steps of 20° or 30°, different contrast modes for different scan angles have been observed. It has been suggested that these different contrast modes are induced by scan-direction dependent surface relaxation processes. Foster *et al.* [63] have investigated the surface relaxation in presence of an Si and MgO AFM tip by means of *ab-initio* calculations. Depending on the applied tip potential and the microscopic tip termination, they have found an intense in- or outward relaxation of the CO_3 groups. The Ca atoms are observed to displace in roughly opposite direction. However, the observed contrast modes have not been classified in the study by Barth. Additionally, all images have been highly distorted by thermal drift with the unit cell sizes deviating up to a relative error of 20 % and the residual Z movement has not been indicated.

Especially the last point is crucial, as obvious from the second study by J. Schütte [184, 185]. Based on quasi constant-height images with negligible Z movement, J. Schütte has investigated the distance dependence in the NC-AFM contrast formation. In particular, his data presented a severe distance dependence for the visibility of the (2×1) reconstruction, where changes of the Δf setpoint[2] in the order of 1 Hz have resulted in most different contrasts. Unfortunately, the ap-

[2] At a cantilever oscillation amplitude $A \sim 10\,\text{nm}$ and resonance frequency $f_0 \sim 300\,\text{kHz}$.

proach of quasi constant-height images does neither provide absolute tip-sample distances of the contrast regimes, nor does it usually cover the full interaction regime.

Within this section, I propose a systematic classification scheme for the observed contrasts in Section 5.6.2 and relate the contrasts to surface properties. The distance dependence in contrast formation is investigated in Section 5.6.3, based on a 3D data set and true constant-height images. One striking example for a tip reconfiguration is analysed in Section 5.6.4. Section 5.6.5 discusses the imaging contrast in the repulsive regime and in the last Section 5.6.6, an identification of the absolute surface orientation is proposed, which is deduced from the NC-AFM contrast formation upon imaging the CO_3 groups.

5.6.1. Specific methods

All following data are acquired with the FM NC-AFM technique, using the line, image or 3D mode. In all modes, the frequency shift Δf is the main measurement channel. In the raster mode, often the true constant-height mode is employed to exclude feedback-loop artifacts. For the quasi constant-height data, the residual Z-movement is given in terms of the FWHM[3] of a Gauss distribution fitted to the height distribution. This method will exemplarily be presented in Figure 5.10 and is meant to yield a reliable impression of the residual Z-movement. Using the atom-tracking technique (for details see Chapter 4), a complete drift-free three-dimensional data set was acquired. From these 3D data, the interaction force is calculated, using the formula discussed in Section 4.6.3.

5.6.2. Contrast classification scheme

Strong evidence for a (2×1) reconstruction on the $CaCO_3(10.4)$ surface has been presented in literature [185, 197, 158]. Therefore, the (2×1) supercell is herein considered as the smallest structural unit. Inside this (2×1) supercell, up to four sites of maximum attractive interaction are observed upon using the NC-AFM technique. These sites are apparent as up to four "bright spots" in the Δf channel. Whether these spots represent the position of the calcium, oxygen or carbon atoms is left open for the time being, it will be discussed later.

NC-AFM data demonstrating different contrast modes have already been presented by J. Schütte [184], but no systematic classification has been given in literature so far. The classification scheme proposed within this section eliminates this deficiency and covers all NC-AFM $CaCO_3(10.4)$ contrasts observed to this day. The scheme is divided into one subclass discussing the *vertical* constrasts (namely $\mathbf{V_1}$

[3] The full width at half maximum (FWHM) is determined by $\mathrm{FWHM} = 2\sqrt{2\ln 2}\sigma$, where σ is the standard deviation given from the Gauss distribution of the histogram.

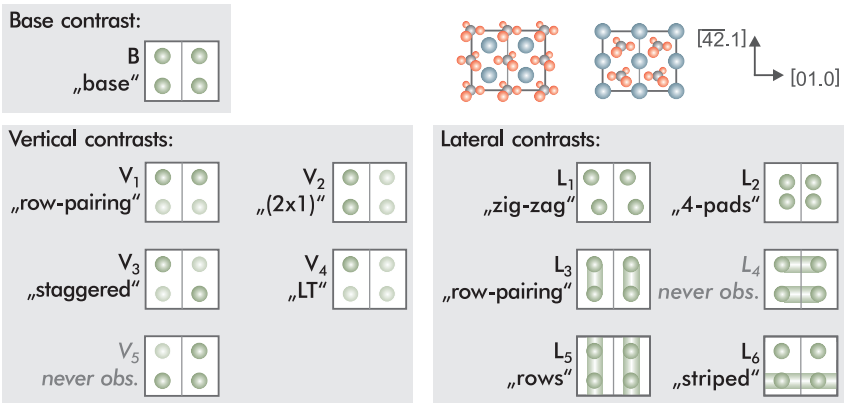

Figure 5.9.: Classification scheme describing the NC-AFM contrasts on $CaCO_3(10.4)$ surfaces observed to this day. Up to four interaction maxima are present within the (2×1) surface unit cell. The appearance of these maximum positions divide the subclasses to the "base" contrast mode **B**, vertical contrast modes $\mathbf{V_i}$ and lateral contrast modes $\mathbf{L_i}$.

to $\mathbf{V_5}$) and one subclass uniting the *lateral* contrasts (namely $\mathbf{L_1}$ to $\mathbf{L_6}$). A schematical representation of this scheme is depicted in Figure 5.9. All constrasts are classified by the appearance of the four "bright spots" in the Δf channel. The most simple appearance is given by the *base* contrast **B**, with which I commence the discussion.

Base contrast B This contrast is formed by four spots of equal brightness, size and separation. Consequently, neither the row-pariring nor the (2×1) reconstruction are visible in this contrast mode. Exemplary data are presented in Figure 5.10, which shows a frequency shift Δf image acquired in the quasi constant-height mode. The residual Z movement is in the order of 7 pm as determined from the height distribution in the inset. Thus, feedback-loop artifacts are expected to be absent. Furthermore, the single defect resolved in Figure 5.10 demonstrates a most sharp AFM tip. Consequently, averaging artifacts due to a blunt tip can be ruled out. The analysis later will suggest that this contrast might be found only in specific interaction regimes.

Vertical modes $\mathbf{V_1}$ to $\mathbf{V_5}$ The *vertical* contrast modes describe the contrast formation only due to the vertical deviations of the interaction at the four spot sites, in particular no lateral effects are considered. In the Δf channel, the interaction at these positions is apparent as "brightness". However, not the absolute value in terms of frequency shift or interaction force is considered here, but a sim-

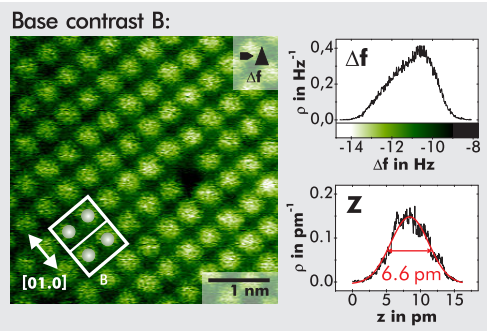

Figure 5.10.: Contrast mode **B**: Four sites of maximum interaction are revealed inside the (2×1) unit cell. They are identical in interaction strength, size and separation. A most sharp AFM tip is demonstrated in these data by resolving a point defect. The quasi constant-height mode is used and the residual Z-movement by means of the FWHM in the height distribution is as small as 6.6 pm.

ple binary contrast formation: Strong or weak interaction. In the Δf data, this is found as "bright" and "darker" spot sites. For this abstract relationship, combinatorial analysis reveals a total of six possible combinations[4]. One of these cases is the already discussed base constrast **B**, where all spots exhibit a similar interaction. The other cases are the vertical modes $\mathbf{V_1}$ to $\mathbf{V_5}$, where either one, two or three spots appear "bright", the other three, two or one "darker", respectively.

In modes $\mathbf{V_1}$ to $\mathbf{V_3}$, two spots appear "bright" due to a similar interaction strength, the other two are imaged "darker", i.e. causing a smaller attractive interaction. Each pair of equal interacting spots is either oriented along the [01.0] direction (in mode $\mathbf{V_1}$), along the $[\overline{42}.1]$ direction (in mode $\mathbf{V_2}$) or they are staggered (in $\mathbf{V_3}$).

The first mode $\mathbf{V_1}$ is the well-known row-pairing contrast, where every second row is imaged darker. This contrast has widely been reported in literature before, using contact and non-contact AFM [198, 185, 15]. For the NC-AFM mode, Figure 5.11(a) presents a typical example for the $\mathbf{V_1}$ contrast. It will later be presented that this contrast is apparent in nearly all interaction regimes, however, sometimes hardly visible.

The second mode $\mathbf{V_2}$ is the contrast, from which predominantly the (2×1) reconstruction is revealed in the NC-AFM data. Two experimental examples are depicted in Figures 5.11(b) and (c). The latter image is a combination of the later introduced lateral contrast $\mathbf{L_3}$ with the vertical contrast $\mathbf{V_2}$. The distance-dependent formation of this contrast $\mathbf{V_2}$ has first been investigated by Schütte *et al.* [185] and will further be elucidated in Section 5.6.3. My data will present that this contrast is also found in nearly all interaction regimes, though often hardly revealed.

In the third contrast mode $\mathbf{V_3}$, the "bright" spots are staggered inside the (2×1)

[4] The symmetry properties of the substrate are neglected here. All cases bearing a mirror symmetry to each other are merged. Additionally, a translation by half the unit cell is allowed as such a translation could not be detected by the NC-AFM. The case of all spots "darker" is neglected. It cannot be distinguished from base contrast **B**.

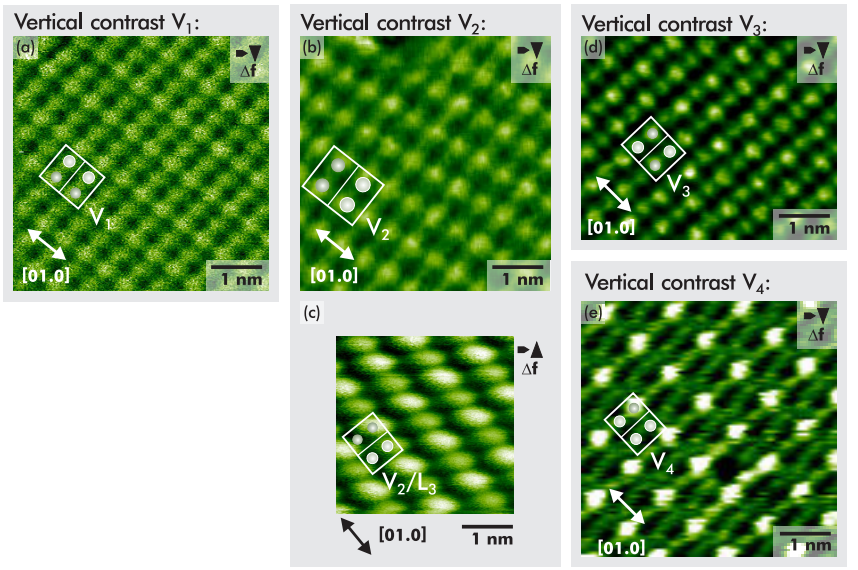

Figure 5.11.: Vertical contrast modes $\mathbf{V_1}$ to $\mathbf{V_4}$. Z movements: (a): 21 pm, (b): 23 pm, (c): true constant-height, (d): 12 pm, (e): 54 pm. A 5 pixel mean is applied to images (b) and (d). (e): adapted from J. Schütte [184].

supercell. Presumably, both characteristics row-pairing and (2×1) reconstruction superimpose themselves in this mode. The contrast is observed rarely, however, experimental evidence is included in Figure 5.11(d). To my best knowledge, it is here observed for the first time.

The fourth contrast mode $\mathbf{V_4}$ has so far only been observed at reduced temperatures by Schütte *et al.* [185]. Only one of the spots is imaged "bright", while all other are "darker". One exemplary image acquired at a sample temperature of about 110 K is presented in Figure 5.11(e).

The fifth contrast mode $\mathbf{V_5}$ has not been observed experimentally so far. It can be considered as an inversion of contrast $\mathbf{V_4}$, where three spots are imaged "bright" and only one is "darker". This mode is included in this discussion for consistency reasons only.

Lateral contrasts $\mathbf{L_1}$ to $\mathbf{L_5}$ For *lateral* effects such as shifts or merging of spots, six more *lateral* contrast modes are herein proposed: modes $\mathbf{L_1}$ to $\mathbf{L_6}$. In contrast to the vertical modes, the lateral modes do not follow a combinatoric analysis and, thus, they cover all contrasts observed up to now. This list might still be incomplete.

Among these modes is the well-known "zig-zag" in *lateral* mode $\mathbf{L_1}$. In this mode, every second spot along [$\overline{42}$.1] is slightly shifted along the [01.0] direction. This contrast has been observed before in the studies by Barth [15] and Schütte [184, 185] using the NC-AFM, by Rode *et al.* [169] using NC-AFM in liquid environment and by Liang *et al.* [117] using contact AFM. The zig-zag has been related to the orientation of the topmost oxygen atoms in the CO_3 groups. The analysis in Section 5.6.3 will present that this contrast is most pronounced at intermediate tip-sample distances. One typical NC-AFM example is included in Figure 5.12(a).

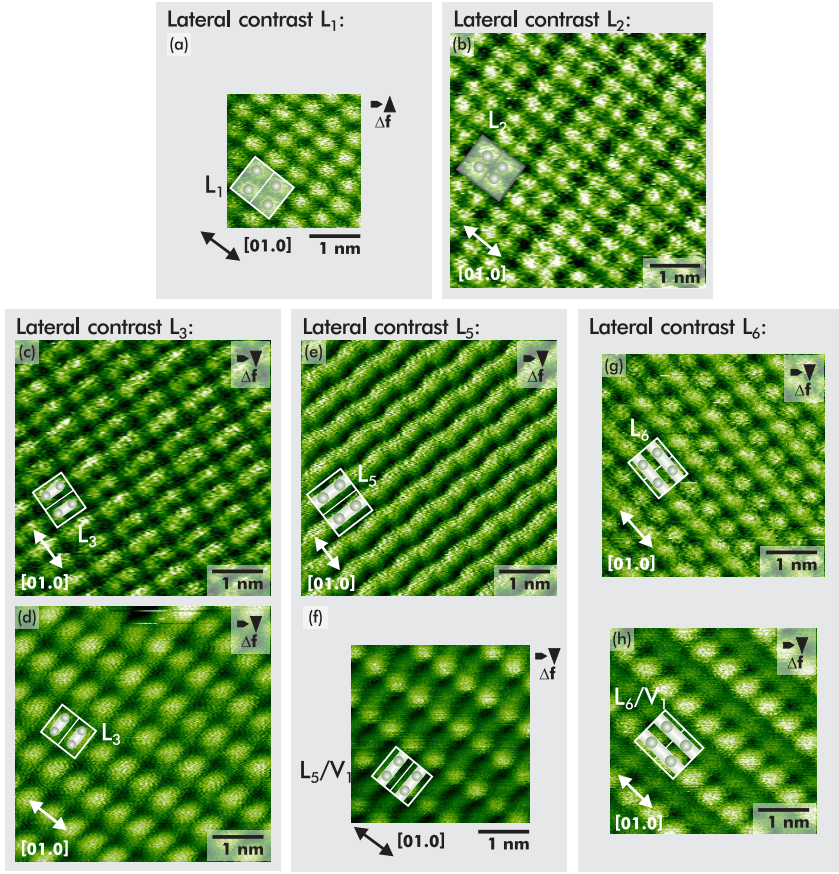

Figure 5.12.: Lateral contrast modes $\mathbf{L_1}$ to $\mathbf{L_6}$. Z movements: (a): 19 pm, (b): 13 pm, (c): 21 pm, (d): 21 pm, (e): 47 pm, (f): true constant-height, (g): 12 pm, (h): 17 pm. (b): adapted from J. Schütte [184].

The "4-pad" contrast mode $\mathbf{L_2}$, where all four spots appear to move to the unit cell centre, has been observed before by J. Schütte [185]. Exemplary data is included in Figure 5.12(b), but the physical origin remains unclear so far.

The third and fourth contrast modes are characterised by a pairing of two spots, either along the $[\overline{42}.1]$ direction in contrast mode $\mathbf{L_3}$ or along the [01.0] direction in contrast mode $\mathbf{L_4}$. Mode $\mathbf{L_3}$ corresponds to the row-pairing and has, therefore, been observed in numerous experiments as mentioned before. Figures 5.12(c) and (d) depict representative NC-AFM data for contrast mode $\mathbf{L_3}$. The formation in (d) is an extreme manifestation of this contrast mode, which will be related to a tip reconfiguration in Section 5.6.4. The mode $\mathbf{L_4}$ has so far not been observed experimentally, it is included in this discussion for consistency reasons only.

The two remaining contrast modes $\mathbf{L_5}$ and $\mathbf{L_6}$ are characterised by continuous lines, either along the $[\overline{42}.1]$ direction in mode $\mathbf{L_5}$ or along the [01.0] direction in mode $\mathbf{L_6}$. In mode $\mathbf{L_5}$, which suggests a relation to the row-pairing reconstruction, each line usually appears at a similar interaction strength. A typical NC-AFM image is depicted in Figure 5.12(e). Also, a combination of modes $\mathbf{L_5/V_1}$ is observed and one example is depicited in Figure 5.12(f). For mode $\mathbf{L_6}$, usually one straight line alternates with individually resolved atoms as the representative data in Figure 5.12(g) demonstrate. This asymmetry might reflect the asymmetry induced by the row-pairing reconstruction. Additionally, Figure 5.12(h) depictes a combination of contrasts $\mathbf{L_6/V_1}$, where also one row appears as a continuous stripe and the other in form of single atoms. However, each row bears a different interaction strength. Later results will present that this mode is predominantly found at small tip-sample distances.

5.6.3. Distance dependent contrast formation

The distance dependence in contrast formation and interaction force is discussed by means of the three-dimensional (3D) data set acquired with the atom-tracking system, supplemented by true constant-height images. Details on the technical implementation, data acquisition and analysis for the 3D data are presented in Chapter 4. From the 3D data space, only data expected to be acquired with the same tip termination is analysed here. Naturally, the analysis of this 3D data space yields results for one specific AFM tip termination and is not necessarily applicable to different tip terminations. This, however, is a fundamental issue in high-resolution NC-AFM experiments [93].

In Figure 5.13(a) and (b), $\Delta f_i(z)$ and $F_i(z)$ curves extracted from 16 inequal positions inside the (2×1) unit cell are presented. These positions cover all high-symmetry positions, namely positions of maximum interaction as well as hollow sites. The sites are named by capital latin letters K–Z and their positions inside the (2×1) super cell are depicted in Figure 5.13(d). In the data space, they are extracted at equivalent sample sites as depicted in Figure 5.13(c). To increase the

signal/noise ratio, a total of 37 curves has been averaged at each position. The averaging postions lie in a circle of radius 3 pixel, which amounts to ∼ 60 pm lateral radius. The circles are included in Figure 5.13(c). The lower curves in Figures 5.13(a) and (b) denote the averaged raw data curves, while the upper curves were calculated as $\Delta f_i(z) - \Delta f_{\mathrm{mean}}(z)$. Here, $\Delta f_{\mathrm{mean}}(z) = \frac{1}{N}\sum_{i=1}^{N} \Delta f_i(z)$ is the averaged curve of the whole data subspace containing a total of N curves. This representation is chosen to enhance the visibility of subtle differences in the contrast formation. In Figure 5.13(b), the frequency shift data are converted to the interaction force, using Equation 4.9 from Section 4.6.3. The same representation as in Subfigure (a) is chosen: The lower curves present the raw data and the upper curve the difference $F_i(z) - F_{\mathrm{mean}}(z)$.

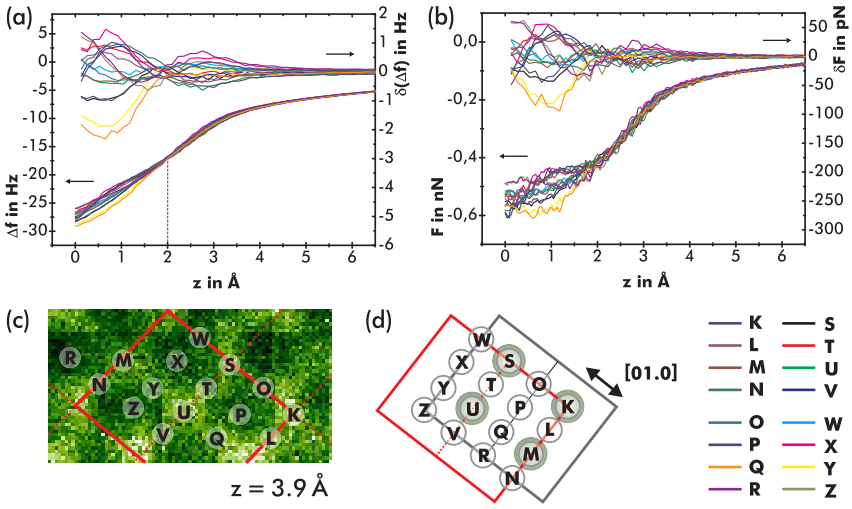

Figure 5.13.: (a) $\Delta f_i(z)$ curves from 16 inequivalent positions inside the (2×1) surface unit cell. (b) Corresponding $F_i(z)$ curves. The positions from which the curves are extracted are marked in (c) in the raw data space (extracted at $z = 3.9$ Å) and in (d) in a schematic representation of the (2×1) unit cell.

The data in Figure 5.13(a) suggest the existence of two contrast regimes, separated by a nodal point at $z \sim 2$ Å. However, an error in the first software version of the data acquisition protocol might have caused parasitic shifts of the curves relative to each other along the Z direction, in the worst case to a maximum of about 40 pm. The conclusions drawn in this section are expected to be largely unaffected by this flaw, especially as negligible shifts are assumed for most of the sample sites compared later. However, for the position of the nodal point separating the contrast regimes this flaw might have a significant influence. Therefore, the nodal point is not further discussed here.

At small tip-sample distances, the corrugation[5] is in the order of 4 Hz and, therefore, way above the instrument noise level. Atomic contrast is easily observed in this regime, where the maximum attractive force amounts to ~ 0.6 nN. In the contrary, the atomic contrast is more difficult to observe at larger tip-sample distances. Here, the corrugation is as small as 0.2 Hz at $z = 7.4$ Å. Interestingly, the data presented here show that the atomic contrast is still visible[6] with corrugations smaller than 20 mHz even at distances larger than 9 Å.

The contrast formation at different tip-sample distances is identified from X-Y planes extracted from the data space. These planes are presented in Figure 5.14(b) to (k), with their Z-position indicated in the [01.0]-Z cut in Figure 5.14(a). To enhance the contrast in this representation, each presented image is calculated as the average from five X-Y planes, corresponding to a Z-resolution of ~ 22 pm. This value is in the order of the Z-movement in quasi constant-height images and, therefore, averaging over this height range is fully justified. The (2×1) surface

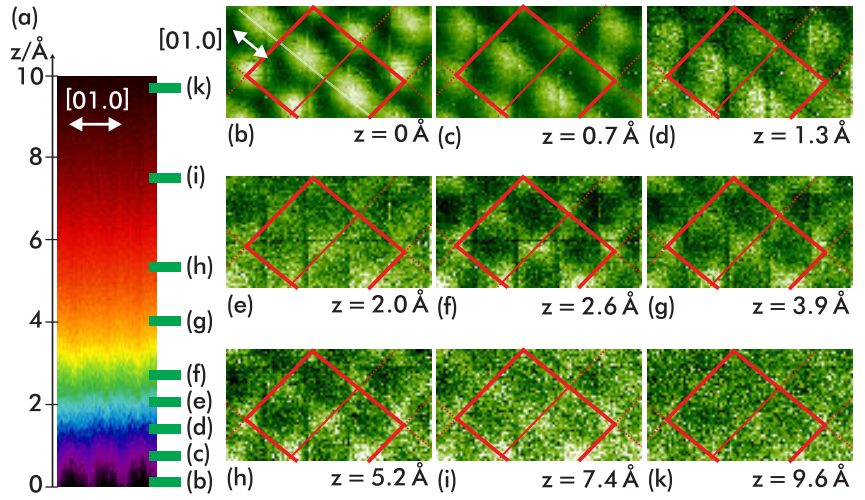

Figure 5.14.: (a) Data projection along a [01.0]-Z plane and (b) projections along X-Y planes. The Z-positions of the X-Y planes (b) to (j) are indicated by green rectangles. To enhance the contrast in the X-Y data planes, the average value from 5 pixel along Z-direction is visualised. The height of the green rectangles indicates the resulting Z-resolution of 22 pm.

unit cell is included in each image at the same absolute lateral position, aligned with their corner sites on top of the bright spots visible at large tip-sample dis-

[5] "Corrugation" is defined as the difference between the interaction maxima and minima. Typically, this is the difference between an atom centre and a hollow site.

[6] The values are identified from the data space by reducing the noise using intense averaging.

tances. At large tip-sample distances, these spots remain stationary irrespective of the Z-position of the plane. This observation is generally not valid for small tip-sample distances, where some points of maximum interaction shift by up to a quarter of the unit cell size. To be more specific, here the positions of maximum interaction at the (2×1) unit cell vertices remain fixed, while those *inside* the depicted unit cell shift along the [01.0] substrate direction by about $b/4$. Owing to the atom-tracking technique, I can rule out that this observed shift is a drift or a feedback-loop artifact. The resulting contrast at this tip-sample distance is of type $\mathbf{L_1}$, the well-known zig-zag. At intermediate distances ($z\sim1.3$ Å), the data in Figure 5.14(d) suggest a mixture of contrasts $\mathbf{L_1}$ and $\mathbf{L_3}$. The physical explanation for this behaviour might be given from relaxation processes in the sample due to the row-pairing or relaxation processes due to the presence of the tip [63]. With the current theoretical understanding, both reasons are plausible. On the contrary, the contrast at large tip-sample distances appears to be the base contrast **B** judging from the X-Y planes in Figures 5.14(f) to (k). Possibly, the zig-zag in contrast mode $\mathbf{L_1}$ with a very small amplitude is visible as well. In conclusion, a distance dependence for the zig-zag amplitude is revealed: At large tip-sample distances the zig-zag amplitude is virtually zero and, thus, no zig-zag is observed. Upon decreasing Z, the amplitude increases to a value as large as $b/4$.

In a next step, the visibility of the row-pairing and the (2×1) reconstruction is discussed. For this purpose, Figures 5.15(a) and (b) present $\Delta f_i(z)-\Delta f_{\mathrm{mean}}(z)$ curves extracted from 16 inequivalent high-symmetry positions inside the surface unit cell. These are the same data as already presented in Figure 5.13. In each plot, the 16 curves are grouped to quartets of four curves[7]. Each group compasses curves from positions lined up either along the [01.0] direction (in Figure 5.15(a)), or along the $[\overline{42}.1]$ direction (in Figure 5.15(b)).

The curves in Figure 5.15(a) discuss the visibility of the (2×1) reconstruction in contrast mode $\mathbf{V_2}$. In this contrast mode, the reconstruction is apparent as an interaction difference between two maxima sites (and also between two minima sites) inside the (2×1) unit cell. These sites are lined up along the [01.0] direction. In Figure 5.15(a), therefore, the area between every second curve extracted along [01.0] is shaded to directly depict the (2×1) visibility. Interestingly, the (2×1) reconstruction in form of contrast $\mathbf{V_2}$ is visible on nearly all unit cell positions at nearly all distances. For small tip-sample distances, the corrugation is comparable for nearly all unit cell positions and in the order of 0.4 Hz. The contrast is most pronounced on the P-X sites with a difference of 1 Hz. Interestingly, these sites are the hollow sites. This finding is in agreement with the work from J. Schütte [184], where the hollow sites have also been suggested to be the maximum corrugation

[7] As before, a total of 37 curves on a circle with a radius of 3 pixel (60 pm) has been averaged for each position.

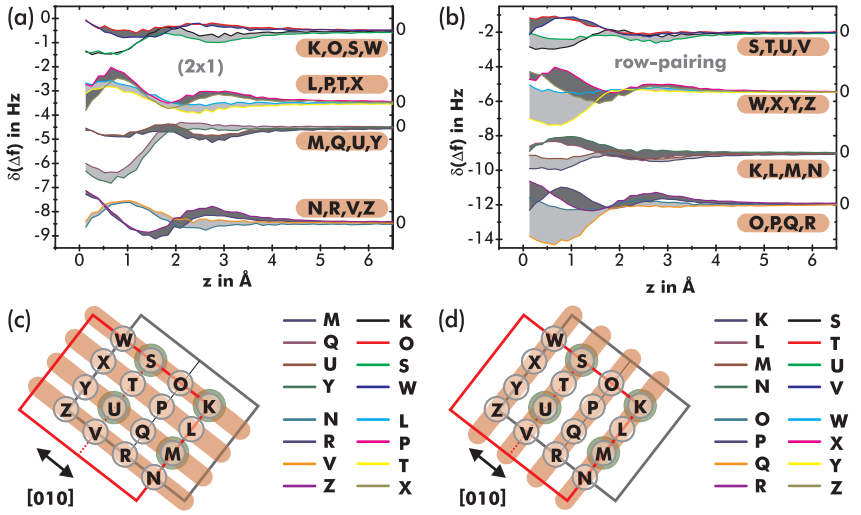

Figure 5.15.: (a) $\Delta f_i(z) - \Delta f_{\text{mean}}(z)$ curves taken from the surface unit cell. Each quartet contains four curves from positions lined up along [01.0]. The shaded regions identify the visibility of the (2×1) reconstruction in contrast mode $\mathbf{V_2}$. (b) The same data, but each quartet here contains curves from positions lined up along $[\overline{4}2.1]$. The shaded regions denote the visibility of the row-pairing in contrast mode $\mathbf{V_1}$. In both Figures, the axis at the left Figure side has an arbitrary offset to each curve group, but provides a correct scaling. (c) and (d) denote the curve positions inside the (2×1) unit cell and the colour code for all curves is depicted.

sites. On the contrary, mode $\mathbf{V_2}$ is hardly visible on sites O-W. For large tip-sample distances, the largest corrugation measured is about 0.35 Hz for $z = 2.7$ Å at sites R-Z. This value is comparable to the noise level of the used microscope [24] and, thus, it is not expected to frequently resolve the (2×1) reconstruction directly from NC-AFM images in this regime. This statement especially holds for large Z, where the corrugation is in the order of mHz. Additionally, a large number of nodal points is present in all groups. Thus, there are interaction regimes where the (2×1) reconstruction is invisible. Additionally, these nodal points likely cause contrast inversions [161] in imaging the surface. This fact renders the interpretation of quasi constant-height or even constant frequency-shift images a delicate task.

In Figure 5.15(b), the visibility of the row-pairing in form of contrast mode $\mathbf{V_1}$ is discussed. A similar strategy is followed as before when discussing the (2×1) reconstruction. Again, four groups of $\Delta f(z)$ curve quartets are used. However, each quartet is here given from curve positions lined up along the $[\overline{4}2.1]$ direction. In Figure 5.15(b), the shaded area between each curve pair, extracted from

every second position along [$\overline{42}$.1], now denote the visibility of the row-pairing in contrast mode $\mathbf{V_1}$. However, the curve shading at small tip-sample distances (at approx. $z < 2$Å) mixes the row-pairing contrast with the zig-zag contrast $\mathbf{L_1}$ due to the shift of the lateral maxima and, thus, is not considered here. At $z > 2$Å, the row-pairing is present through a slightly increased corrugation compared to the (2×1), and it is likewise apparent also at large tip-sample distances. As before for the (2×1), the row-pairing is apparent on nearly all sites. Here, the positions L-N and P-R yield the largest corrugation of 0.6 Hz.

In the 3D data acquisition, it was refrained from sampling data near the $\Delta f(z)$ minimum or even in the repulsive regime in order to maintain an (ideally atomically) sharp and stable AFM tip. This regime, however, is covered in another experiment, where imaging in the true constant-height mode is performed. The results of such a true constant-height mode imaging are presented in Figure 5.16: For both frequency shift images (a) and (b), the tip is first approached to the sample surface within the first lines (not shown), followed by a linear ramp directed outwards. The slow scan-direction in the images is oriented from bottom to top in (a) and vice-versa in (b). To identify the absolute Z-position, the mean value of each row is scaled such that they coincide with a $\Delta f(z)$ curve taken at one sample position[8]. As apparent from Figure 5.16(c), the frequency-shift images span a Z-range of about 4Å.

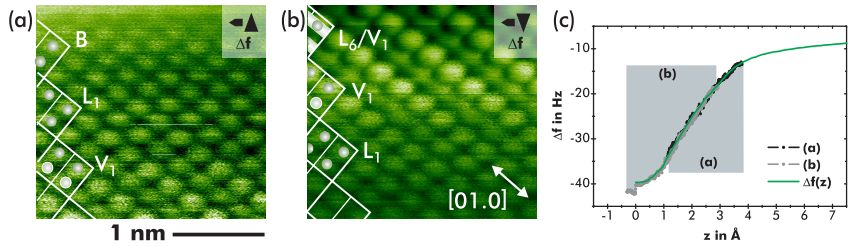

Figure 5.16.: Contrast formation near the lower turning point using the true constant-height mode. (a) And (b) are two images, where the tip is first approached close to the surface, followed by a successive ramp outwards in up (a) and in down (b) slow-scan direction. (c) The row mean values are aligned to a $\Delta f(z)$ curve acquired in the image before. To increase the visibility, a plane-correction algorithm is applied to images (a) and (b).

The contrast evolution in this experiment is straightforward to characterise: At large tip-sample distances ($z \sim 3$Å), the base contrast **B** is observed. Reflecting the analysis before, contrasts $\mathbf{V_2}$ or $\mathbf{V_1}$ might also be present, but presumably be-

[8]For the alignment, the mean curves are only shifted along Z and the Z-axis is allowed to rescale linearly. This rescaling accounts for sample tilt, residual Z-drift and the tip retraction speed.

low the instrument noise level and, thus, not revealed here. When further approaching the tip towards the surface, first the zig-zag contrast $\mathbf{L_1}$ evolves, and, at even smaller Z, contrast $\mathbf{V_1}$ becomes apparent. Last, nearby the minimum of the $\Delta f(z)$ curve approached in the top lines of Figure 5.16(b), the former lateral zig-zag contrast evolves into the striped appearance $\mathbf{L_6}$, combined with row-pairing contrast $\mathbf{V_1}$. This contrast evolution is in agreement with the distance-dependent data from the 3D data set presented before, however, here the formation is extended to the lower turning point of the $\Delta f(z)$-curve.

Most interestingly, these data present the strategy to identify the surface enantiomer, if the surface is assumed to be chiral: At intermediate tip-sample distances, the zig-zag orientation is apparent and the row-pairing evolve upon decreasing Z. Correlating the zig-zag orientation with the row-pairing, these data represent the "S" enantiomer.

5.6.4. Tip-termination dependent contrast formation

For the row-pairing contrast in the extreme variant as depicted before in Figure 5.12(d), experimental findings suggest a severe tip termination influence. This is demonstrated by the data in Figure 5.17, which are successive images acquired in a quasi constant-height mode. In Figure 5.17(a), the $CaCO_3$(10.4) surface is imaged in a combined $\mathbf{V_1}/\mathbf{L_1}$ mode. Both, the height differences of the row-pairing and the zig-zag pattern are visible. In Figure 5.17(b), the surface is imaged in the extreme manifestation of contrast mode $\mathbf{L_3}$. It is neither possible to identify the zig-zag pattern nor the row-pairing contrast $\mathbf{V_1}$, because each pair of spots couple to a single spot. This coupling results in only two maximum interaction sites inside the (2×1) unit cell, instead of four. In the experiment, tip-changes due to tip-sample contacts are provoked before and after this image, leading to a different contrast mode before and after the tip-changes. Figure 5.17(c) presents the contrast $\mathbf{L_1}$, which is observed after the second provoked tip-reconfiguration. This contrast is comparable to the contrast in Figure 5.17(a), observed before the first tip change and, therefore, before the contrast observed in Figure 5.17(b). Thus, in this experiment is was possible to switch from contrast $\mathbf{L_1}$ to $\mathbf{L_3}$ and vice-versa.

To elucidate the contrast formation, $\Delta f(z)$ curves were acquired using the atom-tracking $\Delta f(z)$ curve acquisition protocol[9] described in Section 4.5.5. One $\Delta f(z)$ curve from each mode in (b) and (c) is presented and the corresponding sample sites are indicated by crosses in Figures 5.17(b) and (c). The frequency-shift data is converted to the force and is additionally depicted in Figure 5.17(e). The acquired curves present fundamental differences, most prominent, the magnitude of the minimum value differs by about a factor of two. Furthermore, the curvature in the medium distance regime (at $z \sim 4$ Å) is different between these

[9] For $\Delta f_1(z)$ a total of 20 curves and for $\Delta f_2(z)$ a total of 50 curves are averaged.

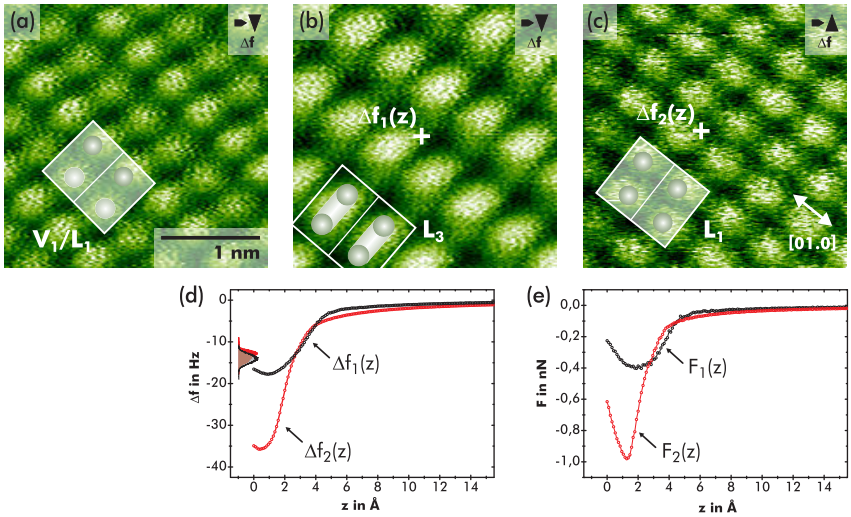

Figure 5.17.: Tip-termination dependent contrast formation: provoked tip-reconfigurations between the images switch the contrast from $\mathbf{V_1/L_1}$ in (a) to $\mathbf{L_3}$ in (b) and back to $\mathbf{L_1}$ in (c). The data are acquired at roughly the same interaction stregth: $\overline{\Delta f} \sim 19.5\,\mathrm{Hz}$ for (a), $\overline{\Delta f} \sim 17\,\mathrm{Hz}$ in (b) and $\overline{\Delta f} \sim 18.5\,\mathrm{Hz}$ in (c). $\Delta f(z)$ curves are acquired at the indicated positions in (b) and (c) and are reproduced in (d) and converted to the force in (e).

two curves and the force minimum is steeper[10]. These severe differences in the force-distance curves suggest that the tip was exposed to an intense reconfiguration, possibly by both, geometric and electronic means. A detailed understanding of this tip-reconfiguration, however, requires a discussion in terms of *ab-initio* calculations, which is beyond the scope of this thesis.

Understanding the tip configuration, most importantly for the contrast $\mathbf{L_3}$, is of utmost interest in terms of determining the chirality of the surface. The discussion in Section 5.4 left the question unanswered, whether the row-pairing is a tip artifact or a true surface property. The next necessary step is to elucidate the contrast formation for different tip-terminations by means of *ab-initio* studies. The herein presented data clearly present the switching of a tip-termination between two contrast modes and are, thus, a most promising input for a theoretical treatment.

[10]The curves are aligned along Z by arbitrarily setting the smallest z value to 0 Å. Therefore, the minimum position along Z has to be accounted as undefined.

5.6.5. Imaging in the repulsive regime

The NC-AFM contrast formation in the repulsive regime is investigated by means of true constant-height images, the results from one such experiment are presented in Figure 5.18. The measurement is started in the attractive regime near the lower turning point of the $\Delta f(z)$ interaction curve in Figure 5.18(a). A combination of contrasts $\mathbf{V_2}/\mathbf{L_3}$ is observed. In the subsequent images, the tip-sample distance is successively decreased to Figure 5.18(f). The mean frequency-shift value of each image is given in Figure 5.18(g), plotted against the Z-position of each image. Only six of a total of 20 images are presented here, the positions of the others are included by small circles in the $\Delta f(z)$ diagram. The repulsive regime is certainly reached in Figures 5.18(e) and (f), where the frequency shift is positive[11].

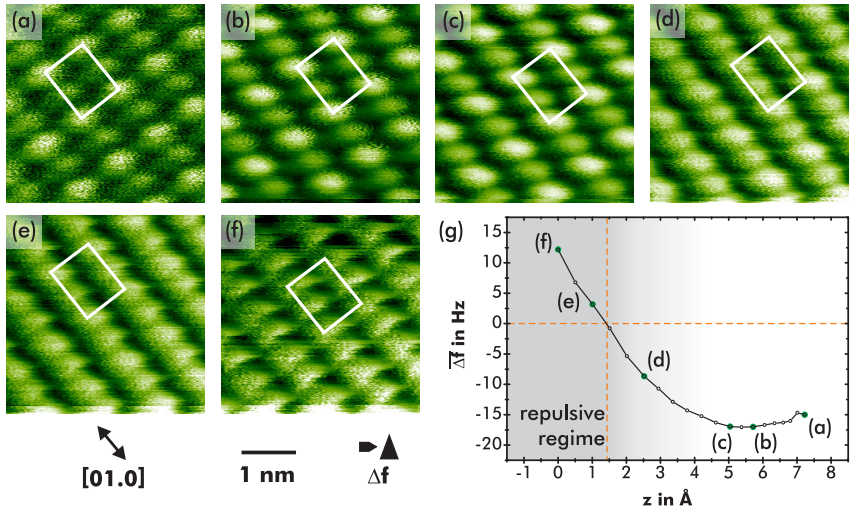

Figure 5.18.: Contrast formation in the repulsive regime. The tip-surface distance is decreased successively from image to image. The mean value from each image is plotted against the image Z-position in (g). The Z-axis has been corrected for residual thermal drift from a reference image acquired at the end.

The observed contrast is identified as a mixed $\mathbf{L_3}/\mathbf{V_2}$ mode at large tip-sample distances (Subfigures (a) to (c)), while it is exclusively $\mathbf{V_3}$ in the repulsive regime (Subfigures (e) and (f)). Furthermore, the imaged species exhibit a triangular shape in the repulsive regime, all triangles pointing to the right with one cor-

[11] For the large amplitudes used here, the exact transition between the attractive and repulsive regime cannot be stated unambiguously from these data. However, a positive frequency shift clearly indicates that the tip enters the repulsive regime. [161]

ner site. Interestingly, this orientation is also present in the backward scan and might be related to the carbonate group orientation. This suggestion is further investigated in Section 5.6.6. Additionally, imaging in the repulsive regime is accompanied by intense dissipation processes, which is evident from the respective channel. Relaxation processes in both, tip and sample are very likely to occur.

5.6.6. Identifying the carbonate group orientation

As discussed in the previous Section, imaging the bright species on $CaCO_3$(10.4) around the $\Delta f(z)$ minimum yields an asymmetry in its appearance, which might point to the carbonate group orientation. To further elucidate this issue, Figures 5.19(a) to (f) present NC-AFM images acquired in the true constant-height mode. During the first lines in each image, the tip-sample distance is decreased with Subfigure (a) acquired at the largest and Subfigure (f) at the smallest Z position. The detuning histogram of each image is included in the $\Delta f(z)$-curve in Figure 5.19(g) to illustrate the absolute Z position. Whether images (d) to (f) are already taken in the repulsive regime cannot definetely argued with no $\Delta f(z)$-curve available in this regime [161]. The total Z-range covered with the images is estimated[12] to be at least 5 Å.

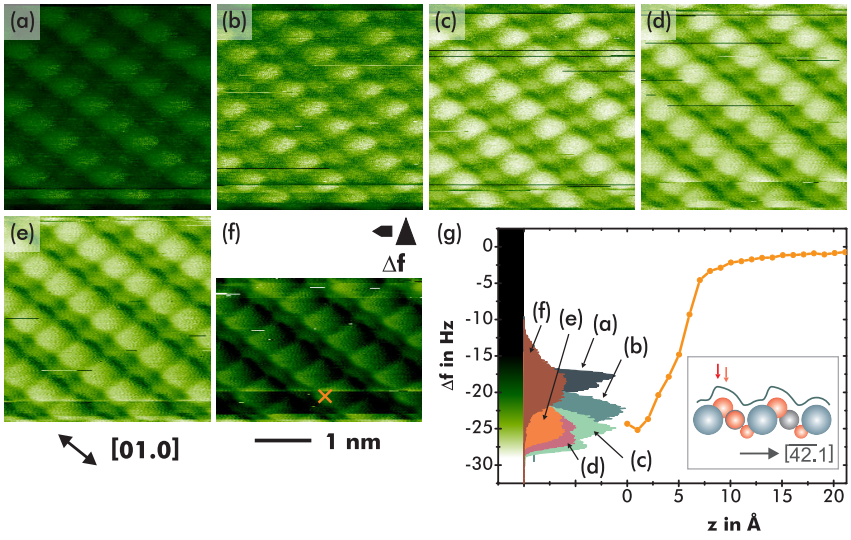

Figure 5.19.: NC-AFM contrast in the vicinity of the $\Delta f(z)$-curve minimum. All images are true constant-height images with a deactivated Z feedback loop. The appearance is the same for the backward scan (not shown).

[12] Assuming that the $\Delta f(z)$ curve is symmetric around the minimum.

In all images, the row-pairing expressed as contrast $\mathbf{V_1}$ is apparent. This is in agreement with the distance-dependent study presented before in Section 5.6.3, where this contrast mode was found at small tip-sample distances. At the same time, the zig-zag is slightly visible in contrast mode $\mathbf{L_1}$.

A careful investigation of the shape of the bright spots reveals an asymmetry in the imaging contrast: In Subfigures (a) and (b), which are definitely taken in the attractive regime and where the $\Delta f(z)$ slope is still positive, the upper right sides appear brightest. When reducing the tip-sample distance, first all spots exhibit a symmetrical appearance in (c), while at closer distances the lower left sides appear brightest in (d) to (f).

This behaviour might be explained by simple geometric arguments: the topmost oxygen atom of each carbonate group protrudes the calcite sample surface by 78 pm. Compared to the other surface atoms, its distance to the force sensing tip is smallest. For a suitable tip termination, it is thus expected that the local maximum force is sensed here. When decreasing the tip-sample distance, this sample site is expected to be the first site where repulsive interactions contribute significantly and, thus, smaller Δf values are measured. Figure 5.20 presents Δf interaction values extracted from the images in Figures 5.19(a) to (f) at the positions A to C as indicated in the inset. At large tip-sample distances (Figures 5.19(a) and (b)), position A at the right spot side is imaged "brightest". This interaction site (green curve) has a minimum at Z distances larger than the red curve, which is extracted at position C. These findings are in complete agreement with the contrast interpretation before: the topmost oxygen atom is imaged bright first (green curve), followed by the centre site of a $CaCO_3$ group (black curve) and, last, by the topmost oxygen atom averted side (red curve) when reducing the Z distance. This model precisely explains the observed contrast formation.

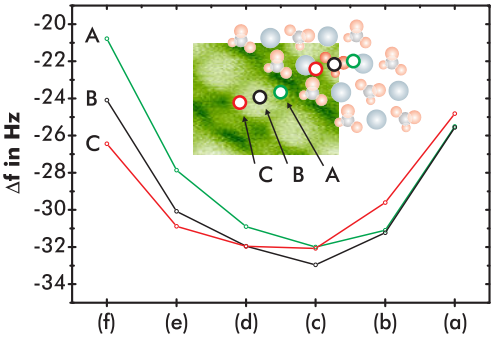

Figure 5.20.: Δf values extracted from three sample positions as indicated in the inset. Letters (a) to (f) on the abscissa denote the subfigures in Figure 5.19. Image (a) is aquired at the largest Z, while (f) corresponds to the smallest tip-sample distance.

Additionally to the contrast formation in the Δf channel, it should briefly be mentioned that also dissipative interactions are observed. This is depicted in Figure 5.21, where Figures 5.19(b) and (e) are reproduced and supplemented by the

respective dissipation data. This dissipative interaction might point to relaxation processes in both, tip and sample material as modelled before by Foster *et al.* [63].

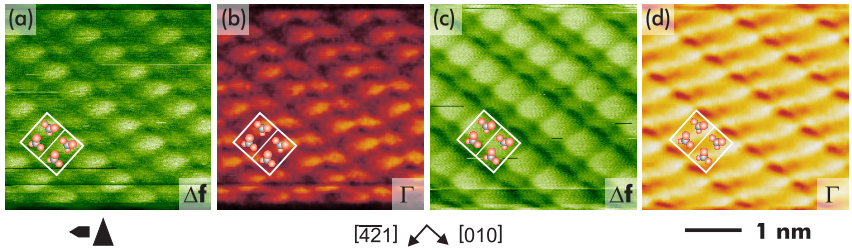

Figure 5.21.: Dissipation contrast in the vicinity of the $\Delta f(z)$ minimum. (a) and (c) reproduce the same constant-height Δf data already presented in Figures 5.19(b) and (e), respectively. Γ is the dissipation signal.

It should briefly be noted that of course a similar effect would be present for a peculiar tip termination, where the described imaging process occures at different tip sites. However, the asymmetric appearance of the "bright" species has been observed for at least three different tips, rendering an imaging artifact unlikely. These experimental data, thus, suggest two important conclusions: First, for this contrast mode the data identify the "bright" species in the Δf channel as the carbonate group. Second, these data suggest the identification of the CO_3 group orientation by means of high-resolution NC-AFM data and, thus, the identification of the absolute sample orientation is possible.

5.7. Conclusions

This chapter discussed in detail the properties of the calcite $CaCO_3$(10.4) surface. For all NC-AFM contrast patterns observed to this day, a comprehensive classification scheme was presented. The scheme defines a total of 12 contrast modes, eight of these modes were observed within this thesis, some of them for the first time. Together with literature findings, a total of 10 modes has been observed experimentally to this day. The complex contrast formation was discussed by means of 3D data, true constant-height images and $\Delta f(z)$ curves. The corrugation for both, the row-pairing and the (2×1) reconstruction is highly distance-dependent and, additionally, at a few particular tip-sample distances the reconstructions cannot be revealed with the NC-AFM. Interestingly, both reconstructions remain visible even at large tip-sample distances.

From symmetry considerations it was deduced that the (10.4) surface might reconstruct in the row-pairing pattern, resulting in a *chiral* surface. This is an unexpected finding, as the truncated bulk structure for the (10.4) surface is achiral. The

NC-AFM contrast formation for the row-pairing was classified and different appearances of the row-pairing reconstruction were revealed. Interestingly, most of them were found to appear at nearly all tip-sample distances. Only for one mode, a specific tip termination is suggested. The identification of one enantiomer was presented from high-resolution true constant-height data.

The NC-AFM contrast formation nearby the $\Delta f(z)$ curve minium reveals an asymmetric appearance of the bright species. This appearance suggests the identification of the carbonate group orientation, and with this the identification of the absolute crystal orientation. The identification of this orientation is so far only possible from the macroscopic birefringence property, as was outlined in this Section.

6. Molecular self-assembly on the calcite (10.4) surface

In this chapter, the adsorption characteristics and the self-assembly of systematically chosen organic molecules are investigated on calcite $CaCO_3$(10.4) surfaces. The discussion in Chapter 2 already suggested that choosing this particular surface might be a favourable step for studying molecular self-assembly. This was reasoned from an analysis of the involved surface energies, where $CaCO_3$(10.4) presents a tendency to predominantly favour layer-by-layer growth. This assumption, which is of course not generally valid for all molecular systems, will be confirmed for nearly all systems investigated here.

Studying the interaction of molecules with the $CaCO_3$(10.4) surface is, furthermore, of utmost interest in topics such as biomineralisation, geochemistry, pharmacy, water desalination or oil production as already outlined in Chapter 5.

This chapter is subdivided into five sections: I start discussing the characteristics of weakly interacting systems, namely of a planar hydrocarbon molecule (hexa-*peri*-hexabenzocoronene, HBC) and a fullerene (C_{60}) in Sections 6.1 and 6.2, respectively. In Sections 6.3 and 6.4, I investigate molecules containing carboxylic acid groups, namely terephthalic acid (TPA) and trimesic acid (TMA). The carboxylic acid groups greatly influence the adsorption behaviour in a positive sense. Using these findings, I combine weak van-der-Waals interactions with directed hydrogen bonds in the final Section 6.5, which results in uni-directional molecular structures of a well-defined width.

6.1. Hexa-peri-hexabenzocoronene

Planar polycyclic aromatic hydrocarbon (PAH) molecules form a well-suited starting system to gain first insights in terms of the interaction with the $CaCO_3$(10.4) substrate. The molecule hexa-*peri*-hexabenzocoronene (HBC, $C_{42}H_{18}$) is chosen as one representant for this molecular class, which is expected to only bind via van-der-Waals forces. The molecules have been synthesised in the group of [Name removed][1] and were kindly provided for my experiments. A model of a HBC molecule drawn to scale to a $CaCO_3$(10.4) surface is presented in Figure 6.1.

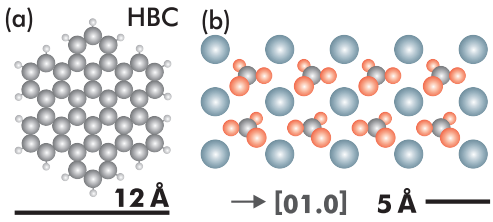

Figure 6.1.: (a) Structural model of the HBC molecule, drawn to scale to the $CaCO_3$(10.4) surface (b). Black spheres: carbon, white spheres: hydrogen, red spheres: oxygen and blue spheres: calcium.

6.1.1. Introduction

The bulk phase of HBC has been investigated in early experiments by Robertsen and Trotter [168]. The lattice parameters have been refined in a second study by Goddart *et al.* [76] in 1995. According to these studies, HBC forms monoclinic crystals of space group $P2_1/a$ with $a = (18.431 \pm 0.003)$Å, $b = (5.119 \pm 0.001)$Å, $c = (12.929 \pm 0.002)$Å and $\beta = (112.57 \pm 0.01)°$ [76] with a two-molecule basis. In the crystal structure, HBC molecules are packed in adjacent columns. The interplanar distance between two HBC molecules has been measured to 3.42 Å, while the molecules are staggered with a centre-to-centre offset of 3.8 Å [76]. This results in a nearly perpendicular orientation between two HBC molecules of adjacent columns.

HBC molecules have attracted notably interest during the last years, especially because of their possible application as conducting layers in molecular electronic devices. Notably, van de Craats *et al.* [44] reported upon a one-dimensional carrier mobility of $0.5\,cm^2V^{-1}s^{-1}$ for a columnar stack of an HBC derivate, a record for such systems in 1999.

Consequently, thin films of HBC molecules have been studied on substrates such as HOPG(0001) [228, 101, 182], MoS_2(0001) [228, 101], Au(111) [155, 188, 172, 218], Au(100) [209], Cu(111) [172] and Ag(111) [75]. On most of these conducting surfaces, the HBC molecules have been reported to form a commensurate superstructure of flat-lying HBC molecules at coverages larger than 0.7 ML. At lower

[1] Synthetic Chemistry Group at the MPI-P, Mainz, Germany

coverages, however, the HBC molecules are observed to repel each other. Thus, exclusively diffusion and no structure formation has been observed for coverages < 0.7 ML. The deposition of films with several ML thickness has been reported to mostly follow the structure of the first layer, thus forming columnar stacks of HBC molecules, which are oriented perpendicular to the sample surface. This phase, however, appears to be metastable at least for the HBC/HOPG system, as annealing to higher temperatures has been reported to induce the formation of the bulk structure [101].

In the context of molecular electronics, however, it is technologically of utmost interest to create columnar stacks oriented parallel to the sample surface, because these stacks might allow for a one-dimensional conductance and, thus, would form a *molecular wire*.

6.1.2. Morphology on calcite

HBC molecules are deposited under ultra-high vacuum conditions from a heated crucible (experimental details are given in Section 3.2.4). When the $CaCO_3$(10.4) substrate is held at room temperature during the deposition process, the molecules mainly undergo a dewetting process and pile up to three-dimensional clusters. This is illustrated by the NC-AFM data in Figure 6.2(a), where an equivalent of ~ 0.2 ML HBC is deposited. In this image, the height of the piled-up structures is observed up to 35 nm as depicted in the line profile in Figure 6.2(b). Presumably, the molecules align themselves in the monoclinic bulk crystal structure. However, in addition to the bulk phase, a small density of flat molecular islands is observed. In Figure 6.2(a), two islands are located in direct vicinity to the bulk structure as marked by white arrows. The precise island structure will be analysed later.

The ratio of islands to clusters is quantified by measuring the volume and projected area of each phase[2]. For the data in Figure 6.2(a), a total volume of about 155 000 nm^3 is measured, with a ratio of island to bulk volume of about 1 : 18. The total covered area is measured to about 22 000 nm^2, with a ratio of island to bulk covered area of about 1 : 1.6.

Thus, for the HBC/$CaCO_3$ system bulk growth is clearly favoured. This is in agreement with the mentioned study on HOPG [101], where the bulk phase appears to constitute the most stable phase, as it has been formed after annealing the molecule/sample system.

[2] The volume and projected area is determined using the "grain analysis tool" of the software Gwyddion [142] on carefully adjusted areas.

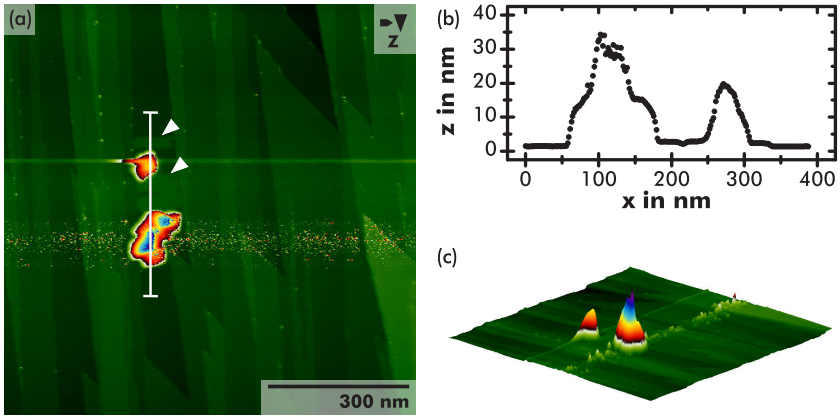

Figure 6.2.: NC-AFM data for the HBC/$CaCO_3$(10.4) system: 0.2 ML are deposited and imaged at 300 K. The height of the molecular clusters amounts up to 35 nm, as visible in the line profile in (b) and as visualised in a 3D representation in (c). The island phase (two islands marked by white arrows) has a height in the order of 1 nm and is, thus, merely visible in this image.

6.1.3. Low-temperature experiments

For $CaCO_3$(10.4), the structure formation of both, the island and the bulk phase, is inhibited when depositing the HBC molecules on a sample held at reduced temperatures. Additionally, an estimate for the diffusion barrier for single molecules is found from experiments at variable temperatures.

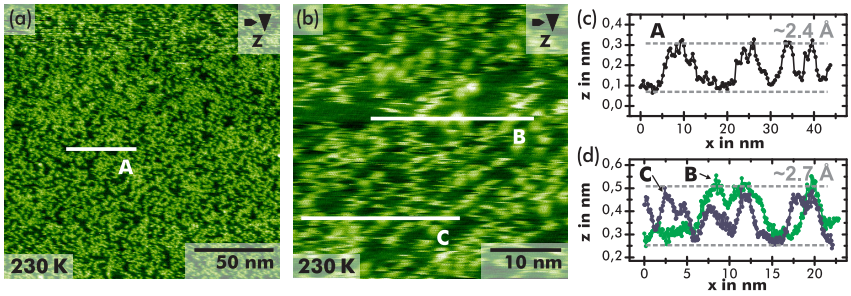

Figure 6.3.: Molecular structure of the HBC/$CaCO_3$(10.4) system at a sample temperature of 230 K. The height measured for single features suggest flat-lying HBC molecules. The onset of diffusion is most clearly revealed in (b).

Figure 6.3 presents NC-AFM data acquired with the substrate held at a temperature of $\sim$ 230 K. A small amount of HBC molecules is deposited on a clean

$CaCO_3$(10.4) surface held at 90 K, before the sample is stepwise annealed to ∼ 230 K for the NC-AFM experiment in Figure 6.3. In these data, single features are visible and are assigned to single HBC molecules. A measured height in the order of 3 Å suggests a flat-lying adsorption geometry, as apparent from the line profiles in Figures 6.3(c) and (d). Below 230 K, this species appears to be immobile, while the onset of hopping is apparent in Figure 6.3(b). Consequently, this finding suggests a diffusion barrier of about $E_d \approx (0.5 \pm 0.1)$ eV, using the estimation presented in the Appendix Section E.

From experiments at variable temperatures it is further supported that the kinetics in island and clusters growth are severely influenced by the substrate temperature during the deposition process. With the objective to increase the island density by simultaneously reducing the bulk phase volume, HBC molecules are first deposited on a clean $CaCO_3$(10.4) substrate held at a reduced temperature of 90 K. After deposition, the substrate is slowly annealed to room temperature.

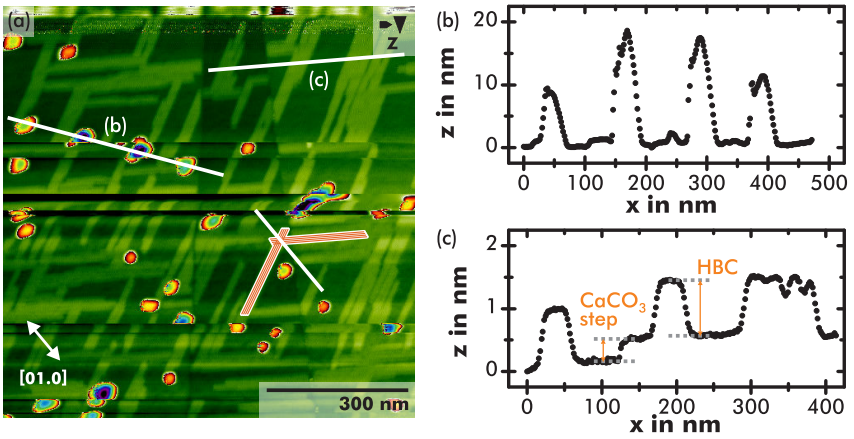

Figure 6.4.: Morphology for the HBC/$CaCO_3$(10.4) system after the variable-temperature preparation: HBC molecules are deposited with the sample held at 90 K, the sample is successively annealed to 300 K afterwards. The imaging is performed at 300 K. For determining the volume and area ratios, only subparts of this image are used, where stable molecular imaging is achieved.

Figure 6.4(a) presents data from one experiment, where an equivalent of ∼ 0.5 ML HBC is deposited on a clean surface. The sample is slowly annealed over several hours and imaged at room temperature ∼ 28 h after molecule deposition. A coexistence of the island and bulk phase is directly visible in these data. Again, the volume and area ratios for both phases are determined from these data. The total molecular volume is measured to about 400 000 nm^3, with an island to bulk volume ratio of about 2 : 1. The total projected area is about 400 000 nm^2, with an

island to bulk area ratio of about 12 : 1. These ratios clearly demonstrate the increase of the HBC island growth at the expense of three-dimensional bulk growth when using the variable-temperature preparation.

6.1.4. Island morphology

The islands exhibit an elongated shape oriented along two principle directions, as evident from Figure 6.4. The two island domains draw an angle of $(120 \pm 2)°$ to each other. When considering the substrate orientation, especially the [01.0] direction which is indicated in Figure 6.4(a), it can readily be assumed that the two island directions are related to each other at least by a glide reflection. Consequently, each island type is assumed to draw an angle of $(60 \pm 1)°$ with the [01.0] substrate direction. This axis might, at the same time, be the glide axis. The existence of this symmetry is a surprising result, as this symmetry does not exist on the $CaCO_3$(10.4) surface as long as the CO_3 group orientation is not neglected.

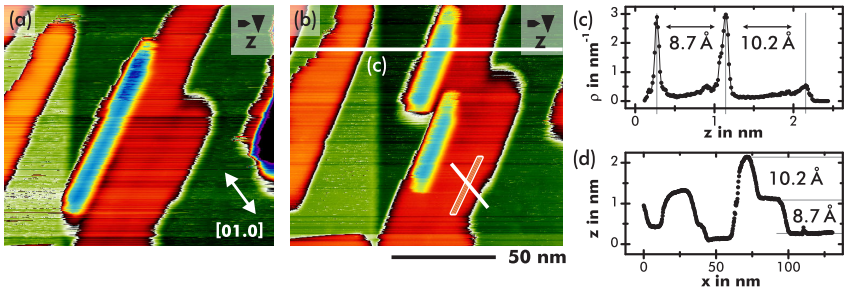

Figure 6.5.: Island layout and evolution for the HBC/$CaCO_3$(10.4) system. NC-AFM images (a) and (b) are separated by ∼ 51 min. The height distribution in (c) is extracted from a subpart on the lower terrace in (b).

Figure 6.5 presents detailed views of several islands. Subfigures (a) and (b) present images acquired consecutively with a ∼ 51 min separation. A significant island reorganisation is apparent on both, the first and second layer of the island structure. This finding is in agreement with the before determined diffusion barrier of $E_d \approx (0.5 \pm 0.1)$ eV and, furthermore, it constrains the intermolecular binding energy to a value smaller than 0.7 eV.

The islands are imaged with a height in the order of 1 nm as measured from the height distribution and line profile in Figures 6.5(c) and (d), respectively. This height is in the order of the HBC molecular width as shown in Figure 6.1(b). Consequently, an upright orientation of the HBC molecules is suggested. This suggestion of upright oriented HBC molecules in the island phase is further confirmed from studying the detailed island structure. This is discussed in the next section based on high-resolution NC-AFM data from one molecular island.

6.1.5. Detailed island structure

The high-resolution data in Figure 6.6 are acquired in the true constant-height mode provided by the atom-tracking system (see Chapter 4 for details on this measurement technique). The tip-sample distance is successively decreased from Subfigure (a) to (e), spanning a Z-range of about 3 Å. The Z-position for each image is indicated in the $\Delta f(z)$ data in Figure 6.6(f). These $\Delta f(z)$ curves are recorded at positions indicated in Figures 6.6(d) and (e). A slight tip-reconfiguration occured between Subfigures (d) and (e), thus curve A describes the interaction for data (a) to (d), while curve B is taken on the bright spot indicated in Figure 6.6(e). Both $\Delta f(z)$ curves A and B are nearly congruent except for the minimum region, however, the imaging contrast increased in quality in Figure 6.6(e).

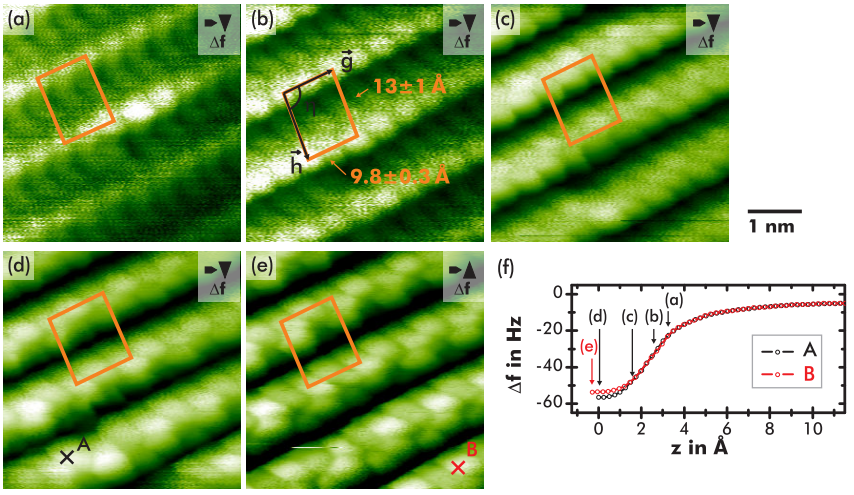

Figure 6.6.: True constant-height NC-AFM data acquired on one island domain. The tip-sample distance is decreased from (a) to (e) as indicated in the $\Delta f(z)$ curves in (f). The unit cell of the molecular structure is indicated in all images.

In all images, a nearly rectangular unit cell of the molecular structure is apparent. From these and other high-resolution NC-AFM data, side lengths of $g = (13 \pm 1)$Å and $h = (9.8 \pm 0.3)$Å with an inner angle of $\eta = (94 \pm 3)°$ are measured. When considering the long-range contrast in Figure 6.6(a) only, the drawn supercell appears to be non-primitive. However, high-resolution data at decreased tip-sample distances in Figure 6.6(e) reveal a different orientation of every second HBC molecule, thus, two neighbouring HBC molecules are assumed to differ slightly in their configuration.

For the unit cell vectors $\vec{g}, \vec{h}$ and $\vec{g}', \vec{h}'$ of each island domain and the unit cell

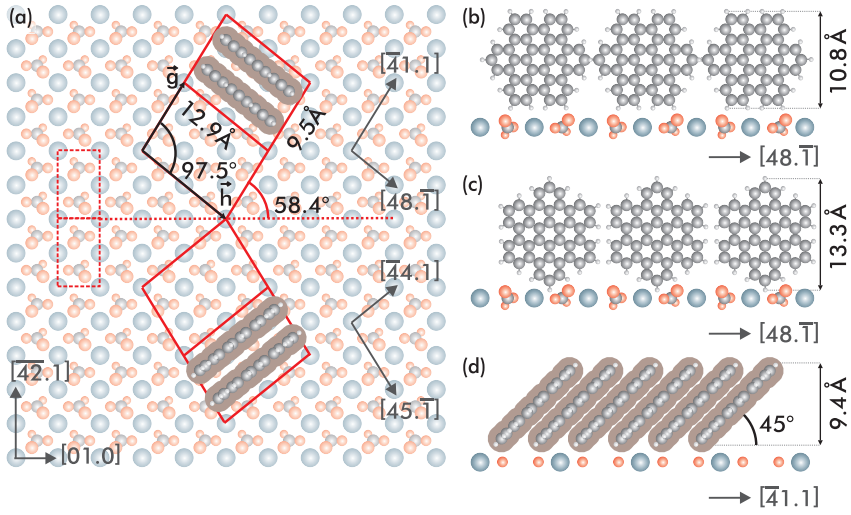

Figure 6.7.: Model for the HBC island phase on the $CaCO_3(10.4)$ surface. (a) Depicts both island domains, the molecular structure here is related by a mirror symmetry with the [01.0] direction as the mirror axis. (b) And (c) depict two possible high-symmetry orientations of the HBC molecules. Most likely, the molecules are tilted by 45°, as analysed in Figure 6.8.

vectors $\vec{a},\vec{b}$ of the (1×1) $CaCO_3(10.4)$ surface unit cell, the superstructures are described by two matrices $\hat{\mathbf{M}}$ and $\hat{\mathbf{M}}'$ via the relations

$$\begin{pmatrix}\vec{g}\\ \vec{h}\end{pmatrix}=\hat{\mathbf{M}}\begin{pmatrix}\vec{a}\\ \vec{b}\end{pmatrix} \qquad \begin{pmatrix}\vec{g}'\\ \vec{h}'\end{pmatrix}=\hat{\mathbf{M}}'\begin{pmatrix}\vec{a}\\ \vec{b}\end{pmatrix} \tag{6.1}$$

Reflecting the experimental data, the following matrices are suggested:

$$\hat{\mathbf{M}}=\begin{pmatrix}1 & 1\\ 2 & -1\end{pmatrix} \qquad \hat{\mathbf{M}}'=\begin{pmatrix}1 & -1\\ 2 & 1\end{pmatrix} \tag{6.2}$$

for each island domain. Due to the rotation of the CO_3 groups of the calcite substrate, the two island orientations are as a matter of fact not congruent. If neglecting the substrate, both orientations bear a mirror symmetry with respect to the [01.0] substrate direction as depicted in Figure 6.7(a). The superstructure unit cell size of $9.5\,\text{Å}\times12.9\,\text{Å}$ is in excellent agreement with the experimental data, and the inner angle of 97.5° is virtually identical to the measured value within the experimental uncertainty. In further agreement to the experimental data from Figure 6.6, two molecules are located within one unit cell. For these

two molecules, the orientation of the CO_3 groups and the calcium ions beneath the lower molecule centre is different as is apparent from the model. This fact might lead to a different adsorption position and is, therefore, is in agreement with the different appearance of the two molecules in Figure 6.6(e).

In this model for the adsorption geometry, the orientation of the HBC molecules as well as their angle drawn with the surface plane remains unclear. Two high-symmetry orientations for the molecular orientation are "long-side down" (depicted in Figure 6.7(b)) and "peak-side down" (Figure 6.7(c)). Using a simple argument based on steric reasons, the "peak-side down" orientation appears more likely, as in the "long-side down" orientation the peak sides overlap considerably as visible in Figure 6.7(b).

To elucidate the angle between the molecular and the sample surface plane, simple calculations[3] for a molecular HBC pair in vacuum are performed. The calculations use a pairwise empirical interaction potential of the Lennard-Jones type $V_{ij}(r_{ij}) = 4\epsilon_{ij}\left[(\sigma_{ij}/r_{ij})^{12} - (\sigma_{ij}/r_{ij})^{6}\right]$ for all involved atoms. The parameters derived for hydrocarbon systems by Stuart *et al.* [200] are used. This model has already been adapted successfully for the HBC/Au(111) system by Ruffieux *et al.* [172], where the optimum adsorption geometry of a second HBC layer has been calculated.

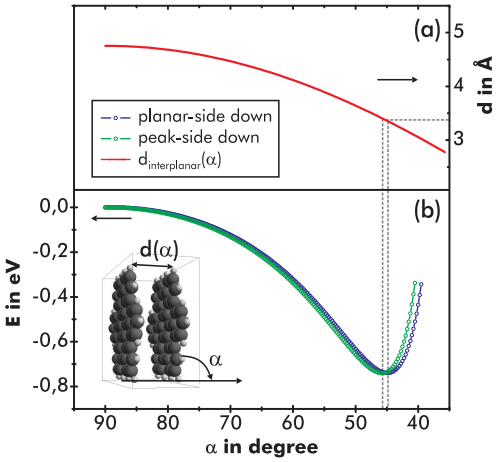

Figure 6.8.: Results from modelling the HBC island structure. (b) The system energy of two HBC molecules calculated in dependence on their tilt angle. For both high-symmetry configurations "peak-side" and "long-side down", a virtually similar energy minimum is found. (a) The interplanar distance in dependence on the tilt angle.

The results of this calculation are presented in Figure 6.8. For both geometries, "peak-side" and "long-side down", the total energy of a molecular pair is calculated as a function of the tilt angle α. The geometric model and the definition of α are included in the inset of Figure 6.8(b), exemplary for the "long-side down" ge-

[3] Mathematica (Wolfram Research, Champaign, IL, USA) is used to evaluate the respective equations.

ometry. The graph in Figure 6.8(a) denotes the HBC interplanar distance for a specific angle. This distance is calculated from simple geometric considerations. For both HBC geometries, the calculated energy is virtually the same (please note that no adjacent row is considered in this calculation). The energy minimum is found for an angle of $(44.3 \pm 0.2)°$ ($(45.0 \pm 0.2)°$) for peak-side (long-side) down, respectively. At these angles, the interplanar HBC distance amounts to (3.32 ± 0.02)Å ((3.36 ± 0.02)Å) for the peak-side (long-side) down geometry, respectively. This distance is comparable to the intermolecular distance of 3.42 Å in the monoclinic bulk structure [76].

6.1.6. Conclusions

HBC molecules deposited on a $CaCO_3$(10.4) surface held at 300 K feature predominantly bulk growth. Using a variable-temperature preparation recipe it was, however, possible to force the formation of an island phase. The structure of this island phase was analysed using high-resolution NC-AFM data and two domains were revealed. Each domain forms a commensurate superstructure, formed by columnar stacked HBC molecules. The inner structure of the two domains is presumably related by a mirror symmetry to each other, with the [01.0] direction forming the mirror axis. The NC-AFM data and simple model calculations suggest furthermore a tilt of the HBC molecules by about 45°, thus reducing the interplanar distance to nearly the bulk value. A diffusion barrier of $E_d \approx (0.5 \pm 0.1)$ eV was estimated from variable temperature experiments and the intense island reorganisation observed at 300 K suggests a value smaller than 0.7 eV for the intermolecular binding energy E_{inter}. In conclusion, the variable-temperature preparation succeeded in the formation of flat-lying HBC columns, making this system potentially interesting in the context of molecular wire formation.

6.2. Fullerene C_{60}

In a second study, the interaction and growth characteristics of C_{60} fullerenes deposited on $CaCO_3$(10.4) surfaces are investigated. Fullerenes constitute one of the well-known modifications of carbon and encompass the class of all spherical molecules formed exclusively by carbon atoms. The C_{60} molecule itself is one of the most prominent representative of this class, after its initial discovery in 1985 by Kroto *et al.* [107]. A schematic representation of the C_{60} molecule is drawn to scale to the $CaCO_3$(10.4) surface in Figure 6.9. Within the molecule, a total of 60 carbon atoms are aligned at the 60 vertices of a truncated icosahedron.

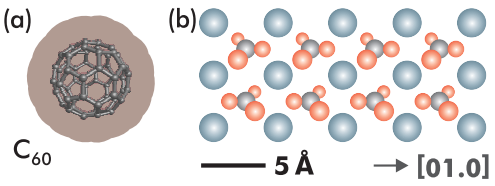

Figure 6.9.: Structural model of the C_{60} molecule (b), drawn to scale to the $CaCO_3$(10.4) surface (a). Black spheres: carbon, red spheres: oxygen and blue spheres: calcium. The 10 Å van-der-Waals radius of the C_{60} fullerene is depicted by a brownish shade.

6.2.1. Introduction

The bulk structure of C_{60} is face-centred cubic (fcc) with $a_{0,\mathrm{fcc}} = (14.17 \pm 0.01)$ Å at room temperature and under normal pressure conditions [86]. However, Heiney *et al.* [86] identified a phase transition from a simple cubic (sc) to the fcc phase at a temperature of (249 ± 1) K. This low-temperature simple cubic phase consists of a four-molecule basis with $a_{0,\mathrm{sc}} = (14.04 \pm 0.01)$ Å (at 11 K). The pressure-dependence for this phase transition temperature has been analysed by Samara *et al.* [179].

The adsorption characteristics and growth properties of C_{60} molecules on conducting, semiconducting and insulating substrates attracted notably interest during the last two decades. Interestingly, the interaction of C_{60} molecules with different substrates has been reported to range from weak van-der-Waals interaction on dielectric surfaces over ionic interaction on metal surfaces to strong covalent bond formation on semiconducting substrates [131]. Reflecting the discussion on surface energies in Chapter 2, layer-by-layer growth and, eventually, the formation of ordered overlayers is expected and reported for numerous C_{60}/metal systems. An overview discussing various substrates has been given by Maxwell *et al.* [131].

Going to insulating substrates, the adsorption of C_{60} molecules has been investigated by Burke *et al.* [34] on the alkali halides KBr(100) and NaCl(100), where

the molecules undergo a dewetting process and form unusual island morphologies. Loske [122] investigated the growth of C_{60} molecules on $CaF_2(111)$ surfaces, where also compact and branched island morphologies have been found. The formation of these different morphologies has recently been modelled by means of a kinetic monte carlo study [106].

6.2.2. Morphology on calcite

C_{60} molecules are sublimated from a heated crucible under ultra-high vacuum conditions, further details were given in Section 3.2.4. An overview image acquired by means of NC-AFM is depicted in Figure 6.10, where the equivalent of ~ 1.5 ML is deposited onto a clean $CaCO_3(10.4)$ surface. Two step edges of the $CaCO_3$ substrate run roughly along the vertical direction in this image with a horizontal separation of about 300 nm. They are visualised by superimposed dotted lines. These step edges provide *nucleation* centres for the C_{60} molecules, as is directly evident from the data. This behaviour of nucleation at step edges is well-known for weakly bound systems and has, for example, been utilised to form rectangular molecular structures on an electron irradiated KBr substrate [144, 145].

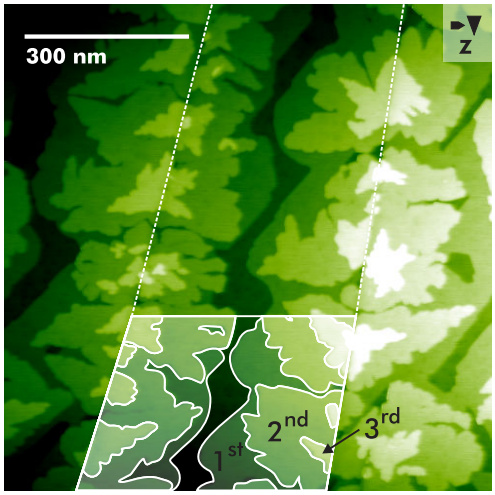

Figure 6.10.: Large-scale morphology of the $C_{60}/CaCO_3(10.4)$ system. Two calcite step edges are present in this image and visualised by dotted lines. The different C_{60} layers are marked in the lower part.

In the lower half of the image, the height and shape of different C_{60} molecular layers between the step edges is visualised. From this NC-AFM data, a layer height of about (9 ± 1)Å is measured. Despite of the errors in NC-AFM height measurements as discussed in Section 3.4, this value is in good agreement with previously measured heights of single layer C_{60} islands on KBr or NaCl surfaces [34]. Furthermore, this height is comparable to the (111)-interplanar distance in the C_{60} fcc bulk structure. The latter value is calculated to 8.2 Å using the bulk parameters

from Heiney *et al.* [86]. Likewise, the nearest-neighbour distance in the C_{60} bulk fcc lattice is given to 10.0 Å. Thus, the observed structures are unambiguously assigned to single layers of C_{60} molecules.

The data presented in Figure 6.10 suggest a layer–by–layer (Frank–van–der–Merwe) growth mode for the $C_{60}/CaCO_3(10.4)$ system. Additionally, the first layer is constrained by smooth, wetting-like island boundaries. It is interesting to note that no rim or branched structures are present, in contrast to earlier observations of C_{60} on $CaF_2(111)$ and other insulating substrates. This finding is, however, in complete agreement with the analysis presented in Chapter 2. For the $C_{60}/CaCO_3$ system, an interface energy[4] of up to $0.47\,Jm^{-2}$ is allowed until layer–by–layer growth is no more the thermodynamically favoured growth mode. This comparable large value is promoted by the rather large surface energy of the $CaCO_3(10.4)$ surface as outlined in Chapter 2. Consequently, molecular bulk phase formation is supressed and, therefore, a dewetting process. This is in sharp contrast to findings for the C_{60}/KBr(100), C_{60}/NaCl(100) or $C_{60}/CaF_2(111)$ systems [34, 123, 122], where a small substrate surface energy promotes molecular bulk growth, eventually through a dewetting process.

Thus, for the $C_{60}/CaCO_3(10.4)$ system at room temperature and at a coverage of more than 1 ML, the presumption from Chapter 2 is confirmed here. This finding constitutes a significant step towards 2D molecular structure formation on a dielectric surface.

6.2.3. Detailed structure

In order to elucidate the detailed adsorption geometry, high-resolution NC-AFM imaging on a C_{60} multilayer is performed. From one experiment, the results are presented in Figure 6.11. A nearly hexagonal structure with a neighbour-neighbour distance of (10.0 ± 0.5)Å is observed and, additionally, a modulation pattern with a periodicity of (61 ± 7)Å is found. These values are given from the two-dimensional Fourier transformation (2D-FT) as reproduced in Figure 6.11(c). They are additionally confirmed by further AFM data (not shown) under careful consideration of thermal drift. The corrugation along Z of the C_{60} molecular lattice is measured to ~ 7 pm, and this value is slightly larger than the corrugation of the modulation pattern, which is ~ 5 pm. Both values are measured in the line profile in Figure 6.11(d), which is extracted from the indicated position in Figure 6.11(b).

The measured C_{60} neighbour-neighbour distance of (10.0 ± 0.5)Å is in excellent agreement with a twofold substrate periodicity along the [01.0] substrate direction. This distance is given from the surface unit cell size to 10 Å. Consequently, it can readily be assumed that the modulation pattern is oriented parallel to the

[4] The value is calculated by using the surface energies listed in the Appendix Section A.

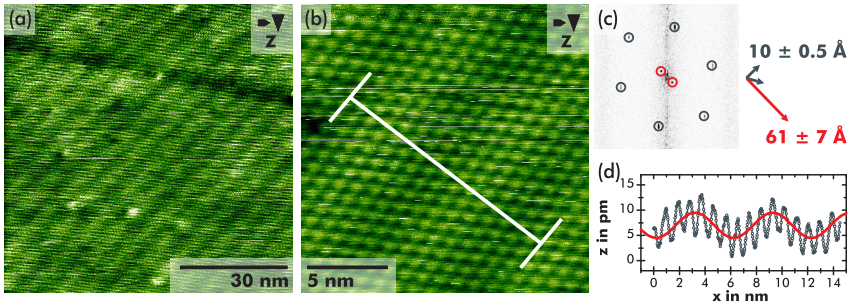

Figure 6.11.: NC-AFM images of the $C_{60}/CaCO_3(10.4)$ system. The 2D-FT data in (c) are calculated from the AFM topography image (a) and identify a nearly hexagonal structure and a modulation pattern. (b) Presents a zoom into the structure presented in (a). Individual C_{60} molecules are clearly resolved. The white line indicates the averaged line profile extracted in (d).

[01.0] substrate direction. Under this assumption, the hereunto perpendicular modulation direction is oriented along the $[\overline{4}2.1]$ direction. From the the measured periodicity of (61 ± 7)Å, this fact reveals a 7.5 fold superstructure with a length of $7.5 \times b = 60.7$Å. The resulting molecular arrangement for this proposed structure is depicted in Figure 6.12 and all measured dimensions are in excellent agreement with the experimental observed values. However, the structure suggests that the correct superstructure is doubled along the $[\overline{4}2.1]$ direction, due to an uneven number of C_{60} molecular rows in the 7.5 fold superstructure. The primitive unit cell for the superstructure is, thus, (2×15) with dimensions 10×121.4Å^2. The unit cell contains a total of 14 molecules, each in a slightly different binding situation to the underlying $CaCO_3(10.4)$ surface. The latter finding likely results into the observed modulation pattern. Please note that the absolute positions of the adsorbed molecules as depicted in Figure 6.12 are arbitrarily chosen.

The layout of the observed superstructure reminds of a (111) plane of the fcc bulk structure, extended by an additional modulation pattern. For the resulting 15 fold superstructure, the lattice constant mismatch along $[\overline{4}2.1]$ compared with a (111) plane is as small as ~ 0.3 %. When neglecting the modulation pattern, the C_{60} would arrange in an oblique structure with unit cell dimensions $c = 9.98$Å, $d = 10.00$Å and $\epsilon = 119.9°$ as depicted in Figure 6.12. The unit cell sizes of this oblique structure bear a mismatch of ~ 0.2 % to a perfect hexagonal structure.

6.2.4. NC-AFM imaging process

In this last section, the NC-AFM imaging process on a C_{60} monolayer is analysed. In a study by Loske *et al.* [124], where the growth of C_{60} islands on a $TiO_2(110)$

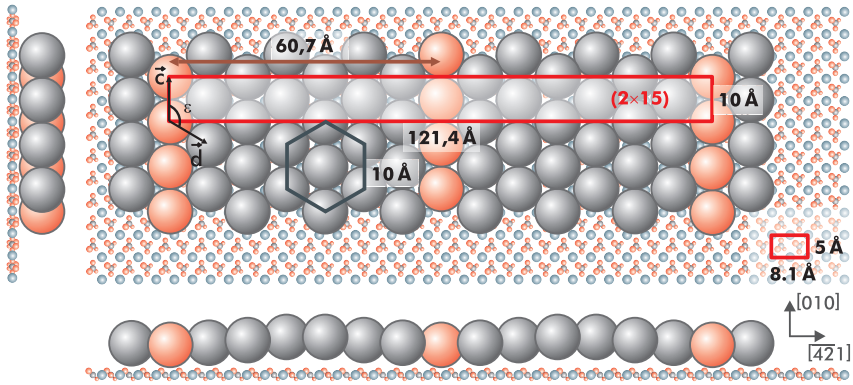

Figure 6.12.: Adsorption model proposed for the $C_{60}/CaCO_3(10.4)$ system. A (2×15) superstructure is evident from the AFM experiments. Note that the absolute positions of the C_{60} molecules are arbitrarily chosen and that the modulation in Z is exaggerated for visualisation purposes.

surface has been investigated, we reported upon a contrast inversion in NC-AFM imaging of the ordered C_{60} structure. This contrast inversion is visible in data acquired in different interaction regimes: While at large tip-sample distances (large z), the centre of each C_{60} molecule is imaged bright, the positions in-between the molecules appear brightest at smaller z. The contrast evolution has been explained by crossing points of $\Delta f(z)$ curves from different sample sites. This finding has been corroborated by myself using model calculations, where a specific C_{60}–C_{60} interaction potential has been employed to calculate the full Δf interaction field. The results revealed the exact crossing points in the interaction curves as found experimentally. Furthermore, it was expected that the contrast formation mechanism is mainly independent of the substrate and, thus, a similar effect is expected for the $C_{60}/CaCO_3(10.4)$ system. This statement will be confirmed by means of quasi constant-height frequency shift data as presented in Figure 6.13.

In this AFM image scanned from the top to the bottom line, the Δf setpoint is gradually increased. This increases the tip-sample interaction and decreases the tip-sample distance z. The mean Δf for each sector is given in the right column, all data are acquired in the attractive regime [161]. The superimposed lines and circles directly visualise a contrast inversion [161]. Here, the contrast evolves as follows: At large tip sample distances (regime I), the centre of a bright spot is assigned to the centre of a single C_{60} molecule. When decreasing the tip-sample distance, at first a section is reached where the contrast is virtually absent ($\Delta f = -16.5\,\mathrm{Hz}$). At even smaller tip-sample distances (regime II), the contrast changes to a waffle-like structure with the centre of each C_{60} molecule lying in

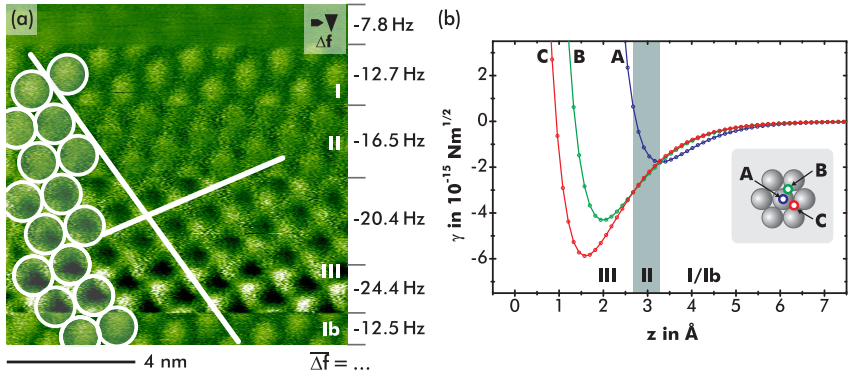

Figure 6.13.: Contrast inversion in the imaging process on a C_{60} layer with the NC-AFM. (a) The mean frequency shift $\overline{\Delta f}$ for each sector is given in the right column. A line correction algorithm was used for improved data visualization. The superimposed circles denote the positions of single C_{60} molecules and the lines are aligned at the hollow sites. (b) Theoretical results for three $\gamma(z)$ interaction curves.

the dark waffle-centre. Upon further decreasing the tip-sample distance, the positions between the C_{60} molecules appear brightest, now these sample sites present the largest attractive interaction (regime III). To demonstrate the reproducibility of this contrast formation, the last lines (regime Ib) are imaged again at a similar interaction as was chosen for the first lines and they reproduce the contrast in regime I.

The explanation for this contrast formation is in agreement with the explanation for the $C_{60}/TiO_2(110)$ system [124]. However, the precise exposition of the interaction behaviour depends on the different adsorption geometry of the $C_{60}/CaCO_3(10.4)$ system. In particular, the sector between regimes I and II, where the imaged corrugation is highly reduced, has not been observed before for the $C_{60}/TiO_2(110)$ system. Figure 6.13(b) presents simulated interaction data[5] for the $C_{60}/CaCO_3(10.4)$ system. Three interaction curves in form of the normalised frequency shift γ [67] are presented. This quantity γ is proportional to the frequency shift Δf, but it is independent of the cantilever parameters. Curve A is calculated for the C_{60} on-top position, curve B for the hollow position between two molecules and curve C at the hollow position between three molecules. These positions are indicated in the inset of Figure 6.13(b).

In agreement with the $C_{60}/TiO_2(110)$ system, crossing points are found and separate the interaction regimes I to III. The sample position imaged "brightest"

[5]The same model with the potential derived by Feng-Ling *et al.* [59] from the previous work published by Loske *et al.* [124] is used here. The only difference is the C_{60} geometry, as the (2×15) superstructure formed on calcite is modelled herein.

is always found from the curve with the smallest γ-value. With this interpretation, the contrast formation in regimes I to III is directly explained: In regime I, position A yields the smallest interaction, in regime II, positions B and C are virtually similar but inhibit a smaller γ value compared to position A. Last, position C yields the smallest γ in regime III. Consequently, the C_{60} centre is imaged brightest in regime I and the hollow positions are imaged brightest in regime II with the C_{60} centre position being dark. In regime III, the position between three molecules is imaged brightest.

Interestingly, for the specific tip-sample distance where all three $\gamma(z)$ curves intersect, no contrast of the molecular structure is expected. This finding is in agreement with the experimental data at a Δf setpoint of about $-16.5\,\mathrm{Hz}$. This section has not been found for the $C_{60}/TiO_2(110)$ system as, due to a different adsorption geometry, no $\gamma(z)$ crossing point exists for all three curves.

6.2.5. Conclusions

The NC-AFM data suggest a molecular growth in the layer–by–layer mode. This finding is in full agreement with the initial analysis in Chapter 2 and indicates the advantage of using $CaCO_3(10.4)$ as a substrate for studying molecular self-assembly compared to other dielectric surfaces. Additionally, the $CaCO_3(10.4)$ surface is, to the authors best knowledge, the first dielectric substrate where no dewetting of the C_{60} fullerenes is observed at room temperature.

High-resolution NC-AFM data revealed a (2×15) superstructure for the C_{60} molecules, with 14 C_{60} molecules inside the unit cell. The molecules arrange in a nearly hexagonal pattern, which is extended by a modulation with a periodicity of 121.4 Å. The lattice mismatch to a (111) plane of the C_{60} fcc bulk structure is as small as $\sim 0.3\,\%$. The existence of the large superstructure including the modulation clearly indicates the templating effect of the underlying substrate on the molecular structure.

A similar contrast inversion mechanism in NC-AFM imaging was found, as has been observed before for the $C_{60}/TiO_2(110)$ system. Interestingly, due to the C_{60} adsorption geometry herein, the analysis revealed one specific tip-sample distance where the corrugation is virtually absent. For this specific distance, the C_{60} molecular structure is invisible to the NC-AFM.

6.3. Terephthalic acid

The results presented for the $C_{60}/CaCO_3(10.4)$ system in Section 6.2 are promising when aiming at self-assembly of complex molecular structures on dielectric surfaces. However, the large diffusion rate at room temperature still inhibits a stable structure to be formed, most prominent due to small diffusion barriers and small intermolecular binding energies. Therefore, other interactions than weak van-der-Waals attraction are necessary.

The addition of carboxylic acid moieties to organic molecules has led to the formation of complex network structures on conducting substrates [20]. Furthermore, studying the adsorption of stearic acid molecules on $CaCO_3$ surfaces yielded comparable high binding energies supported by the carboxylic acid moieties [50].

Consequently, I choose planar organic molecules with carboxylic acid groups as promising candidates for an increased intermolecular interaction and, potentially, even a bond-formation with the underlying substrate. Two aromatic carboxylic acids are studied within this thesis, namely terephthalic acid (TPA, $C_8O_4H_6$) and trimesic acid (TMA, $C_9O_6H_6$). I start in this section with the $TPA/CaCO_3(10.4)$ system and defer the discussion of the TMA molecule to Section 6.4. A schematic representation of the TPA molecule, which consists of a central benzene with two carboxylic acid groups in a *para* configuration, is given in Figure 6.14. The molecule is drawn to scale to the $CaCO_3(10.4)$ surface.

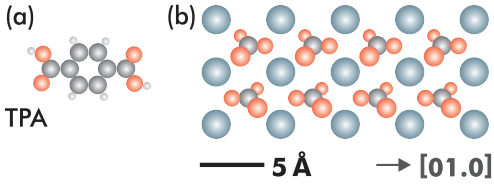

Figure 6.14.: Terephthalic acid (a) drawn to scale to the $CaCO_3(10.4)$ surface (b). Black spheres: carbon, white spheres: hydrogen, red spheres: oxygen and blue spheres: calcium.

6.3.1. Introduction

Terephthalic acid (TPA) is a versatile molecular linker and has, consequently, received considerable attention with regard to the assembly of three-dimensional self-assembled porous frameworks stabilised by metal-carboxylate bonds [225] as well as in two-dimensional supramolecular architectures at surfaces [196, 195, 19, 39, 42, 163, 154].

Bailey and Brown [14] have investigated the TPA bulk structure by means of X-ray diffraction. From their data, they have identified two triclinic forms, both presumably of space group $P\bar{1}$. For both forms, chains of TPA molecules linked via hydrogen bonds between two carboxylic acid groups are reported as the basal

unit. Along these molecular chains, the molecule-molecule distance has been measured to 9.54 Å.

This self-complementary linking via the carboxylic acid groups is, consequently, the common motif found when studying the TPA superstructures on substrates such as HOPG [112], Pd(111) [39] or Au(111) [42]. The structure formation changes substantially when the TPA molecules are deprotonated, which has, for example, been presented in experiments on Pd(111) [39] and Cu(100) [196]. On strongly interacting substrates, however, the molecular assembly of TPA has often been observed to be dictated by the surface structure. To name one prominent example, a full monolayer of TPA molecules on a TiO_2(110) substrate favours an upright orientation as has first been observed by Tekiel *et al.* [208]. In cooperation with the group of [Name removed][6], we have investigated the submonolayer coverage of TPA on TiO_2(110) in a combined NC-AFM and Near Edge X-ray Absorption Fine Structure (NEXAFS) experimental study. From the NEXAFS experiments, it was possible to unambiguously identify a structural transition from flat-lying molecules at sub-monolayer coverages to upright-standing molecules at monolayer coverage. Interestingly, the formation of TPA multilayers evinced to be hindered. The results of this study have been published in the *Journal of Physical Chemistry C* [163].

6.3.2. Adsorption at room temperature

In a first experiment, a submonolayer coverage of TPA is deposited on a clean $CaCO_3$(10.4) surface at room temperature. After TPA deposition, the sample is transferred to the AFM. From this experiment, two consecutively acquired images are presented in Figure 6.15(a) and (b) (acquisition time per image ~ 8.5 min). At this coverage of less than a monolayer, islands with fuzzy outlines are observed. To visualise the island reorganisation, two of the island outlines are highlighted in Figure 6.15(a) by white lines. These outlines are copied[7] to Subfigure (b) and, thus, directly map the island reconfiguration.

The inner structure of these islands bear a well-defined pattern. From several two-dimensional Fourier transform (2D-FT) data (one shown in Figure 6.15(c)), a rectangular unit cell of size $(10.0 \pm 0.2) \times (16.3 \pm 0.4)$ Å^2 is measured. This unit cell, which is also indicated in the real-space domain in Figures 6.15(a) and (b), is in excellent agreement with a (2×2) superstructure, having a unit cell size of 9.98×16.19 Å^2.

The TPA diffusion limits the high-resolution capabilities of the NC-AFM technique. This is circumvented by either immobilising the molecules at reduced temperatures or upon forming a full monolayer. Figure 6.16 presents NC-AFM

[6] Institute of Functional Interfaces, Karlsruhe Institute of Technology, Karlsruhe, Germany

[7] Due to image distortions induced by thermal drift, the outlines are realigned with respect to the fixed features.

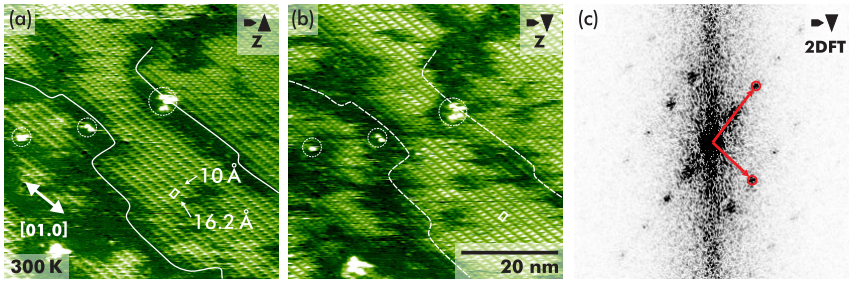

Figure 6.15.: (a) And (b) consecutive images taken at a sample temperature of 300 K. Three immobile features are marked as a reference. The outline of two island structures is highlighted. (c) Central part of the 2D-FT from (b).

results where the latter ansatz is followed. A molecular coverage[8] of slightly more than one monolayer is deposited and, as directly apparent from the image, the molecular structure becomes immobile.

The overview NC-AFM image in Figure 6.16 clearly suggests a layer–by–layer growth mode for the TPA molecule on the $CaCO_3$(10.4) surface. The calcite substrate is completely covered by a (2×2) phase, as will be analysed in Section 6.3.3. However, a second phase forming molecular islands of increased height is present. The inner structure of this second phase suggests a much denser molecular packing. This phase mainly nucleates at calcite step edges, however, at the lowest terrace in Figure 6.16(a) several islands are observed apart from step edges. They appear to nucleate at one corner of a TPA domain boundary. These domain boundaries are identified as dense stripes parallel to the [01.0] direction, few are marked by white arrows in Figures 6.16(a) and (b). They will be discussed in Section 6.3.3.

The island height of the second phase is measured in Figure 6.16 to (7 ± 1)Å relative to the TPA monolayer. Although the absolute height measured with the NC-AFM technique is usually questionable (see Section 3.4 for details), the measured height is here in-between the expected dimensions of flat-lying (~ 3Å) and upright-standing (~ 10Å) TPA molecules. Therefore, it cannot be clarified unambiguously whether the second phase is formed by a second molecular layer or by upright standing molecules embedded in the first (2×2) layer. However, I will exclusively focus on the predominant (2×2) phase in this thesis.

6.3.3. Structural model

The above mentioned (2×2) superstructure is clearly revealed from NC-AFM data acquired on a full monolayer, as will be discussed in detail in the following. The

[8] One monolayer is defined as two TPA molecules per (2×2) unit cell.

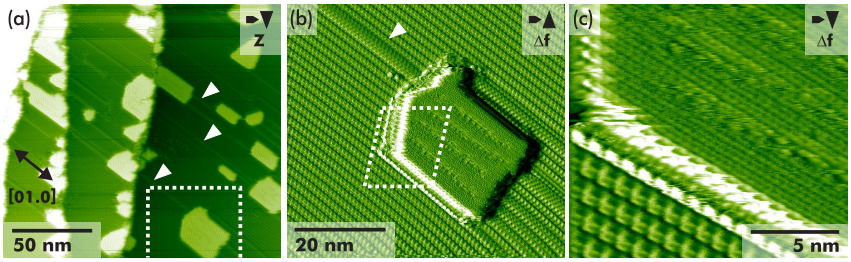

Figure 6.16.: (a) Immobile TPA superstructure imaged on a $CaCO_3(10.4)$ surface. The structure is stabilised by depositing slightly more than one monolayer of TPA molecules. (b) And (c) are detailed images acquired at the positions indicated in (a) and (b), respectively. (c) Is distorted due to thermal drift.

measured dimensions of the unit cell agree excellently with the island structure observed at submonolayer coverages. Thus, for this phase no coverage dependence of the adsorption structure is expected and the results for the full monolayer are assumed to agree with the structure at submonolayer coverages. Figure 6.17(a) presents a high-resolution image from a part of the data shown in Figure 6.16(a).

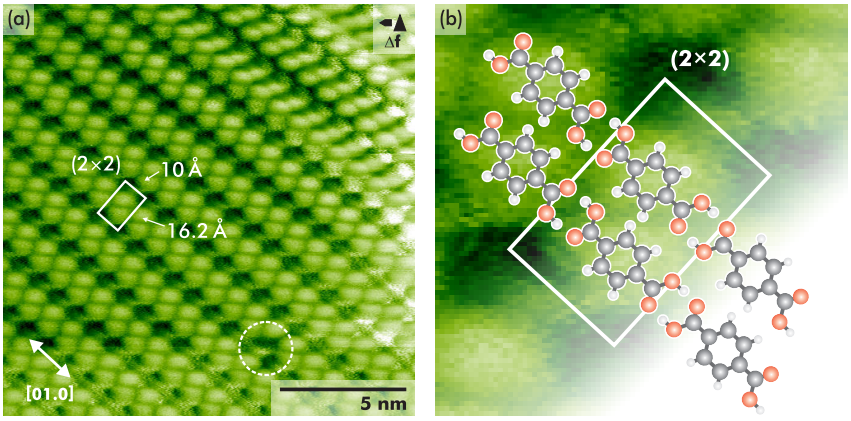

Figure 6.17.: Structure of the TPA (2×2) superstructure on a $CaCO_3(10.4)$ surface imaged at room temperature. (a) Detail image including a single molecular defect. (b) Structural model consisting of two chains of TPA molecules. These chains form the basal motif in the TPA bulk structure.

The detailed view at the molecular structure in Figure 6.17(a) reveals molecular double *chains* oriented along the [01.0] substrate direction. Each of these chains

is likely formed by flat-lying TPA molecules. The molecules along one chain are presumably linked by hydrogen bonds between two carboxylic acid groups as visualised in the structural model in Figure 6.17(b). The observed periodicity of 10 Å fits excellently to this geometry, it is angreement to the two-fold superstructure along a and, furthermore, it resembles the TPA bulk structure. Compared to the bulk structure [14], however, the hydrogen bonds in the TPA/$CaCO_3$(10.4) structure are slightly stretched by ~ 45 pm due to a lattice mismatch of ~ 5 % between the TPA bulk and $CaCO_3$(10.4) superstructure dimension.

Usually, two adjacent chains are observed to pair to a molecular *ribbon*. This is additionally depicted in Figure 6.17(b) for two short molecular chains. These ribbons align with a periodicity of 16.19 Å along the $[\overline{42}.1]$ direction, accordingly to the two-fold superstructure along b. It should briefly be noted that the possibility of a double tip artifact in imaging single molecular chains can be ruled out due to the presence of single molecular defects (one is indicated in Figure 6.17(a)). The interchain interaction is presumably a mixture of weak hydrogen bonding between the carboxylic acid dimers and the hydrogen atoms at the benzene core as well as weak van-der-Waals forces between the involved molecules. Additionally, a significant influence of the calcite substrate is suggested, as the chains do not assemble in the most dense, but in a rather open fashion.

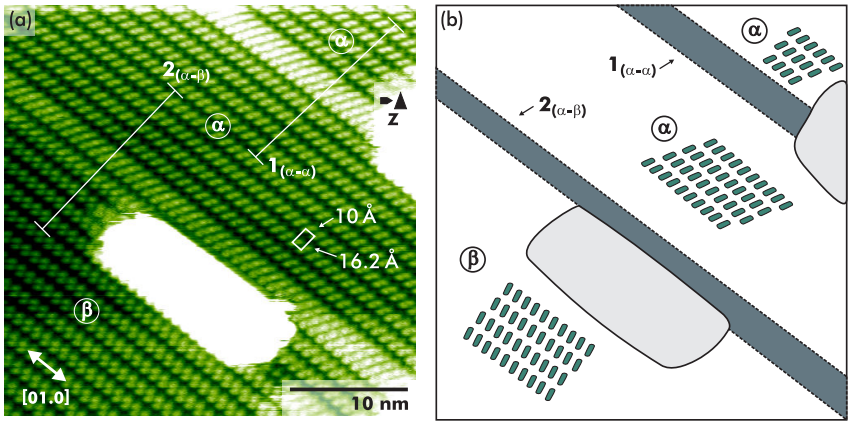

Figure 6.18.: (a) Domain boundary structure revealed for the TPA/$CaCO_3$(10.4) structure. (b) Is a schematic representation of NC-AFM image (a), revealing two domains α and β, two boundaries 1 and 2 and the (2×2) superstructure.

The data in Figure 6.18(a), which are another zoom into Figure 6.16(a), reveal two more characteristics which were not identified at submonolayer coverages. First, two domains for the (2×2) superstructure are revealed, namely α and β. The domains differ in their appearance due to a different chain orientation inside

the molecular ribbons as will be analysed later. Second, these domains are separated by boundaries formed by densely-packed TPA molecules. Two variants of these boundaries are possible and observed experimentally: One type separates two equal domains (herein named type $1_{(\alpha-\alpha)}$ and type $1_{(\beta-\beta)}$), while the second separates two different domains (type $2_{(\alpha-\beta)}$). The periodicity of the molecular structure along the [01.0] direction inside the domain boundaries agrees well with the (2×2) superstructure along this direction and, thus, the domain boundaries are most likely formed by dense arrangements of TPA chains.

For analysing the structure of domains α and β, it is instructive to measure the width of the domain boundaries. This length is equivalent to the separation of the TPA ribbons across the respective boundary. For the two boundaries marked in Figure 6.18(a), averaged line profiles extracted along the [$\overline{4}2$.1] direction are reproduced in Figure 6.19(a). The [$\overline{4}2$.1] direction is perpendicular to the boundary orientation.

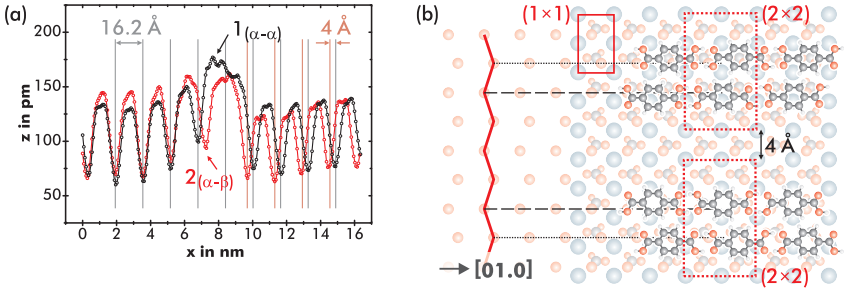

Figure 6.19.: (a) Two averaged line profiles from Figure 6.17(a). Profile 1 is extracted across a boundary with adjacent $\alpha-\alpha$ domains, while profile 2 separates domains $\alpha-\beta$. (b) Presents the refined adsorption model for the (2×2) superstructure. To the left, only the topmost oxygen atoms of the calcite substrate are depicted.

According to the (2×2) superstructure, the periodicity along [$\overline{4}2$.1] is 16.19 Å. This periodicity is visualised by vertical black lines in Figure 6.19(a). Interestingly, the lines match the molecular arrangement across boundary $1_{(\alpha-\alpha)}$, while for boundary $2_{(\alpha-\beta)}$, a shift of about 4 Å is found in these data. This shift at the ($\alpha-\beta$) boundary is in excellent agreement to a shift by $b/2$, where b is the $CaCO_3$(10.4) unit cell size along [$\overline{4}2$.1]. It is, thus, identical to the distance of two neighbouring topmost oxygen atoms along [$\overline{4}2$.1].

From this analysis, the structural model for the (2×2) superstructure is refined as proposed in Figure 6.19(b). Two of the TPA chains are observed to pair to a molecular ribbon by weak interchain interaction. In this configuration, the chains are slightly shifted against each other. The shift of the "upper" chain (see Figure 6.19(b)) can either be positive or negative, leading to the structure of do-

mains α and β. The drawing in this model suggests an influence of the topmost oxygen atoms, which, however, cannot be identified unambiguously from the current data.

6.3.4. Low temperature experiments

To further elucidate the structure formation, experiments are performed at reduced temperatures using submonolayer coverages of TPA. Figure 6.20 presents NC-AFM data where the equivalent of $\sim 5\,\%$ ML is deposited on a substrate held at a temperature of 90 K. The consecutive imaging is performed at a substrate temperature of 110 K.

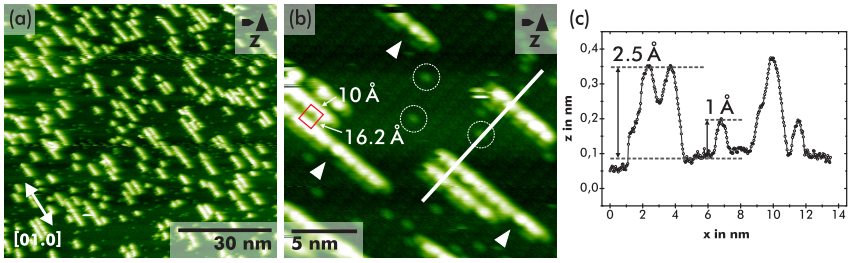

Figure 6.20.: NC-AFM data for the TPA/$CaCO_3$(10.4) system acquired at a sample temperature of 110 K. Before data acquisition, $\sim 5\,\%$ ML of TPA molecules are deposited on the substrate at a temperature of 90 K.

As apparent from these data, molecular chains are already formed at a temperature of 110 K. Thus, the diffusion barrier E_d for a single TPA molecule on calcite is smaller than 0.3 eV, using again the estimation presented in the Appendix Section E. The observed dimensions of the chains are in agreement with the TPA chain motif observed before, in which TPA molecules are linked via their carboxylic acid groups. The height of a single row measured from the line profile in Figure 6.20(c) amounts to ~ 2.5 Å. This finding supports the assumption of flat-lying TPA molecules, even under the uncertainties in NC-AFM height measurements (see Section 3.4). The molecular chains already align accordingly to the (2×2) superstructure, for visualisation purposes a (2×2) supercell is included in Figure 6.20(b).

Additionally to the molecular chains, the underlying substrate structure of calcite is faintly resolved in Figure 6.20(b). The contrast is presumably $\mathbf{V_4}$ and, therefore, both the row-pairing and the (2×1) reconstruction are visible. Details about the different calcite reconstructions are given in Chapter 5. Interestingly, all TPA chains observed in these data are well-aligned with the (2×1) calcite unit cell. In absence of the (2×1) reconstruction, random shifts of the adsorbed chains of

a along the [01.0] directions would be expected. As this is not observed in these data, a strong influence of the (2×1) surface reconstruction on the molecular arrangement is suggested.

In Figure 6.20(b), a second species besides the TPA molecules is observed. This species either resides on the bare calcite surface (few are highlighted by dotted circles), or it binds to a TPA chain. The imaged height of the free species is measured to ~ 1 Å as indicated in Figure 6.20(c). Interestingly, the species is observed only to bind to one side of the TPA chains, an asymmetry in agreement with the $CaCO_3$(10.4) surface properties. For the $CaCO_3$(10.4) surface, this asymmetry is entailed by the different carbonate group orientation. These data suggest that this property is propagated to the adsorbed molecular structure. An imaging or tip artifact for the adjacent species can be ruled out, as single defects (few marked by white triangles in Figure 6.20(b)) are observed. Presumably, these adsorbates are single water molecules originating from the background pressure [184].

6.3.5. Conclusions

In conclusion, the TPA molecules arrange themselves on the $CaCO_3$(10.4) surface predominantly forming a (2×2) superstructure. This structure is stabilised by molecular ribbons, while each ribbon is assembled from a pair of molecular chains. The structure of each chain agrees with the fundamental TPA bulk motif, but the hydrogen bonds are stretched by ~ 45 pm due to a lattice mismatch of ~ 5 %. The chaines are asymmetrical shifted against each other, which leads to two possible arrangements. Both arrangements were revealed in form of two domains on the $CaCO_3$(10.4) surface.

The diffusion barrier for a single TPA molecule is smaller than 0.3 eV as determined from experiments at 110 K. At this temperature, the chain formation already occures and, most interestingly, the single chains align themselves with respect to the calcite (2×1) reconstruction. Thus, a severe influence of the (2×1) reconstruction on the molecular structure is suggested.

6.4. Trimesic acid

The TPA/$CaCO_3$(10.4) system allowed for the successful two-dimensional molecular self-assembly on an insulating surface. However, the comparable small intermolecular binding energy E_{inter} together with a small diffusion barrier E_d still led to comparable instable submonolayer structures at room temperature. The system investigated in this Section bears the potential of an increased intermolecular binding energy due to a third carboxylic acid group compared to the TPA molecule. The molecule chosen is trimesic acid (TMA, $C_9O_6H_6$), a schematic representation is given in Figure 6.21.

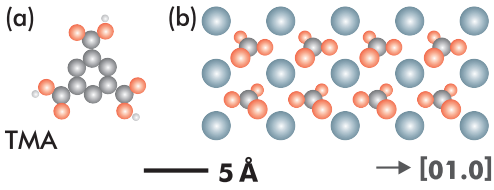

Figure 6.21.: (a) Trimesic acid (TMA) drawn to scale to the $CaCO_3$(10.4) surface (b). Black spheres: carbon, white spheres: hydrogen, red spheres: oxygen and blue spheres: calcium.

6.4.1. Introduction

The bulk structure of trimesic acid has been investigated by Duchamp and Marsh [49]. From X-ray diffraction data they found monoclinic crystals of space group $C2/c$ with $a = 26.52$ Å, $b = 16.42$ Å, $c = 26.55$ Å and $\beta = 91.53°$. The basis structural motif has been found as a continuous, two-dimensional network consisting of large rings formed by six TMA molecules. The stabilisation of this motif is provided by pairwise hydrogen bonds between the carboxylic acid groups.

TMA has been discussed as a molecular building block for highly ordered structures on conducting surfaces such as HOPG(0001) [128, 111, 77], Cu(100) [48], Au(111) [226] and Ag/Si(111) $-(\sqrt{3}\times\sqrt{3})$R30° [189]. On these surfaces, flat-lying TMA molecules form the characteristic "flower" and "chicken-wire" structures. Both structures are stabilised by hydrogen bonds between the carboxylic acid groups, however, the number of carboxylic acid groups involved in the bond formation differs. While the chicken-wire structure is stabilised by carboxylic acid dimers and is, thus, equivalent to the basis bulk motif, the flower structure involves an interaction between three carboxylic acid groups. The latter structure allows a denser packing of TMA molecules compared to the chicken-wire motif.

6.4.2. Adsorption on calcite

Figure 6.22 presents typical NC-AFM data after the deposition of ~ 0.4 ML of TMA on a clean $CaCO_3$ surface. In Figure 6.22(a), molecular strands roughly oriented

along the [01.0] substrate direction are observed. The image is crossed by nearly vertically oriented step edges of the underlying calcite substrate. Figure 6.22(b) presents a detailed view at the position indicated in Figure 6.22(a). In this Figure, a total of four phases formed inside the molecular strands coexist. One phase (phase **A**) reveals a nearly hexagonal pattern, while phases $\mathbf{B_1}$ and $\mathbf{B_2}$ represent a stripe-like ordering. The fourth phase, namely phase **C**, appears firsthand unordered, but later data will point to a highly truncated chicken-wire motif. An examplary region of each phase is marked in Figure 6.22(b). The imaged height for all molecular phases is in the order of 2 Å as apparent from the height distribution (see inset Figure 6.22(b)). This finding suggests a flat-lying geometry of TMA molecules for all observed phases, which will now be discussed.

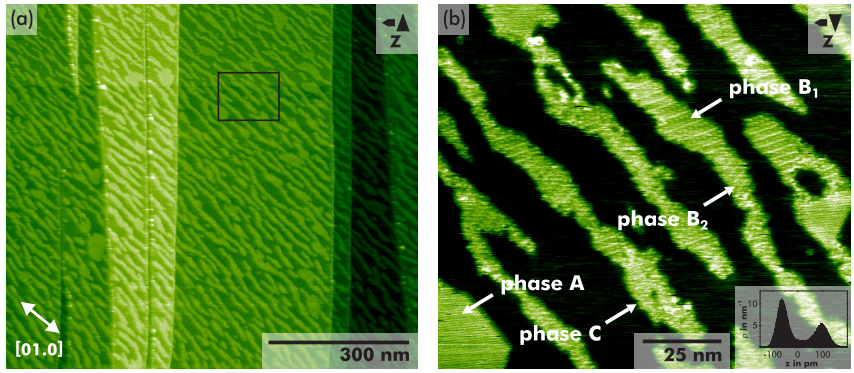

Figure 6.22.: NC-AFM data for the TMA/$CaCO_3$(10.4) sytem. (a) Molecular strands roughly oriented along the [01.0] substrate direction are observed. (b) A total of four phases coexist and are named in this zoom-in.

Phase A The discussion is commenced with phase **A**, the hexagonally appearing domain. Figure 6.23(a) presents a high-resolution Δf image of one island, where both, the molecular structure and the underlying $CaCO_3$(10.4) surface is resolved. The data is carefully corrected for thermal drift using the drift-correction strategy developed by myself and coworkers [160]. Two-dimensional Fourier-transformations (2D-FT) from several consecutive images are utilised to measure the lateral dimensions of the molecular structure. An exemplary 2D-FT is included in Figure 6.23(a), where the spots originating from the molecular structure are marked by green circles and spots from the substrate lattice periodicity are marked by red circles. The former spots yield periodicities of (8.5 ± 0.3)Å, (8.3 ± 0.3)Å and (8.1 ± 0.3)Å for the molecular structure, while the substrate lattice is measured to $(4.8 \pm 0.2) \times (8.4 \pm 0.4)$Å^2, in good agreement with the crystallographic bulk data (see Chapter 5 for details). For a hexagonal lattice, the nearest-

neighbour distance c_i is given by $c_i = \frac{2}{\sqrt{3}} d_i$ from the lattice plane distances d_i. Consequently, for the preceding data an average nearest-neighbour distance of (9.6 ± 0.6)Å is calculated.

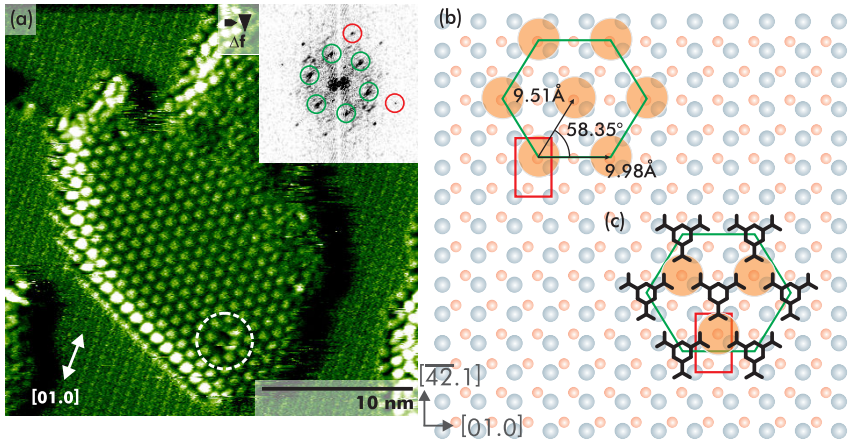

Figure 6.23.: (a) High-resolution Δf image of phase **A**. The island is embedded into an island of phase **C** (see top of the image). In the inset, the 2D-FT of (a) is shown. The molecular adsorption structure shown (b) and (c) is most likely stabilised by hydrogen bonds between the carboxylic groups of three flat-lying TMA molecules. Therefore, this structure is comparable to the flower motif.

This average nearest-neighbour distance is in excellent agreement with a nearly hexagonal superstructure on the $CaCO_3$(10.4) surface, which is visualised in Figure 6.23(b). The TPA data in Section 6.3 already suggested an intense templating effect of the calcite $CaCO_3$(10.4) substrate. Consequently, the substrate lattice is here chosen as the reference for the molecular adsorption model, especially the sublattice of the topmost oxygen atoms is assumed to align with the carboxylic acid groups. These assumption directly suggest the adsorption model for the quasi-hexagonal superstructure in phase **A** as depicted in Figure 6.23(b): The slightly distorted hexagonal cell of the flower motif is a commensurate superstructure, in this Figure aligned with respect to one topmost oxygen atom of the carbonate groups. The unit cell for this structure is a slightly compressed hexagon, precisely the structure bears an oblique unit cell with $a_1 = 9.98$Å, $a_2 = 9.51$Å and $\alpha = 58.35°$. Using Wood's notation, the molecules form a $c(2 \times 2)$ superstructure. In this superstructure, the difference in the nearest neighbour distances amounts to about 5 %. The dimensions are in excellent agreement with the measured distances d_i from the 2D-FT.

In Figure 6.23(c), structural models of TMA molecules are superimposed on the oblique unit cell. The structure is most likely stabilised by hydrogen bonds be-

tween the carboxylic acid groups of three TMA molecules and, thus, corresponds to the close-packed flower motif. The repeating unit is indeed observed in the Δf images and even defects (one marked in the lower right of Figure 6.23(a)) are observed. The absolute adsorption position is only suggested in this Figure, it was not identified unambiguously from the NC-AFM data. This uncertainty is tightened, as it is currently also unclear whether the molecular benzene core or the region of hydrogen bonding is imaged "bright" for the TMA superstructure.

Phases B_1, B_2 and C The other three observed phases, namely the striped phases $\mathbf{B_1}$ and $\mathbf{B_2}$ as well as phase **C**, are most likely truncated subfigures of the chicken-wire motif. The chicken-wire motif is stabilised by hydrogen bonds between carboxylic acid dimers as depicted in Figure 6.24. Most interestingly, an extended chicken-wire motif itself is here not observed on a $CaCO_3$(10.4) surface, which is in contrast to the omnipresence on conducting surfaces [128, 111, 77, 48, 226, 189]. Recalling the assumption of a templating effect due to a strong interaction between the protruding surface oxygen atoms and the molecular carboxylic acid groups, the reason for this absence is presumably the severe mismatch of the chicken-wire superstructure with the $CaCO_3$(10.4) surface lattice as depicted in Figure 6.24. In this figure, the chicken-wire motif is printed with di-

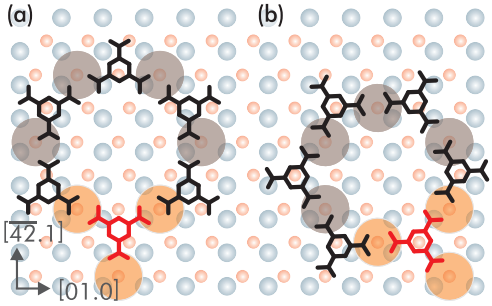

Figure 6.24.: Chicken-wire motif of the TMA molecules superimposed to scale to the $CaCO_3$(10.4) surface. While one molecule can bind to three surface oxygen atoms as suggested from the flower motif, the resulting molecular structure is expected not being congruent to the substrate structure. This is shown for two geometries in (a) and (b).

mensions derived from the bulk structure. A single TMA molecule can adsorb on the $CaCO_3$(10.4) surface with all three carboxyl groups being more or less in registry with the surface lattice, especially being in registry with the topmost surface oxygen atoms (molecule highlighted in red, oxygen atoms highlighted in orange). Upon continuing the chicken-wire structure, however, the registry with the topmost oxygen atoms is usually not conserved and, thus, this adsorption geometry is expected to be energetically unfavourable.

Figure 6.25 represents high-resolution NC-AFM data acquired of phases $\mathbf{B_1}$ and $\mathbf{B_2}$ in Subfigures (a) and (b). Additionally, Subfigure (c) represents high-resolution data of presumably phase **C** apparent within a full monolayer of TMA molecules. For the phase $\mathbf{B_1}$ and $\mathbf{B_2}$, the molecular arrangement is most clearly revealed from

the dissipation data reproduced in Figure 6.25(b). The molecular structure can be described by a centre line (indicated in red in Figure 6.25(a)), to which additional molecules are attached on both sides. As already suggested by the data in Figure 6.22(b), this centre line draws an angle with the $[\overline{4}2.1]$ direction and the two phases $\mathbf{B_1}$ and $\mathbf{B_2}$ hereby differ by the sign of this angle. Precisely, in these data an angle of $\pm(18\pm2)°$ drawn with the $[\overline{4}2.1]$ direction is measured. The existence of these two phases are in agreement with the glide plane symmetry of the $CaCO_3$(10.4) surface (see Section 5.4 for details).

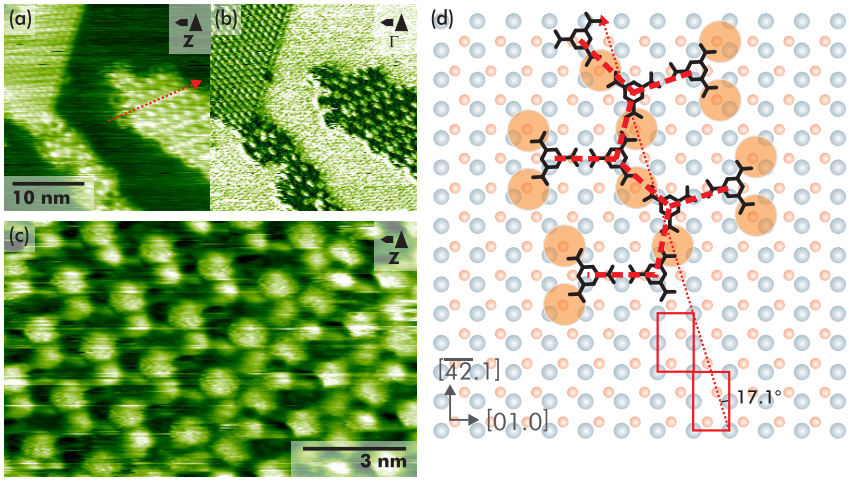

Figure 6.25.: High-resolution NC-AFM images of the phases $\mathbf{B_1}$ and $\mathbf{B_2}$ in (a) and (b). (c) Is presumably phase **C** upon the formation of a full monolayer. All observed motifs suggest a truncated chicken-wire motif, for which a structural model is given in (d).

Figure 6.25(d) presents a structural model suggested by the experimental data. The model is a truncated chicken-wire motif, where the sides of the hexagonal gaps are open. The centre molecule line proceeds here along the $[\overline{8}7.2]$ substrate direction, the $[\overline{8}1.2]$ direction is the symmetric analogon. This direction forms an angle of 17.1° with the $[\overline{4}2.1]$ direction, which is in excellent agreement to the measured value of $(18\pm2)°$.

6.4.3. Varied coverages of TMA

Ye *et al.* [226] investigated the self-assembly of TMA on Au(111) surfaces, where the evolution of the chicken-wire motif to the dense-packed flower structure has been reported to depend on the molecular coverage. To rule out a coverage dependent formation for the TMA/$CaCO_3$(10.4) system, experiments are performed

at varied coverages. Figure 6.26 presents NC-AFM results from samples with different coverages of TMA molecules. The data suggest no coverage dependence on the structure formation. Especially, the dense-packed flower-structure does not evolve when approaching one monolayer coverage. Additional annealing experiments were performed, where the TMA/$CaCO_3$(10.4) samples were heated to a maximum of $\sim 380\,K$, but it was not possible to induce a structure reorganisation (data not shown).

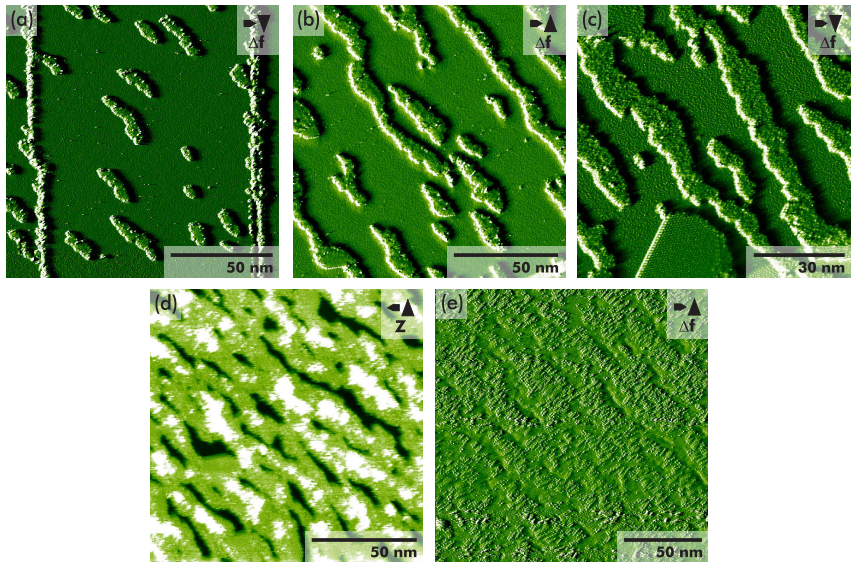

Figure 6.26.: Different coverages of TMA molecules on the $CaCO_3$(10.4) surface. In (d) and (e), already a second monolayer of molecules is adsorbed on top of the first layer.

6.4.4. Conclusions

TMA molecules adsorbed on $CaCO_3$(10.4) surfaces formed overstructures stable at room temperature. A total of four phases were observed within these data, all phases coexist on the $CaCO_3$(10.4) surface. One phase exhibits the well-ordered flower motif in a $c(2\times 2)$ superstructure, which requires a slight compression of this motif. The other phases were identified as truncated chicken-wire structures. An extended chicken-wire network was not found on this surface, most likely due to a severe incommensurability of this chicken-wire motif to the $CaCO_3$(10.4) surface structure. Also after experiments at elevated temperatures and high molecular coverages, the formation of an extended chicken-wire network was not re-

vealed. This finding denotes a surprisingly intense templating of the calcite substrate on the molecular structure formation. Furthermore, the results demonstrate that the $CaCO_3$(10.4) is a promising substrate when aiming at large-scale formation of hydrogen-bonded networks.

6.5. Helicenes

Within this section, I present the formation of uni-directional molecular structures self-assembled from heptahelicene-2-carboxylic acid ([7]HCA). In contrast to most previous results of molecular "wire" formation on insulating surfaces [129, 74, 100, 144], the wire-like structures observed here grow on bare terraces and are of well-defined width. I use racemic [7]HCA molecules (enantiomeric excess of 0 %), an equimolar mixture of (M)-[7]HCA and (P)-[7]HCA differing in helicity as depicted in Figure 6.27(a). The molecules have been kindly provided by [Name removed][9] and the synthesis has recently been published by Rybáček *et al.* [176]. This section mainly contains the results already published in the *Journal of Physical Chemistry C* [162]. Part of the experiments presented within this section were performed by [Name removed] [143] during his diploma thesis supervised by myself. The density-functional theory (DFT) calculations were performed by [Name removed] in a collaboration with the group of [Name removed] [10].

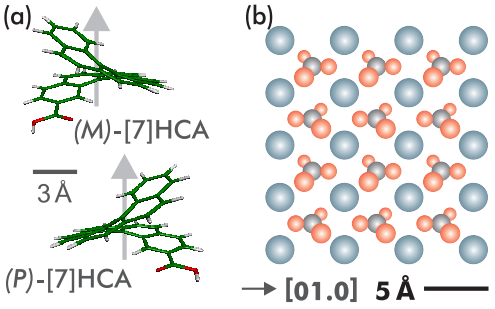

Figure 6.27.: (a) Model of the [7]HCA molecule. The molecule is functionalized by a carboxylic acid group attached to one end of the screw structure. The helical molecular axis is marked by a grey arrow. In this study, the racemic mixture (enantiomeric excess of 0%) of both enantiomers was used. (b) The calcite (10-14) surface

6.5.1. Introduction

In terms of future molecular electronic devices, two elementary structures are pivotal, namely molecular transistors [97] and wires in form of quasi one-dimensional arrangements [129]. For single-molecule transistors, several concepts have already been developed [97], and their switching capability has been demonstrated [206].

Very recently, the first promising results have been obtained on a truly insulating substrate, namely KBr(001) [129, 74, 100, 144]. In these studies, an attempt has been made to form molecular wire-like structures, however, high molecular mobility has led to clustering at the step edges [129, 109] or the formation of structures of several tens of nanometers in width [58]. It has been demonstrated that

[9] Institute of Organic Chemistry and Biochemistry ASCR, Prague, Czech Republik
[10] Fachbereich Physik, Universität Osnabrück, Germany

the length can be controlled by employing Au nanoclusters as end caps, however, both width and height of these molecular structures have remained less well controlled [74, 100].

Within this section, I present the formation of uni-directional molecular structures self-assembled from heptahelicene-2-carboxylic acid ([7]HCA) molecules. The π-system of these molecules provides the potential for electronic transport along several molecules. The transport along single helicene molecules has been studied theoretically [212], demonstrating that by tuning the radius of the helix and the width of the helix ribbon, helicenes exhibit semiconducting or metallic behavior. Bare heptahelicenes ([7]H) without a carboxylic acid moiety have been investigated before on different metal surfaces, namely Cu(111) [54, 56, 57], Cu(332) [56], Ni(100) [55] and Ni(111) [53]. On the Cu surfaces, [7]H molecules bind via the three terminal phenyl rings to the substrate, with its helical axis nearly parallel to the surface normal [56, 57]. On Ni(100), by contrast, [7]H molecules within a saturated monolayer adsorb with their helical axis at an angle of $(43 \pm 5)^\circ$ with respect to the surface plane [55]. This geometry, identified by NEXAFS for Ni(100), is suggested but not confirmed for a closed monolayer on Ni(111) [53].

6.5.2. Results and discussion

The [7]HCA molecules are sublimated onto the bare calcite $CaCO_3$(10.4) surface kept at room temperature from a heated crucible. Figure 6.28 displays an overview image taken approximately 6 h after the molecule deposition. Within this image, single rows located on the calcite surface are clearly visible. All of the rows are aligned along the [01.0] substrate direction. The mean length of the rows in this image is 47 nm with a standard deviation of 24 nm, reflecting the length distribution of the molecular rows as presented in the inset of Figure 6.28. In contrast, the width of the rows is monodisperse and will be discussed later. The distribution of the rows on the surface is random apart from the alignment along the [01.0] direction. At room temperature, straight rows along another crystallographic direction were never observed. Furthermore, neither clustering nor island formation of the molecular rows was observed at this coverage of about one quarter of a full monolayer[11]. Additionally, there is no indication of nucleation at the step edges of the calcite substrate. Two step edges are observed in Figure 6.28 as straight lines running through the entire image from top to bottom. As can be seen, the edges do not constitute nucleation sites for the growth of molecular rows.

The molecular rows shown here form at room temperature and do not require further treatment such as annealing at elevated temperatures. In the early stages of row formation, however, a transient row structure is observed, having a smaller

[11] At coverages of 1 ML, a closed film exhibiting a (2×3) superstructure is observed. In each supercell, two [7]HCA molecules are present and, consequently, one molecule occupies an area of 1.215 nm^2 on the calcite surface.

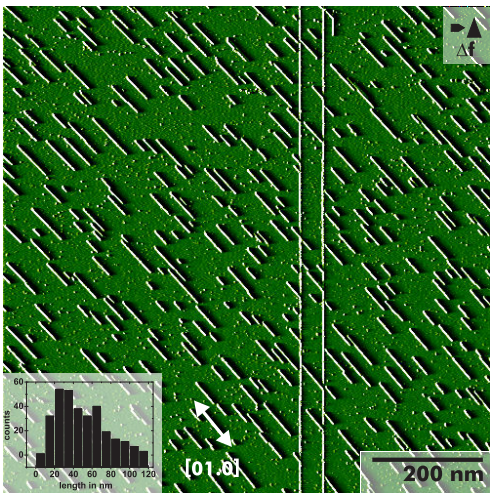

Figure 6.28.: Frequency shift Δf image of the calcite $CaCO_3(10.4)$ surface including the adsorbed molecules taken approximately 6 h after finishing the molecule deposition. Two step edges of the underlying substrate are visible as vertical, straight lines. Unidirectional molecular rows are observed along the [01.0] direction. The length distribution of these rows is presented in the inset.

width than the final molecular rows. Such transient rows can be seen in Figure 6.29, taken ~ 65 min after molecule sublimation. In this image, two different molecular row structures coexist, namely the molecular rows as identified in Figure 6.28 and, additionally, thinner rows which have approximately half of the previously observed width (a few of these thinner rows are marked by arrows). This observation together with the distances identified later indicate that the final molecular row structures are composed of molecular pairs.

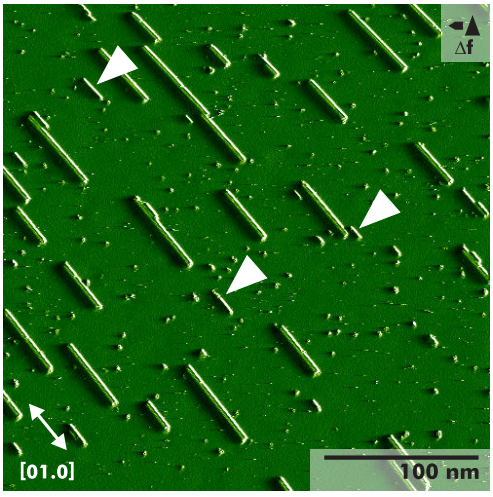

Figure 6.29.: Detailed view of the unidirectional molecular structures. In contrast to Figure 6.28, this image was started ~ 65 min after the molecule deposition was finished. Distinct rows of two different widths are present; the broader rows resemble the rows observed in Figure 6.28. Several thinner rows are marked by white arrows.

The formation of the unidirectional structures demonstrates that the mobility of the molecules at room temperature is sufficient to overcome the diffusion barrier on the surface. On the other hand, the intermolecular interaction strength is large enough to provide stable growth along the molecular row direction. When depositing the [7]HCA molecules onto the calcite substrate held at low temperatures (110 K), individual molecules are observed on the surface (not shown here), indicating that the molecules do not possess sufficient energy to overcome the diffusion barrier at 110 K. This allows for an estimation of a surface diffusion barrier in the range of $0.3\,\text{eV} < E_\text{d} < 0.7\,\text{eV}$, using the estimation presented in the Appendix Section E. Thus, the observed molecular rows represent a self-assembled structure [220] with the $CaCO_3$(10.4) surface acting as a template, as all of the rows align along the [01.0] direction, exclusively.

In order to gain insights into the mechanism of molecular row formation, high-resolution NC-AFM imaging is performed, which reveals details of the molecular structure. Figure 6.30 presents a high-resolution image of one individual molecular row. In Figure 6.30(a), the topography channel is shown, while Figure 6.30(b) represents the corresponding Δf signal. In both channels, an internal structure is clearly resolved. The double-row structure visible in the topography channel (Figure 6.30(a)) is formed by pairs of bright features. This is in good agreement with the above assumption; the final molecular rows are composed of molecular pairs. The protrusions within a pair are separated by (11 ± 3) Å, almost perpendicular to the row direction. The periodicity along the row direction can be determined very precisely, as the underlying calcite substrate structure is resolved simultaneously. In Figure 6.30(b), several parallel white lines indicate the double unit cell repeat distance of $2 \times 5\,\text{Å}^2$ in the [01.0] direction, and therefore the periodicity along the double-row structure can unambiguously be identified to 10 Å.

Imaging highly protruding structures with NC-AFM involves numerous problems, including imaging the tip apex [150], feedback instabilities and entering into the repulsive regime [161]. In Figure 6.30(c) and (d), line profiles taken from the topography (in (c)) and the Δf images (in (d)) are presented, one taken along the molecular row (red) and one perpendicular to the row (black). The same image point is indicated by arrows in all of the subfigures. The corrugation along the molecular row is in the order of 1 Å, whereas the imaged height of the row itself is about ~ 7 Å with respect to the imaged surface. This height of 7 Å is somewhat smaller than what is expected for an upright standing molecule (about 11.5 Å when taking the van-der-Waals radii of an individual molecule), indicating that the upright standing molecules might form a tilt angle with respect to the surface normal. This behavior has been observed previously for heptahelicenes on Ni(100) [55], where the helical axis draws an angle of $(43 \pm 5)^\circ$ with the surface plane. I want, however, stress explicitly that the measured height represents a plane of identical strength of interaction, namely a plane of equal detuning. Thus, it does not necessarily coincide with the expected height derived from quantum

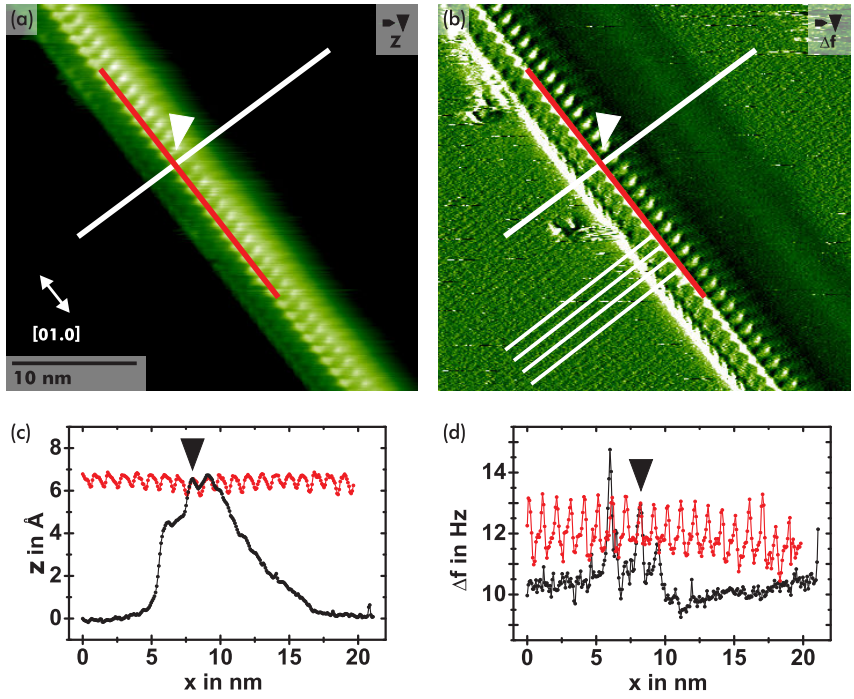

Figure 6.30.: Structure of a paired molecular row as imaged with the NC-AFM in (a) the topography channel and (b) the Δf channel. The same image point is marked in all Figures by white and black arrows. (c) Height profiles taken along the indicated lines of (a). (d) Height profiles taken along the indicated lines in (b).

chemical modeling.

Additionally, the appearance of the molecular row is asymmetric, as seen by the black curve in Figure 6.30(c). This asymmetry holds for both the forward and the backward scan lines (not shown). As the molecular structure protrudes from the surface at least by 7Å compared to the corrugation of the calcite substrate, many atoms of the tip apex interact with the molecular row. Even for a relatively sharp tip, atoms that are several Ångströms away from the foremost tip atom can, thus, contribute to the measured interaction forces, resulting in the asymmetric appearance which reflects the asymmetry of the tip apex. The double-row appearance of the molecular structure does, however, represent the true molecular structure. A careful comparison of data taken with a large number of different tips confirm this point and explicitly exclude the possibility of a double-tip artifact.

The [7]HCA used in this study consists of a racemic mixture of both (M) and (P) enantiomers, which are displayed as ball-and-stick models in Figure 6.27(a).

The NC-AFM results indicate an upright standing geometry of the molecules with the helical axis roughly parallel to the [01.0] direction, but the molecules might be tilted with respect to the surface plane. This interpretation is in agreement with previous results for heptahelicene on Ni(100) [55]. Furthermore, two-dimensional islands might be expected in the case of flat-lying [7]HCA(with the helical axis perpendicular to the surface plane as observed for heptahelicene on Cu(111) [56, 57] rather than the unidirectional rows of [7]HCA described here. The upright geometry allows for $\pi-\pi$ stacking of the molecules along the molecular row direction. Moreover, as a transition of less stable single rows to molecular double rows is observed, the molecules within the $\pi-\pi$ stacked row seem to interact with another neighboring row. Considering the molecular structure, it can be readily assumed that the double-row formation is due to the hydrogen bond formation between the carboxylic acid groups of neighboring [7]HCA molecules. Possible structural models for such rows composed of molecular pairs are given in Figure 6.31(a) to (c). Owing to molecular chirality, two different kinds of molecular rows can be envisioned, namely homochiral (M),(M) and (P),(P) rows, comprising either (M) or (P) enantiomers exclusively, or heterochiral (M),(P) rows, containing both enantiomers within the double row. In the NC-AFM images, no differences were observed between the rows, suggesting that heterochiral rows are formed. However, based on the NC-AFM images alone, it is not possible to identify the internal structure clearly, leaving the possibility that existing differences in the case of homochiral double-row formation remain undiscovered, although many high-resolution data of different molecular rows were carefully compared. In order to obtain basic insights into the organization of [7]HCA on the calcite surface leading to the row formation, A. Greuling[12] performed density functional theory (DFT) calculations for this system. Technical details given in Ref. [162]. As the large size of the surface system with the molecules on top constitutes a challenging task for DFT, several simplifications are employed. All the calculations are performed with the [7]HCA molecules in-vacuo, thus in the absence of the calcite surface.

In the first step, the geometry of an individual molecule was optimised by minimising all the forces to less than 0.01 eV/Å. Secondly, the interaction potential of two such relaxed molecules is calculated in dependence on the molecule-molecule distance, as shown in Figure 6.31(d). Based on this calculation, a binding energy of about 0.09 eV at an optimum distance of 8 Å is obtained for a single row. Furthermore, the distance-dependent potential for a homo- and a heterochiral molecular double row as shown in Figure 6.31(b) and (c) is calculated. For this calculation, initially the geometry of a molecular pair consisting of two molecules (either homo- or heterochiral) forming hydrogen bonds between the carboxylic groups was optimised. After obtaining this optimised pair geometry, the distance-

[12] Fachbereich Physik, Universität Osnabrück, Osnabrück, Germany

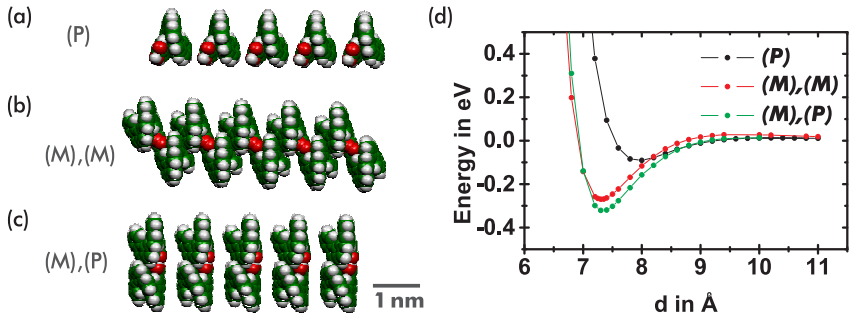

Figure 6.31.: Models for different [7]HCA rows. (a) Single homochiral molecular row. (b) Homochiral molecular double row formed by homochiral molecular pairs. (c) Heterochiral molecular double row formed by heterochiral molecular pairs. (d) Calculated potentials for the above shown different row geometries. (black) Interaction potential of two individual [7]HCA molecules, i.e. forming a single row as shown in (a) (same for (M)). (red) Interaction potential of two homochiral pairs, forming a homochiral double row as shown in (b) (same for (P),(P)). (green) Interaction potential of two heterochiral pairs, forming a heterochiral double row as shown in (c). Note that another arrangement for the heterochiral rows does in principle exist, comprising of homochiral pairs of different chirality. This configuration, however, hampers $\pi-\pi$ stacking and was, thus, omitted in this calculation.

dependent potential was calculated by varying the pair-pair distance of two pairs (without further relaxation of the individual pairs). As can be seen, the binding energy is about 0.27 eV per pair for the homochiral double row at an optimum distance of 7.3 Å. For the heterochiral pair, a binding energy of about 0.32 eV at a distance of about 7.3 Å was obtained.

The energy difference between the homo- and heterochiral pairs calculated here is too small to be taken literally. This is especially true when considering the simplification made by omitting the substrate surface. Furthermore, DFT calculations do not describe systematically the dispersion forces contributing to the $\pi-\pi$ interactions [78, 79, 214, 173, 187]. Fortunately, the local-density approximation (LDA) to the DFT exchange-correlation functional often yields binding energies and distances of weakly interacting objects in reasonable agreement with more elaborate approaches and with experiments [130, 83, 171] Therefore, the calculated data do strongly support the above-drawn conclusion of upright standing molecules forming rows by $\pi-\pi$ stacking of the aromatic rings. Moreover, the calculations indicate that single molecular rows with a binding energy of only 0.09 eV remain unstable at room temperature, while the formation of heterochiral, molecular double-rows with a binding energy of 0.32 eV seems plausible. This calculated binding energy is relatively small; however, absolute energy values are

calculated with rather large error for the reasons discussed above.

Finally, the binding distances obtained from DFT suggest an optimum distance of about 7.3 Å somewhat smaller than the observed periodicity of 10 Å. This difference can be understood by considering a possible tilted alignment of the molecules. Upon tilting the main molecular axis about 43° with respect to the surface plane, the intermolecular distance measured parallel to the helical axes is decreased from initially 10 Å to 7.3 Å. At the same time, the height of the molecule is reduced from approximately 11.5 Å to 8.4 Å, which is rather close to the experimentally observed molecular height.

6.5.3. Conclusions

In conclusion, this section presented the self-assembly of uni-directional molecular structures of racemic [7]HCA molecules on the calcite $CaCO_3$(10.4) surface. The molecular rows do not require nucleation sites such as step edges but form on the bare terraces. High-resolution NC-AFM images revealed insights into the molecular geometry, indicating molecular rows formed by upright-standing pairs of [7]HCA molecules with their helical axis tilted with respect to the surface plane. This configuration was readily understood by $\pi - \pi$ stacking of the molecules within a row and hydrogen bond formation to the neighboring rows. Ab-initio calculations elucidated the detailed geometry and support the assumption of tilted molecules. This study demonstrates that choosing properly functionalized molecules enables self-assembly of molecular wire-like structures even on insulating surfaces, where high molecular mobility has so far hampered the self-assembly of tailor-made molecular structures.

7. Summary

In conclusion, this thesis presents a detailed and successful study of molecular self-assembly on the calcite $CaCO_3(10.4)$ surface. One reason for the superior applicability of this particular surface was given in Chapter 2, where the well-known growth modes were reflected. Layer-by-layer growth, which is a necessity for the formation of templated 2D molecular structures, is particularly favoured on substrates with a high surface energy. The $CaCO_3(10.4)$ surface is among those substrates and, thus, most promising.

All experiments in this thesis were performed using the NC-AFM technique under ultra-high vacuum conditions. The acquisition of drift-free data, a necessity since the very beginning in the SPM field, became in this thesis possible owing to the herein newly developed atom-tracking system. The performance analysis of this system in Chapter 4 revealed a most robust operation under large and non-linear drift conditions. A lateral tip-positioning precision of at least 50 pm was achieved. Furthermore, a newly developed scan protocol was implemented in this system, which allows for the acquisition of dense 3D data under room-temperature conditions. An entire 3D data set from a $CaCO_3(10.4)$ surface consisting of $85 \times 85 \times 500$ pixel was discussed. This data set constitutes the current pixel record for 3D NC-AFM data acquired under room-temperature conditions.

The row-pairing and (2×1) reconstructions of the $CaCO_3(10.4)$ surface constitute most interesting research subjects from a fundamental and application-oriented point of view. For both reconstructions, the NC-AFM imaging was classified to a total of 12 contrast modes. Eight of these modes were observed within this thesis, some of them for the first time. Together with literature findings, a total of 10 modes has been observed experimentally to this day. Some contrast modes presented themselves as highly distance-dependent and at least for one contrast mode, a severe tip-termination influence was found. The analysis demonstrated the difficulties in interpreting NC-AFM data of the $CaCO_3(10.4)$ surface, especially when recorded in constant-force (constant-Δf) mode. Moreover, many results obtained within this thesis require close interplay with theory, especially by means of *ab-initio* methods. The herein discussed experimental data is expected to constitute a most valuable input for future theoretical investigations.

Most interestingly, the row-pairing reconstruction was found to break a symmetry element of the $CaCO_3(10.4)$ surface. With the presence of this reconstruc-

tion, the calcite (10.4) surface becomes chiral. This finding is inconsistent with the current literature understanding, where the surface is, in agreement with the bulk-truncated structure, accounted to be achiral. Although the row-pairing reconstruction itself has been observed before in contact AFM experiments, the physical origin for this reconstruction is still unclear. From high-resolution NC-AFM data, the identification of the enantiomers is here possible and was presented for one enantiomer in this thesis.

Chapter 6 presented five studies of self-assembled molecular structures on calcite $CaCO_3$(10.4) surfaces. Only for one system, namely HBC/$CaCO_3$(10.4), the formation of a bulk structure was observed. This well-known occurence of weak molecule-insulator interaction hinders the investigation of two-dimensional molecular self-assembly. It was, however, possible to force the formation of an island phase for this system upon following a variable-temperature preparation.

For the C_{60}/$CaCO_3$(10.4) system it is most notably that no branched island morphologies were found. Instead, the first C_{60} layer appeared to wet the calcite surface. This finding is in full agreement with the analysis in Chapter 2, but, to my best knowledge, for insulators exclusively observed here so far.

In all studies, the molecules arranged themselves in ordered superstructures. A templating effect due to the underlying calcite substrate was evident for all systems. This templating strikingly led either to the formation of large commensurate superstructures, such as a (2×15) structure with a 14 molecule basis for the C_{60}/$CaCO_3$(10.4) system, or prevented the vast growth of incommensurate molecular motifs, such as the chicken-wire structure in the TMA/$CaCO_3$(10.4) system.

The molecule-molecule and the molecule-substrate interaction was increased upon choosing molecules with carboxylic acid moieties in the third, fourth and fifth study. In all experiments, hydrogen-bonded assemblies were created. TPA molecules arrange flat-lying in a well-ordered (2×2) superstructure, but at room temperature still attachment and detachment of single molecules from the molecular islands was observed at a considerable rate. TMA presented at least four different phases, coexisting on the surface. One phase is the well-known flower structure, which yielded in contrast to the TPA molecules stable islands at submonolayer coverages.

Directed hydrogen bond formation combined with intermolecular $\pi - \pi$ interaction is employed in the fifth study, where the formation of uni-directional molecular "wires" from single helicene molecules succeeded. Each "wire" is composed of heterochiral helicene pairs, well-aligned along the [01.0] substrate direction and stabilised by $\pi - \pi$ interaction. Most notably, the directed hydrogen bond formation enforce a limitation of the molecular row width to two molecules.

These experimental findings lead to the following conclusions for molecular self-assembly on $CaCO_3$(10.4): (i) planar hydrocarbon molecules are presumably an unfortunate choice, as HBC dewetted from the surface and was highly mo-

bile. (ii) The calcite $CaCO_3$(10.4) surface had an intense templating effect on the molecular structure formation. (iii) The molecular superstructure had to be commensurate to the calcite substrate lattice, otherwise templated molecular structure formation was unfavoured. (iv) The inclusion of carboxylic acid moieties led to the formation of hydrogen-bonded networks as long as conclusion (iii) was fulfilled.

All investigated systems clearly demonstrate that a rational choice of both, a high surface-energy substrate and properly functionalised molecules allows for molecular self-assembly on an insulator with a structural variety that has so far only been achieved on metallic and semiconducting substrates. Especially the successful formation of uni-directional molecular rows of well-defined width demonstrates the potential for extending complex molecular structure formation from conducting to insulating surfaces.

Bibliography

[1] **Abe, M., Sugimoto, Y., Custance, Ó., Morita, S.** Atom tracking for reproducible force spectroscopy at room temperature with non-contact atomic force microscopy. *Nanotechnology* 16 (2005), 12, p. 3029

[2] **Abe, M., Sugimoto, Y., Custance, Ó., Morita, S.** Room-temperature reproducible spatial force spectroscopy using atom-tracking technique. *Applied Physics Letters* 87 (2005), 17, p. 173503

[3] **Abe, M., Sugimoto, Y., Namikawa, T., Morita, K., Oyabu, N., Morita, S.** Drift-compensated data acquisition performed at room temperature with frequency modulation atomic force microscopy. *Applied Physics Letters* 90 (2007), 20, p. 203103

[4] **Addadi, L., Weiner, S.** Control and design principles in biological mineralization. *Angewandte Chemie-International Edition* 31 (1992), 2, p. 153–169

[5] **Addadi, L., Weiner, S.** Crystals, asymmetry and life. *Nature* 411 (2001), p. 753

[6] **Albers, B. J., Schwendemann, T. C., Baykara, M. Z., Pilet, N., Liebmann, M., Altman, E. I., Schwarz, U. D.** Data acquisition and analysis procedures for high-resolution atomic force microscopy in three dimensions. *Nanotechnology* 20 (2009), 26, p. 264002

[7] **Albers, B. J., Schwendemann, T. C., Baykara, M. Z., Pilet, N., Liebmann, M., Altman, E. I., Schwarz, U. D.** Three-dimensional imaging of short-range chemical forces with picometre resolution. *Nature Nanotechnology* 4 (2009), 5, p. 307

[8] **Albrecht, T. R., Grütter, P., Horne, D., Rugar, D.** Frequency-Modulation Detection Using High-Q Cantilevers for Enhanced Force Microscope Sensitivity. *Journal of Applied Physics* 69 (1991), 2, p. 668

[9] **Analog Devices**: *Quad-Channel Digital Isolators ADuM1400 / ADuM1401 / ADuM1402 (Rev. G)*, 2008

[10] **Arduino**: *Arduino Open Source Project*. http://www.arduino.cc

[11] **Ashino, M., Obergfell, D., Haluska, M., Yang, S. H., Khlobystov, A. N., Roth, S., Wiesendanger, R.** Atomic-resolution three-dimensional force and damping maps of carbon nanotube peapods. *Nanotechnology* 20 (2009), 26, p. 264001

[12] **Atmel**: *8-bit AVR Microcontroller, Rev 2549L-08/07*, 08 2007

[13] **Baer, D.R., Jr., D. L. B.** Studies of the calcite cleavage surface for comparison with calculation. *Applied Surface Science* 72 (1993), 4, p. 295

[14] **Bailey, M., Brown, C. J.** The crystal structure of terephthalic acid. *Acta Crystallographica* 22 (1967), 3, p. 387

[15] **Barth, C.**: *Atomar aufgelöste Kraftmikroskopie auf ionischen Oberflächen: Fluoride, Calcit und Saphir*. Leipzig, Universität Osnabrück, Diss., 2002

[16] **Barth, C., Foster, A. S., Henry, C. R., Shluger, A. L.** Recent Trends in Surface Characterization and Chemistry with High-Resolution Scanning Force Methods. *Advanced Materials* 23 (2011), 4, p. 477

[17] **Barth, C., Henry, C. R.** Kelvin probe force microscopy on surfaces of UHV cleaved ionic crystals. *Nanotechnology* 17 (2006), 7, p. 155

[18] **Barth, J. V.** Molecular architectonic on metal surfaces. *Annual Review of Physical Chemistry* 58 (2007), p. 375

[19] **Barth, J. V., Costantini, G., Kern, K.** Engineering atomic and molecular nanostructures at surfaces. *Nature* 437 (2005), 7059, p. 671

[20] **Barth, J. V., Weckesser, J., Cai, C., Günter, P., Bürgi, L., Jeandupeux, O., Kern, K.** Building supramolecular nanostructures at surfaces by hydrogen bonding. *Angewandte Chemie, International Edition* 39 (2000), 7, p. 1230

[21] **Barth, J. V., Weckesser, J., Lin, N., Dmitriev, A., Kern, K.** Supramolecular architectures and nanostructures at metal surfaces. *Applied Physics A: Materials Science & Processing* 76 (2003), 5, p. 645

[22] **Bauer, E.** Phänomenologische Theorie der Kristallabscheidung an Oberflächen. I. *Zeitschrift für Kristallographie* 110 (1958), 1-6, p. 372

[23] **Baykara, M. Z., Schwendemann, T. C., Altman, E. I., Schwarz, U. D.** 3D Atomic Force Microscopy: Three-Dimensional Atomic Force Microscopy - Taking Surface Imaging to the Next Level. *Advanced Materials* 22 (2010), 26, p. 2838

[24] **Bechstein, R.**: *Pristine and Doped Titanium Dioxide Studied by NC-AFM*, Universität Osnabrück, Diss., 2009

[25] **Bennett, J.M., Bennett, J.E.**: *Handbook of Optics.* New York : McGraw-Hill, 1978

[26] **Benson, G. C., Claxton, T. A.** Application of a shell model to calculation of surface distortion in alkali halide crystals. *Journal of Chemical Physics* 48 (1968), 3, p. 1356

[27] **Binnig, G., Quate, C.F., Gerber, C.** Atomic Force Microscope. *Physical Review Letters* 56 (1986), 9, p. 930

[28] **Binnig, G., Rohrer, H., Gerber, C., Weibel, E.** Surface studies by scanning tunneling microscopy. *Physical Review Letters* 49 (1982), 1, p. 57

[29] **Binnig, G., Rohrer, H., Gerber, C., Weibel, E.** 7x7 Reconstruction on silicon(111) resolved in real space. *Physical Review Letters* 50 (1983), 2, p. 120

[30] **Bragg, W. L.** The Structure of Some Crystals as Indicated by Their Diffraction of X-rays. *Proceedings of the Royal Society of London. Series A* 89 (1913), 610, 248

[31] **Bragg, W. L.** The Analysis of Crystals by the X-ray Spectrometer. *Proceedings of the Royal Society of London. Series A* 89 (1914), 613, 468

[32] **Braun, D. A., Langewisch, G., Fuchs, H., Schirmeisen, A.** Force field experiments of an epitaxial superstructure of 3,4,9,10-perylenetetra-carboxylic-dianhydride on Ag(111). *Journal of Vacuum Science & Technology B* 28 (2010), 3, p. C4B6

[33] **Braun, D. A., Weiner, D., Such, B., Fuchs, H., Schirmeisen, A.** Submolecular features of epitaxially grown PTCDA on Cu(111) analyzed by force field spectroscopy. *Nanotechnology* 20 (2009), 26, p. 264004

[34] **Burke, S. A., Mativetsky, J. M., Fostner, S., Grütter, P.** C_{60} on alkali halides: Epitaxy and morphology studied by noncontact AFM. *Physical Review B* 76 (2007), 3, p. 035419

[35] **Burke, S. A., Topple, J. M., Gruetter, P.** Molecular dewetting on insulators. *Journal of Physics: Condensed Matter* 21 (2009), 42, p. 423101

[36] **Burr-Brown Corporation**: *FET-Input, Low Distortion Operational Amplifier*, 1992

[37] **Burr-Brown Corporation**: *16-Bit Digital-to-analog converter with 16-Bit Bus Interface*, 1994

[38] **Butt, H.-J., Cappella, B., Kappl, M.** Force measurements with the atomic force microscope: Technique, interpretation and applications. *Surface Science Reports* 59 (2005), 1, p. 1

[39] **Cañas-Ventura, M. E., Klappenberger, F., Clair, S., Pons, S., Kern, K., Brune, H., Strunskus, T., Wöll, C., Fasel, R., Barth, J. V.** Coexistence of one- and two-dimensional supramolecular assemblies of terephthalic acid on Pd(111) due to self-limiting deprotonation. *Journal of Chemical Physics* 125 (2006), 18, p. 184710

[40] **Chou, S. Y., Krauss, P. R., Renstrom, P. J.** Nanoimprint lithography. *Journal of Vacuum Science & Technology B* 14 (1996), 6, p. 4129

[41] **Cirrus Logic**: *PA15FL, PA15FLA High Voltage Power Operational Amplifiers*, 2010

[42] **Clair, S., Pons, S., Seitsonen, A. P., Brune, H., Kern, K., Barth, J. V.** STM Study of Terephthalic Acid Self-Assembly on Au(111): Hydrogen-Bonded Sheets on an Inhomogeneous Substrate. *Journal of Physical Chemistry B* 108 (2004), 38, p. 14585

[43] **Cölfen, H.** Precipitation of carbonates: recent progress in controlled production of complex shapes. *Current Opinion in Colloid & Interface Science* 8 (2003), 1, p. 23

[44] **Craats, A. M. d., Warman, J. M., Fechtenkotter, A., Brand, J. D., Harbison, M. A., Mullen, K.** Record charge carrier mobility in a room-temperature discotic liquid-crystalline derivative of hexabenzocoronene. *Advanced Materials* 11 (1999), 17, p. 1469

[45] **Deer, W. A., Howie, R. A., Zussman, J.**: *An introduction to the rock forming minerals*. Pearson Education Limited, 1992

[46] **Diebold, U.** The surface science of titanium dioxide. *Surface Science Reports* 48 (2003), 5-8, p. 53

[47] **Dienel, T., Loppacher, C., Mannsfeld, S. C. B., Forker, R., Fritz, T.** Growth-mode-induced narrowing of optical spectra of an organic adlayer. *Advanced Materials* 20 (2008), 5, p. 959

[48] **Dmitriev, A., Lin, N., Weckesser, J., Barth, J. V., Kern, K.** Supramolecular Assemblies of Trimesic Acid on a Cu(100) Surface. *Journal of Physical Chemistry B* 106 (2002), 27, p. 6907

[49] **Duchamp, D. J., Marsh, R. E.** Crystal Structure of Trimesic Acid (Benzene-1,3,5-Tricarboxylic Acid). *Acta Crystallographica Section B-Structural Crystallography and Crystal Chemistry* 25 (1969), p. 5

[50] **Duffy, D. M., Harding, J. H.** Modelling the interfaces between calcite crystals and Langmuir monolayers. *Journal of Materials Chemistry* 12 (2002), p. 3419

[51] **Effenberger, H., Mereiter, K., Zemann, J.** Crystal-structure refinements of magnesite, calcite, rhodochrosite, siderite, smithonite, and dolomite, with discussion of some aspects of the stereochemistry of calcite type carbonates. *Zeitschrift Fur Kristallographie* 156 (1981), 3-4, p. 233

[52] **Eigler, D.M., Schweizer, E.K.** Positioning Single Atoms with a Scanning Tunneling Microscope. *Nature* 344 (1990), p. 524

[53] **Ernst, K.-H., Böhringer, M., McFadden, C. F., Hug, P., Müller, U., Ellerbeck, U.** Nanostructured chiral surfaces. *Nanotechnology* 10 (1999), p. 355

[54] **Ernst, K. H., Kuster, Y., Fasel, R., Muller, M., Ellerbeck, U.** Two-dimensional separation of [7]helicene enantiomers on Cu(111). *Chirality* 13 (2001), 10, p. 675

[55] **Ernst, K. H., Neuber, M., Grunze, M., Ellerbeck, U.** NEXAFS study on the orientation of chiral P-heptahelicene on Ni(100). *Journal of the American Chemical Society* 123 (2001), 3, p. 493

[56] **Fasel, R., Cossy, A., Ernst, K. H., Baumberger, F., Greber, T., Osterwalder, J.** Orientation of chiral heptahelicene $C_{30}H_{18}$ on copper surfaces: An x-ray photoelectron diffraction study. *Journal of Chemical Physics* 115 (2001), 2, p. 1020

[57] **Fasel, R., Parschau, M., Ernst, K.-H.** Amplification of chirality in two-dimensional enantiomorphous lattices. *Nature* 439 (2006), 7075, p. 449

[58] **Fendrich, M., Kunstmann, T.** Organic molecular nanowires: N,N'-dimethylperylene-3,4,9,10-bis(dicarboximide) on KBr(001). *Applied Physics Letters* 91 (2007), 2, p. 023101

[59] **Feng-Ling, L.** The Morse's Type Potential Function for C_{60}-C_{60} Interactions and Its Applications. *Acta Physico-Chimica Sinica* 18 (2002), p. 967

[60] **Feynman, R. P.** There's Plenty of Room at the Bottom. *Caltech Engineering and Science* 23 (1960), p. 22

[61] **Foster, A., Shluger, A., Barth, C., Reichling, M.**: Contrast mechanisms on insulating surfaces. In: **Morita**, S. (Hrsg.), **Wiesendanger**, R. (Hrsg.), **Meyer**, E. (Hrsg.): *Noncontact Atomic Force Microscopy*. Berlin : Springer, 2002, p. 305

[62] **Foster, A. S., Gal, A. Y., Nieminen, R. M., Shluger, A. L.** Probing Organic Layers on the TiO_2(110) Surface. *Journal of Physical Chemistry B* 109 (2005), 10, p. 4554

[63] **Foster, A. S., Shluger, A. L., Nieminen, R. M.** Quantitative modelling in scanning force microscopy on insulators. *Applied Surface Science* 188 (2002), 3-4, p. 306

[64] **Fukuma, T., Ueda, Y., Yoshioka, S., Asakawa, H.** Atomic-Scale Distribution of Water Molecules at the Mica-Water Interface Visualized by Three-Dimensional Scanning Force Microscopy. *Physical Review Letters* 104 (2010), 1, p. 016101

[65] **Gale, J.**: *priv. comm.* 2010

[66] **Giessibl, F. J.** Atomic resolution of the silicon (111)-(7x7) surface by atomic force microscopy. *Science* 267 (1995), 5194, p. 68

[67] **Giessibl, F. J.** Forces and frequency shifts in atomic-resolution dynamic-force microscopy. *Physical Review B* 56 (1997), 24, p. 16010

[68] **Giessibl, F. J.** Advances in atomic force microscopy. *Reviews of Modern Physics* 75 (2003), 3, p. 949

[69] **Giessibl, F. J., Bielefeldt, H.** Physical interpretation of frequency-modulation atomic force microscopy. *Physical Review B* 61 (2000), 15, p. 9968

[70] **Gifford, J. W.** The Refractive Indices of Fluorite, Quartz, and Calcit. *Proceedings of the Royal Society of London* 70 (1902), p. 329

[71] **Gilman, J. J.** Direct measurements of the surface energies of crystals. *Journal of Applied Physics* 31 (1960), 12, p. 2208

[72] **Girifalco, L. A.** Molecular-Properties of C_{60} in the Gas and Solid-Phases. *Journal of Physical Chemistry* 96 (1992), 2, p. 858

[73] **Glatzel, T., Zimmerli, L., Kawai, S., Meyer, E., Fendt, L.-A., Diederich, F.** Oriented growth of porphyrin-based molecular wires on ionic crystals analysed by nc-AFM. *Beilstein Journal of Nanotechnology* 2 (2011), p. 34

[74] **Glatzel, T., Zimmerli, L., Koch, S., Kawai, S., Meyer, E.** Molecular assemblies grown between metallic contacts on insulating surfaces. *Applied Physics Letters* 94 (2009), 6, p. 063303

[75] **Glowatzki, H., Gavrila, G. N., Seifert, S., Johnson, R. L., Räder, J., Müllen, K., Zahn, D. R. T., Rabe, J. P., Koch, N.** Hexa-peri-hexabenzocoronene on Ag(111): Monolayer/multilayer transition of molecular orientation and electronic structure. *Journal of Physical Chemistry C* 112 (2008), 5, p. 1570

[76] **Goddard, R., Haenel, M. W., Herndon, W. C., Kruger, C., Zander, M.** Crystallization of large planar polycyclic aromatic-hydrocarbons - the molecular and crystal-structures of hexabenzo[bc,ef,hi,kl,no,qr]coronene and benzo[l,2,3-bc/4,5,6-b'c']dicoronene. *Journal of the American Chemical Society* 117 (1995), 1, p. 30

[77] **Griessl, S., Lackinger, M., Edelwirth, M., Hietschold, M., Heckl, W. M.** Self-assembled two-dimensional molecular host-guest architectures from trimesic acid. *Single Molecules* 3 (2002), 1, p. 25

[78] **Grimme, S.** Accurate description of van der Waals complexes by density functional theory including empirical corrections. *Journal of Computational Chemistry* 25 (2004), 12, p. 1463

[79] **Grimme, S.** Semiempirical GGA-type density functional constructed with a long-range dispersion correction. *Journal of Computational Chemistry* 27 (2006), 15, p. 1787

[80] **Gross, L., Mohn, F., Moll, N., Liljeroth, P., Meyer, G.** The Chemical Structure of a Molecule Resolved by Atomic Force Microscopy. *Science* 325 (2009), 5944, p. 1110

[81] **Gross, L., Mohn, F., Moll, N., Meyer, G., Ebel, R., Abdel-Mageed, W. M., Jaspars, M.** Organic structure determination using atomic-resolution scanning probe microscopy. *Nature Chemistry* 2 (2010), 10, p. 821

[82] **Hadicke, E., Rieger, J., Rau, I. U., Boeckh, D.** Molecular dynamics simulations of the incrustation inhibition by polymeric additives. *Physical Chemistry Chemical Physics* 1 (1999), 17, p. 3891

[83] **Harl, J., Kresse, G.** Cohesive energy curves for noble gas solids calculated by adiabatic connection fluctuation-dissipation theory. *Physical Review B* 77 (2008), 4, p. 045136

[84] **Hazen, R. M.** ; **Palyi**, G. (Hrsg.), **Zucchi**, C. (Hrsg.), **Caglioti**, L. (Hrsg.): *Chiral crystal faces of common rock-forming minerals*. New York: Elsevier, 2004. – 137 S.

[85] **Hazen, R. M., Filley, T. R., Goodfriend, G. A.** Selective adsorption of L- and D-amino acids on calcite: Implications for biochemical homochirality. *Proceedings of the National Academy of Sciences* 98 (2001), 10, p. 5487

[86] **Heiney, P. A., Fischer, J. E., McGhie, A. R., Romanow, W. J., Denenstein, A. M., McCauley Jr., J. P., Smith, A. B., Cox, D. E.** Orientational ordering transition in solid C_{60}. *Physical Review Letters* 66 (1991), 22, p. 2911

[87] **Heyde, M., Simon, G. H., Rust, H. P., Freund, H. J.** Probing adsorption sites on thin oxide films by dynamic force microscopy. *Applied Physics Letters* 89 (2006), 26, p. 263107

[88] **Heyes, D. M., Barber, M., Clarke, J. H. R.** Molecular-dynamics computer-simulation of surface properties of crystalline potassium-chloride. *Journal of the Chemical Society-Faraday Transactions* 73 (1977), p. 1485

[89] **Hill, E., Freelon, B., Ganz, E.** Diffusion of hydrogen on the Si(001) surface investigated by STM atom tracking. *Physical Review B* 60 (1999), 23, p. 15896

[90] **Hirano, S., Yogo, T., Kikuta, K.** Synthetic calcite single crystals for optical device. *Progress in Crystal Growth and Characterization of Materials* 23 (1992), p. 341

[91] **Hla, S.-W., Bartels, L., Meyer, G., Rieder, K.-H.** Inducing All Steps of a Chemical Reaction with the Scanning Tunneling Microscope Tip: Towards Single Molecule Engineering. *Physical Review Letters* 85 (2000), 13, p. 2777

[92] **Hölscher, H., Schwarz, U. D., Wiesendanger, R.** Calculation of the frequency shift in dynamic force microscopy. *Applied Surface Science* 140 (1999), 3-4, p. 344

[93] **Hofer, W. A., Foster, A. S., Shluger, A. L.** Theories of scanning probe microscopes at the atomic scale. *Reviews of Modern Physics* 75 (2003), p. 1287

[94] **Hölscher, H., Langkat, S. M., Schwarz, A., Wiesendanger, R.** Measurement of three-dimensional force fields with atomic resolution using dynamic force spectroscopy. *Applied Physics Letters* 81 (2002), 23, p. 4428

[95] **Israelachvili, J. N.**: *Intermolecular and Surface Forces.* Elsevier, 2011

[96] **Jin, M. X., Shimada, E., Ikuma, Y.** Observation of calcite $(10\bar{1}4)$ surface by AFM in air and surface structure analysis. *Journal of the Ceramic Society of Japan* 107 (1999), 12, p. 1166

[97] **Joachim, C., Gimzewski, J. K., Tang, H.** Physical principles of the single-C_{60} transistor effect. *Physical Review B* 58 (1998), 24, p. 16407

[98] **Joachim, Ch., Gimzewski, J. K., Aviram, A.** Electronics using hybrid-molecular and mono-molecular devices. *Nature* 408 (2000), p. 541

[99] **Kawai, S., Glatzel, T., Koch, S., Baratoff, A., Meyer, E.** Interaction-induced atomic displacement revealed by drift-corrected dynamic force spectroscopy. *Physical Review B* 83 (2011), p. 035421

[100] **Kawai, S., Maier, S., Glatzel, T., Koch, S., Such, B., Zimmerli, L., Fendt, L. A., Diederich, F., Meyer, E.** Cutting and self-healing molecular wires studied by dynamic force microscopy. *Applied Physics Letters* 95 (2009), 10, p. 103109

[101] **Keil, M., Samori, P., Santos, D. A., Kugler, T., Stafstrom, S., Brand, J. D., Müllen, K., Bredas, J. L., Rabe, J. P., Salaneck, W. R.** Influence of the morphology on the electronic structure of hexa-peri-hexabenzocoronene thin films. *Journal of Physical Chemistry B* 104 (2000), 16, p. 3967

[102] **Kellogg, G. L.** Field-ion microscope studies of single-atom surface-diffusion and cluster nucleation on metal-surfaces. *Surface Science Reports* 21 (1994), 1-2, p. 1

[103] **Kerisit, S., Parker, S. C., Harding, J. H.** Atomistic Simulation of the Dissociative Adsorption of Water on Calcite Surfaces. *The Journal of Physical Chemistry B* 107 (2003), 31, p. 7676

[104] **Kühnle, A.** Self-assembly of organic molecules at metal surfaces. *Current Opinion in Colloid and Interface Science* 14 (2009), p. 157

[105] **Kristensen, R., Stipp, S. L. S., Refson, K.** Modeling steps and kinks on the surface of calcite. *Journal of Chemical Physics* 121 (2004), 17, p. 8511

[106] **Körner, M., Loske, F., Einax, M., Kühnle, A., Reichling, M., Maass, P.** Second-layer induced island morphologies in thin-film growth of fullerenes. *in print, Physical Review Letters* (2011)

[107] **Kroto, H. W., Heath, J. R., O'Brien, S. C., Curl, R. F., Smalley, R. E.** C_{60}: buckminsterfullerene. *Nature* 318 (1985), 6042, p. 162

[108] **Krueger, M., Borovsky, B., Ganz, E.** Diffusion of adsorbed Si dimers on Si(001). *Surface Science* 385 (1997), 1, p. 146

[109] **Kunstmann, T., Schlarb, A., Fendrich, M., Wagner, T., Möller, R., Hoffmann, R.** Dynamic force microscopy study of 3,4,9,10-perylenetetracarboxylic dianhydride on KBr(001). *Physical Review B* 71 (2005), 12, p. 121403

[110] **La O, G. J., In, H. J., Crumlin, E., Barbastathis, G., Yang, S.-H.** Recent advances in microdevices for electrochemical energy conversion and storage. *International Journal of Energy Research* 31 (2007), 6-7, p. 548

[111] **Lackinger, M., Griessl, S., Heckl, W. A., Hietschold, M., Flynn, G. W.** Self-assembly of trimesic acid at the liquid-solid interface - a study of solvent-induced polymorphism. *Langmuir* 21 (2005), 11, p. 4984

[112] **Lackinger, M., Griessl, S., Kampschulte, L., Jamitzky, F., Heckl, W. M.** Dynamics of grain boundaries in two-dimensional hydrogen-bonded molecular networks. *Small* 1 (2005), 5, p. 532

[113] **Lahav, M., Leiserowitz, L.** Comments on "Mirror Symmetry Breaking" of the Centrosymmetric $CaCO_3$ Crystals with Amino Acids. *Angewandte Chemie International Edition* 120 (2008), 20, p. 3738

[114] **Langkat, S. M., Hölscher, H., Schwarz, A., Wiesendanger, R.** Determination of site specific interatomic forces between an iron coated tip and the NiO(001) surface by force field spectroscopy. *Surface Science* 527 (2003), 1-3, p. 12

[115] **Leeuw, N. H., Cooper, T. G.** A computational study of the surface structure and reactivity of calcium fluoride. *Journal of Materials Chemistry* 13 (2003), 1, p. 93

[116] **Leeuw, N. H., Parker, S. C.** Surface structure and morphology of calcium carbonate polymorphs calcite, aragonite, and vaterite: An atomistic approach. *Journal of Physical Chemistry B* 102 (1998), 16, p. 2914

[117] **Liang, Y., Lea, A. S., Baer, D. R., Engelhard, M. H.** Structure of the cleaved $CaCO_3(10\bar{1}4)$ surface in an aqueous environment. *Surface Science* 351 (1996), 1-3, p. 172

[118] **Linear Technology Corporation**: *LTC2420 20-Bit µPower No Latency ΔΣ ADC in SO-8*, 2000

[119] **Linear Technology Corporation**: *LTC1864/LTC1865 µPower, 16-Bit, 250ksps 1- and 2-Channel ADCs in MSOP*, 2007

[120] **Liu, W., Liu, X., Zheng, W. T., Jiang, Q.** Surface energies of several ceramics with NaCl structure. *Surface Science* 600 (2006), 2, p. 257

[121] **Loges, N., Wolf, S. E., Panthöfer, M., Müller, L., Reinnig, M.-C., Hoffmann, T., Tremel, W.** Reply to "Mirror Symmetry Breaking" of the Centrosymmetric $CaCO_3$ Crystals with Amino Acids. *Angewandte Chemie International Edition* 47 (2008), 20, p. 3683

[122] **Loske, F.**: *Tailoring molecule nanostructures on insulating surfaces investigated by non-contact atomic force microscopy*, Universität Mainz, Diss., 2011

[123] **Loske, F., Lübbe, J., Schütte, J., Reichling, M., Kühnle, A.** Quantitative description of C_{60} diffusion on an insulating surface. *Physical Review B* 82 (2010), 15, p. 155428

[124] **Loske, F., Rahe, P., Kühnle, A.** Contrast inversion in non-contact atomic force microscopy imaging of C_{60} molecules. *Nanotechnology* 20 (2009), 26, p. 264010

[125] **Lübbe, J.**: *priv. comm.* 2011

[126] **Lübbe, J.**: *PhD Thesis*, Universität Osnabrück, Diss., in preparation

[127] **Mackrodt, W. C., Stewart, R. F.** Defect properties of ionic solids .1. Point-defects at surfaces of face-centered cubic-crystals. *Journal of Physics C-Solid State Physics* 10 (1977), 9, p. 1431

[128] **MacLeod, J. M., Ivasenko, O., Perepichka, D. F., Rosei, F.** Stabilization of exotic minority phases in a multicomponent self-assembled molecular network. *Nanotechnology* 18 (2007), 42, p. 424031

[129] **Maier, S., Fendt, L.-A., Zimmerli, L., Glatzel, T., Pfeiffer, O., Diederich, F., Meyer, E.** Nanoscale engineering of molecular porphyrin wires on insulating surfaces. *Small* 4 (2008), 8, p. 1115

[130] **Marini, A., Garcia-Gonzalez, P., Rubio, A.** First-principles description of correlation effects in layered materials. *Physical Review Letters* 96 (2006), 13, p. 136404

[131] **Maxwell, A. J., Brühwiler, P. A., Arvanitis, D., Hasselström, J., Johansson, M. K.-J., Mårtensson, N.** Electronic and geometric structure of C_{60} on Al(111) and Al(110). *Physical Review B* 57 (1998), 12, p. 7312

[132] **McNaught, A. D., Wilkinson, A.**: *IUPAC. Compendium of Chemical Terminology, 2nd ed. (the "Gold Book")*. http://dx.doi.org/doi:10.1351/goldbook. Version: 2006

[133] **Melitz, W., Shen, J., Kummel, A. C., Lee, S.** Kelvin probe force microscopy and its application. *Surface Science Reports* 66 (2011), 1, p. 1

[134] **Meyer, G., Amer, N. M.** Novel optical approach to atomic force microscopy. *Applied Physics Letters* 53 (1988), 12, p. 1045

[135] **Meyer, G., Repp, J., Zöphel, S., Braun, K.-F., Hla, S. W., Fölsch, S., Bartels, L., Moresco, F., Rieder, K. H.** Controlled manipulation of atoms and small molecules with a low temperature scanning tunneling microscope. *Single Molecules* 1 (2000), 1, p. 79

[136] **Mirwald, P. W.** The electrical conductivity of calcite between 300 and 1200 C at a CO_2 pressure of 40 bars. *Physics and Chemistry of Minerals* 4 (1979), 291

[137] **Morita**, S. (Hrsg.), **Wiesendanger**, R. (Hrsg.), **Meyer**, E. (Hrsg.): *Noncontact Atomic Force Microscopy*. Springer, Berlin, 2002

[138] **Nabok, D., Puschnig, P., Ambrosch-Draxl, C.** Cohesive and surface energies of pi-conjugated organic molecular crystals: A first-principles study. *Physical Review B* 77 (2008), 24, p. 245316

[139] **NanoSurf AG**: *Nanosurf easyPLL plus Specifications*, 2008

[140] **Nanotec Electronica S.L.**: *Dulcinea SPM control system*. 2011

[141] **National Instruments**: *LabVIEW 8.6*. 2010

[142] **Necas, D., Klaptek, P., the Gwyddion community**: *Gwyddion – Free SPM data analysis software*. http://www.gwyddion.net

[143] **Nimmrich, M.**: *Untersuchung der Sublimationseigenschaften organischer Moleküle im Ultrahochvakuum*. Diplomarbeit, Universität Osnabrück, 2009

[144] **Nony, L., Bennewitz, R., Pfeiffer, O., Gnecco, E., Baratoff, A., Meyer, E., Eguchi, T., Gourdon, A., Joachim, C.** Cu-TBPP and PTCDA molecules on insulating surfaces studied by ultra-high-vacuum non-contact AFM. *Nanotechnology* 15 (2004), 2, p. S91

[145] **Nony, L., Gnecco, E., Baratoff, A., Alkauskas, A., Bennewitz, R., Pfeiffer, O., Maier, S., Wetzel, A., Meyer, E., Gerber, C.** Observation of individual molecules trapped on a nanostructured insulator. *Nano Letters* 4 (2004), 11, p. 2185

[146] **Northrup, J. E., Tiago, M. L., Louie, S. G.** Surface energetics and growth of pentacene. *Physical Review B* 66 (2002), 12

[147] **Omicron NanoTechnology**: *MATE MATRIX Automated Task Environment*, 2010

[148] **Omicron NanoTechnology**: *Vernissage MATRIX Result File Access and Export*, 2010

[149] **Orme, C. A., Noy, A., Wierzbicki, A., McBride, M. T., Grantham, M., Teng, H. H., Dove, P. M., DeYoreo, J. J.** Formation of chiral morphologies through selective binding of amino acids to calcite surface steps. *Nature* 411 (2001), p. 775

[150] **Pakarinen, O. H., Barth, C., Foster, A. S., Henry, C. R.** Imaging the real shape of nanoclusters in scanning force microscopy. *Journal of Applied Physics* 103 (2008), 5, p. 054313

[151] **Paz, Y., Luo, Z., Rabenberg, L., Heller, A.** Photooxidative Self-Cleaning Transparent Titanium-Dioxide Films on Glass. *Journal of Materials Research* 10 (1995), 11, p. 2842

[152] **Perkins, F. W., Post, D. E., Uckan, N. A., Azumi, M., Campbell, D. J., Ivanov, N., Sauthoff, N. R., Wakatani, M., Nevins, W. M., Shimada, M., Van Dam, J., Boucher, D., Cordey, G., Costley, A., Jacquinot, J., Janeschitz, G., Mirnov, S., Mukhovatov, V., Porter, G., Putvinski, S., Stambaugh, R., Wesley, J., Young, K., Aymar, R., Shimomura, Y., Fujisawa, N., Igitkhanov, Y., Kukushkin, A., Rosenbluth, M.** Chapter 1: Overview and summary. *Nuclear Fusion* 39 (1999), 12, p. 2137

[153] **Pohl, D. W., Möller, R.** Tracking Tunneling Microscopy. *Review of Scientific Instruments* 59 (1988), 6, p. 840

[154] **Prauzner-Bechcicki, J. S., Godlewski, S., Tekiel, A., Cyganik, P., Budzioch, J., Szymonski, M.** High-Resolution STM Studies of Terephthalic Acid Molecules on Rutile TiO2(110)-(1x1) Surfaces. *Journal of Physical Chemistry C* 113 (2009), p. 9305–9315

[155] **Proehl, H., Toerker, M., Sellam, F., Fritz, T., Leo, K., Simpson, C., Mullen, K.** Comparison of ultraviolet photoelectron spectroscopy and scanning tunneling spectroscopy measurements on highly ordered ultrathin films of hexa-peri-hexabenzocoronene on Au(111). *Physical Review B* 63 (2001), 20, p. 205409

[156] **Puchin, V. E., Puchina, A. V., Huisinga, M., Reichling, M.** Theoretical modelling of steps on the CaF_2(111) surface. *Journal of Physics-Condensed Matter* 13 (2001), 10, p. 2081

[157] **Qin, X. R., Swartzentruber, B. S., Lagally, M. G.** Diffusional Kinetics of SiGe Dimers on Si(100) Using Atom-Tracking Scanning Tunneling Microscopy. *Physical Review Letters* 85 (2000), Oct, 17, p. 3660

[158] **Rachlin, A. L., Henderson, G. S., Goh, M. C.** An atomic force microscope (AFM) study of the calcite cleavage plane: image averaging in Fourier space. *American Mineralogist* 77 (1992), 9-10, p. 904

[159] **Rahe, P.**: *Adsorptionseigenschaften von organischen Molekülen auf Titandioxid untersucht mit hochauflösender Rasterkraftmikroskopie*. Diplomarbeit, Universität Osnabrück, 2008

[160] **Rahe, P., Bechstein, R., Kühnle, A.** Vertical and lateral drift corrections of scanning probe microscopy images. *Journal of Vacuum Science and Technology B* 28 (2010), 3, p. C4E31

[161] **Rahe, P., Bechstein, R., Schütte, J., Ostendorf, F., Kühnle, A.** Repulsive interaction and contrast inversion in noncontact atomic force microscopy imaging of adsorbates. *Physical Review B* 77 (2008), 19, p. 195410

[162] **Rahe, P., Nimmrich, M., Greuling, A., Schütte, J., Stará, I.G., Rybáček, J., Huerta-Angeles, G., Starý, I., Rohlfing, M., Kühnle, A.** Toward Molecular Nanowires Self-Assembled on an Insulating Substrate: Heptahelicene-2-carboxylic acid on Calcite ($10\bar{1}4$). *Journal of Physical Chemistry C* 114 (2010), 3, p. 1547

[163] **Rahe, P., Nimmrich, M., Nefedov, A., Naboka, M., Wöll, Ch., Kühnle, A.** Transition of Molecule Orientation during Adsorption of Terephthalic Acid on Rutile TiO2(110). *Journal of Physical Chemistry C* 113 (2009), 40, p. 17471

[164] **Rahe, P., Schütte, J., Schniederberend, W., Reichling, M., Abe, M., Sugimoto, Y., Kühnle, A.** Flexible drift-compensation system for precise 3D force mapping in severe drift environments. *Review of Scientific Instruments* 82 (2011), p. 063704

[165] **Rao, K., Rao, K.** Dielectric dispersion and its temperature variation in calcite single crystals. *Zeitschrift für Physik A Hadrons and Nuclei* 216 (1968), 300

[166] **Reeder**, Richard J. (Hrsg.): *Carbonates: mineralogy and chemistry*. Washington, D.C. : Mineralogical Society of America, 1983 (Reviews in mineralogy)

[167] **Rieger, J., Thieme, J., Schmidt, C.** Study of precipitation reactions by X-ray microscopy: $CaCO_3$ precipitation and the effect of polycarboxylates. *Langmuir* 16 (2000), 22, p. 8300

[168] **Robertson, J., Trotter, J.** Crystal-structure studies of polynuclear hydrocarbons .6. 1,12-2,3-4,5-6,7-8,9-10,11-hexabenzocoronene. *Journal of the Chemical Society* (1961), p. 1280

[169] **Rode, S., Oyabu, N., Kobayashi, K., Yamada, H., Kühnle, A.** True Atomic-Resolution Imaging of ($10\bar{1}4$) Calcite in Aqueous Solution by Frequency Modulation Atomic Force Microscopy. *Langmuir* 25 (2009), 5, p. 2850–2853

[170] **Rohl, A. L., Wright, K., Gale, J. D.** Evidence from surface phonons for the (2x1) reconstruction of the ($10\bar{1}4$) surface of calcite from computer simulation. *American Mineralogist* 88 (2003), 5-6, p. 921

[171] **Rohlfing, M., Bredow, T.** Binding Energy of Adsorbates on a Noble-Metal Surface: Exchange and Correlation Effects. *Physical Review Letters* 101 (2008), 26, p. 266106

[172] **Ruffieux, P., Groning, O., Bielmann, M., Simpson, C., Mullen, K., Schlapbach, L., Groning, P.** Supramolecular columns of hexabenzocoronenes on copper and gold(111) surfaces. *Physical Review B* 66 (2002), 7, p. 073409

[173] **Rulíšek, L., Exner, O., Cwiklik, L., Jungwirth, P., Starý, I., Pospíšil, L., Havlas, Z.** On the convergence of the physicochemical properties of [n]helicenes. *Journal of Physical Chemistry C* 111 (2007), p. 14948

[174] **Ruschmeier, K., Schirmeisen, A., Hoffmann, R.** Atomic-Scale Force-Vector Fields. *Physical Review Letters* 101 (2008), 15, p. 156102

[175] **Ruschmeier, K., Schirmeisen, A., Hoffmann, R.** Site-specific force-vector field studies of KBr(001) by atomic force microscopy. *Nanotechnology* 20 (2009), 26, p. 264013

[176] **Rybáček, J., Huerta-Angeles, G., Kollárovič, A., Stará, I. G., Starý, I., Rahe, P., Nimmrich, M., Kühnle, A.** Racemic and Optically Pure Heptahelicene-2-carboxylic Acid: Its Synthesis and Self-Assembly into Nanowire-Like Aggregates. *European Journal of Organic Chemistry* 2011 (2011), 5, p. 853

[177] **Sader, J. E., Jarvis, S. P.** Accurate formulas for interaction force and energy in frequency modulation force spectroscopy. *Applied Physics Letters* 84 (2004), 10, p. 1801

[178] **Sadewasser, S., Carl, P., Glatzel, T., Lux-Steiner, M.** Influence of uncompensated electrostatic force on height measurements in non-contact atomic force microscopy. *Nanotechnology* 15 (2004), 2, p. S14

[179] **Samara, G. A., Schirber, J. E., Morosin, B., Hansen, L. V., Loy, D., Sylwester, A. P.** Pressure dependence of the orientational ordering in solid C_{60}. *Physical Review Letters* 67 (1991), 22, p. 3136

[180] **Schirmeisen, A., Weiner, D., Fuchs, H.** Single-Atom Contact Mechanics: From Atomic Scale Energy Barrier to Mechanical Relaxation Hysteresis. *Physical Review Letters* 97 (2006), 13, p. 136101

[181] **Schlapbach, L., Zuttel, A.** Hydrogen-storage materials for mobile applications. *Nature* 414 (2001), 6861, p. 353

[182] **Schmitz-Hübsch, T., Sellam, F., Staub, R., Toerker, M., Fritz, T., Kubel, C., Müllen, K., Leo, K.** Direct observation of organic-organic heteroepitaxy: perylene-tetracarboxylic-dianhydride on hexa-peri-benzocoronene on highly ordered pyrolytic graphite. *Surface Science* 445 (2000), 2-3, p. 358

[183] **Schunack, M.**: *Scanning Tunneling Microscopy Studies of Organic Molecules on Metal Surfaces*, University of Aarhus, Diss., 2002

[184] **Schütte, J.**: *Abbildung organischer Moleküle auf dielektrischen Oberflächen.* Göttingen, Universität Osnabrück, Diss., 2009

[185] **Schütte, J., Rahe, P., Tröger, L., Rode, S., Bechstein, R., Reichling, M., Kühnle, A.** Clear signature of the (2x1) reconstruction of calcite $(10\bar{1}4)$. *Langmuir* 26 (2010), 11, p. 8295

[186] **Schwarz, A., Hölscher, H., Langkat, S. M., Wiesendanger, R.** Three-Dimensional Force Field Spectroscopy. *Scanning Tunneling Microscopy-/Spectroscopy and Related Techniques: 12th International Conf.*, 696 (2003), 1, p. 68

[187] **Sehnal, Petr, Stará, Irena G., Šaman, David, Tichý, Miloš, Míšek, Jiří, Cvačka, Josef, Rulíšek, Lubomír, Chocholoušová, Jana, Vacek, Jaroslav, Goryl, Grzegorz, Szymonski, Marek, Císařová, Ivana, Starý, Ivo**. An organometallic route to long helicenes. *Proceedings of the National Academy of Sciences* 106 (2009), 32, p. 13169

[188] **Sellam, F., Schmitz-Hübsch, T., Toerker, M., Mannsfeld, S., Proehl, H., Fritz, T., Leo, K., Simpson, C., Müllen, K.** LEED and STM investigations of organic-organic heterostructures grown by molecular beam epitaxy. *Surface Science* 478 (2001), 1-2, p. 113

[189] **Sheerin, G., Cafolla, A. A.** Self-assembled structures of trimesic acid on the Ag/Si(111)-$(\sqrt{3}\times\sqrt{3})$R30 surface. *Surface Science* 577 (2005), 2-3, p. 211

[190] **Shuttleworth, R.** The surface energies of inert-gas and ionic crystals. *Proceedings of the Physical Society of London Section A* 62 (1949), 351, p. 167

[191] **Simon, G.H., Heyde, M., Rust, H.-P.** Recipes for cantilever parameter determination in dynamic force spectroscopy: spring constant and amplitude. *Nanotechnology* 18 (2007), 25, 255503

[192] **Skinner, A. J., LaFemina, J. P., Jansen, H. J. F.** Structure and Bonding of Calcite - a Theoretical-Study. *American Mineralogist* 79 (1994), 3-4, p. 205

[193] **Specs Zurich GmbH**: *Nanonis SPM control system with AT4 module.* 2011

[194] **Spillmann, H., Dmitriev, A., Lin, N., Messina, P., Barth, J. V., Kern, K.** Hierarchical Assembly of Two-Dimensional Homochiral Nanocavity Arrays. *Journal of the American Chemical Society* 125 (2003), 35, p. 10725

[195] **Stepanow, S., Lingenfelder, M., Dmitriev, A., Spillmann, H., Delvigne, E., Lin, N., Deng, X., Cai, C., Barth, J. V., Kern, K.** Steering molecular organization and host-guest interactions using two-dimensional nanoporous coordination systems. *Nature Materials* 3 (2004), 4, p. 229

[196] **Stepanow, S., Strunskus, T., Lingenfelder, M., Dmitriev, A., Spillmann, H., Lin, N., Barth, J. V., Wöll, C., Kern, K.** Deprotonation-Driven Phase Transformations in Terephthalic Acid Self-Assembly on Cu(100). *Journal of Physical Chemistry B* 108 (2004), 50, p. 19392

[197] **Stipp, S. L., Hochella, M. F.** Structure and Bonding Environments at the Calcite Surface as Observed with X-Ray Photoelectron-Spectroscopy (XPS) and Low-Energy Electron-Diffraction (LEED). *Geochimica Et Cosmochimica Acta* 55 (1991), 6, p. 1723

[198] **Stipp, S. L. S., Eggleston, C. M., Nielsen, B. S.** Calcite Surface-Structure Observed at Microtopographic and Molecular Scales with Atomic-Force Microscopy (AFM). *Geochimica Et Cosmochimica Acta* 58 (1994), 14, p. 3023

[199] **Stroscio, J., Eigler, D. M.** Atomic and Molecular Manipulation with the Scanning Tunneling Microscope. *Science* 254 (1991), p. 1319

[200] **Stuart, S. J., Tutein, A. B., Harrison, J. A.** A reactive potential for hydrocarbons with intermolecular interactions. *The Journal of Chemical Physics* 112 (2000), 14, p. 6472

[201] **Such, B., Glatzel, T., Kawai, S., Koch, S., Meyer, E.** Three-dimensional force spectroscopy of KBr(001) by tuning fork-based cryogenic noncontact atomic force microscopy. *Journal of Vacuum Science & Technology B* 28 (2010), 3, p. C4B1

[202] **Sugimoto, Y., Namikawa, T., Miki, K., Abe, M., Morita, S.** Vertical and lateral force mapping on the Si(111)-(7x7) surface by dynamic force microscopy. *Physical Review B* 77 (2008), 19, p. 195424

[203] **Sugimoto, Y., Pou, P., Abe, M., Jelinek, P., Perez, R., Morita, S., Custance, Ó.** Chemical identification of individual surface atoms by atomic force microscopy. *Nature* 446 (2007), p. 64

[204] **Swartzentruber, B. S.** Direct measurement of surface diffusion using atom-tracking scanning tunneling microscopy. *Physical Review Letters* 76 (1996), 3, p. 459–62

[205] **Swartzentruber, B. S., Smith, A. P., Jónsson, H.** Experimental and Theoretical Study of the Rotation of Si Ad-dimers on the Si(100) Surface. *Physical Review Letters* 77 (1996), Sep, 12, p. 2518

[206] **Tans, S. J., Verschueren, A. R. M., Dekker, C.** Room-temperature transistor based on a single carbon nanotube. *Nature* 393 (1998), 6680, p. 49

[207] **Tasker, P. W.** Surface energies, surface tensions and surface-structure of the alkali-halide crystals. *Philosophical Magazine A-Physics of Condensed Matter Structure Defects and Mechanical Properties* 39 (1979), 2, p. 119

[208] **Tekiel, A., Prauzner-Bechcicki, J. S., Godlewski, S., Budzioch, J., Szymonski, M.** Self-assembly of terephthalic acid on rutile TiO2(110): Toward chemically functionalized metal oxide surfaces. *Journal of Physical Chemistry C* 112 (2008), 33, p. 12606

[209] **Toerker, M., Fritz, T., Proehl, H., Gutierrez, R., Grossmann, F., Schmidt, R.** Electronic transport through occupied and unoccupied states of an organic molecule on Au: Experiment and theory. *Physical Review B* 65 (2002), 24, p. 245422

[210] **Toumey, C.** Apostolic Succession. *Engineering & Science* 1/2 (2005), p. 16

[211] **Traco Power**: *DC/DC converters datasheet,* 2010

[212] **Treboux, G., Lapstun, P., Wu, Z. H., Silverbrook, K.** Electronic conductance of helicenes. *Chemical Physics Letters* 301 (1999), 5-6, p. 493

[213] **Tröger, L., Schütte, J., Ostendorf, F., Kühnle, A., Reichling, M.** Concept for support and cleavage of brittle crystals. *Review of Scientific Instruments* 80 (2009), 6, p. 063703

[214] **Valdes, H., Klusak, V., Pitonak, M., Exner, O., Stary, I., Hobza, P., Rulisek, L.** Evaluation of the intramolecular basis set superposition error in the calculations of larger molecules: [n]Helicenes and Phe-Gly-Phe tripeptide. *Journal of Computational Chemistry* 29 (2008), 6, p. 861

[215] **Van Zeggeren, F., Benson, G. C.** Calculation of the surface energies of alkali halide crystals. *Journal of Chemical Physics* 26 (1957), 5, p. 1077

[216] **Venables, J. A.**: *Introduction to Surface and Thin Film Processes.* Cambridge University Press, 2000

[217] **Vitos, L., Ruban, A. V., Skriver, H. L., Kollar, J.** The surface energy of metals. *Surface Science* 411 (1998), 1-2, p. 186

[218] **Wagner, C., Kasemann, D., Golnik, C., Forker, R., Esslinger, M., Mullen, K., Fritz, T.** Repulsion between molecules on a metal: Monolayers and submonolayers of hexa-peri-hexabenzocoronene on Au(111). *Physical Review B* 81 (2010), 3, p. 035423

[219] **Weast**, R.C. (Hrsg.), **Astle**, M.J. (. (Hrsg.): *Handbook of Chemistry and Physics*. Bocy Raton, FL : CRC Press, 1981 (62nd ed.)

[220] **Whitesides, G. M., Grzybowski, B.** Self-assembly at all scales. *Science* 295 (2002), 5564, p. 2418

[221] **WinAVR**: *WinAVR Project*. http://winavr.sourceforge.net

[222] **Winchell, H.** The unit cells of calcite. *American Journal of Science* 254 (1956), 2, p. 65

[223] **Wolf, S. E., Loges, N., Mathiasch, B., Panthöfer, M., Mey, I., Janshoff, A., Tremel, W.** Phasenselektion von Calciumcarbonat durch die Chiralität adsorbierter Aminosäuren. *Angewandte Chemie* 119 (2007), 29, p. 5716

[224] **Wollbrandt, J., Linke, W., Brückner, U.** Untersuchung elektrostatischer Aufladungen auf Spaltflächen von Alkalihalogenideinkristallen. *Experimentelle Technik der Physik* 23 (1975), p. 65

[225] **Yaghi, O. M., O'Keeffe, M., Ockwig, N. W., Chae, H. K., Eddaoudi, M., Kim, J.** Reticular synthesis and the design of new materials. *Nature* 423 (2003), 6941, p. 705

[226] **Ye, Y. C., Sun, W., Wang, Y. F., Shao, X., Xu, X. G., Cheng, F., Li, J. L., Wu, K.** A unified model: Self-assembly of trimesic acid on gold. *Journal of Physical Chemistry C* 111 (2007), 28, p. 10138

[227] **Yokoyama, T., Kamikado, T., Yokoyama, S., Mashiko, S.** Conformation selective assembly of carboxyphenyl substituted porphyrins on Au (111). *Journal of Chemical Physics* 121 (2004), 23, p. 11993

[228] **Zimmermann, U., Karl, N.** Epitaxial-growth of coronene and hexa-peri-benzocoronene on MoS2(0001) and graphite (0001) - A LEED study of molecular-size effects. *Surface Science* 268 (1992), 1-3, p. 296

A. Surface energies

Table A.1.: List of surface energies reported in literature. The values reported in literature differ slightly, the used value is an average.

Substrate	γ in mJ/m^2	References
Metal substrates		
Fe(100)	2714	Ref. [217]
Pt(111)	2333	Ref. [217]
Pd(111)	1903	Ref. [217]
Cu(111)	1877	Ref. [217]
Au(111)	1332	Ref. [217]
Ag(111)	1220	Ref. [217]
Al(111)	1110	Ref. [217]
Dielectric substrates		
$CaCO_3$(10.4)	590	Refs. [105, 50, 116]
CaF_2(111)	480	Refs. [71, 115, 156]
MgO(100)	377	Ref. [120]
CaO(100)	370	Ref. [120]
NaF(100)	261	Refs. [215, 207, 26, 190, 127]
NaCl(100)	181	Refs. [215, 207, 26, 190, 127]
KCl(100)	157	Refs. [215, 207, 26, 190, 88]
KBr(100)	141	Refs. [215, 207, 26, 190]
Molecules		
Sexiphenyl(100)	142	Ref. [138]
C_{60}	116	Ref. [72]
Pentacene(001)	102	Ref. [146]
Anthracene(010)	91	Ref. [146]
Pentacene(010)	47	Ref. [146]

B. Atom tracking: technical details

In this Section details on the technical implementation of the atom-tracking system are given. The functionality of the microcontroller inside the atom-tracking system is split into numerous modules. A short description for every module is given here, while the concrete implementation can be found in the sourcecode.

Timing module The microcontroller is operating at about 16 MHz, by default using an internal oscillator. As these oscillators usually do not provide a reasonable stability, an external quartz crystal oscillator is connected to define the system clock. The crystal frequency of this quartz was measured with a frequency counter[1] to (15998342 ± 10) Hz and is defined in `settings.h` as macro `F_CPU`. Still the external quartz is subject to temperature drift, therefore, I include a large error for the measurement.

The 16 bit Timer/Counter unit `Timer/Counter1` is used to define the absolute time. The compare match A of this Timer/Counter is triggered every second and executes the interrupt routine `ISR(TIMER1_COMPA_vect)`. This interrupt routine increments the register `status.timing_timesec` by one and toggles the front LED "Clock". The sub-second resolution is given from the current value of `Timer/Counter1`. A Labview script is available to convert between this value and milliseconds. The resulting resolution is about 64 µs

The absolute timing is wrong by a few seconds per day due to two reasons: First the `Timer/Counter1` is a 16 bit integer counter and, thus, the trigger rate is systematically incorrect by a maximum of about 64 µs. Second, the external oscillator is not temperature stabilised, causing a reference frequency shift with temperature. However, these errors are neglectible.

The timing module features two more triggers, namely the 16 bit `Timer/Counter4` and the 8 bit `Timer/Counter0`. The former is designed to trigger the code execution of time-critical modules. Specifically, the main programmes for the tracking feedback loop, the feedforward update, the tip-positioning update and the oscilloscopes are executed in the main loop in case the interrupt service routine `ISR(TIMER4_COMPA_vect)` has set the respective trigger.

[1] 53181A RF Frequency Counter (Agilent Technologies, Santa Clara CA, USA).

For less time-critical tasks, the interrupt service routine for `Timer/Counter0`, `ISR(TIMER0_COMPA_vect)`, is executed with a rate of ∼ 5 Hz. This routine triggers the status module, which sends the current tip positions to the computer. Additionally, if the tracking is paused, it triggers the flashing of the LED "Tracking Loop".

Settings module The settings and the current status of the whole atom-tracking system is completely stored inside the microcontroller. According to the concept of a finite state machine, the Labview scripts on the computer induce state changes and set or request parameters. The states for each module are centralised in the C struct `status`, defined in file `settings.h`. The configuration of the system is available in a second C struct `configuration`, also defined in the file `settings.h`. These registers are accessible by all modules.

Communication module The communication with the controlling computer is implemented using a serial byte protocol. The parameters for this serial communication, such as baud rate, frame length and stop bits, are defined in `comm.h` and `comm.c`.

The data is transmitted bytewise via the serial connection, consequently an input (`comm_ibuffer`) and an output (`comm_obuffer`) buffer is used for each transmission direction. These buffers are ring buffers as implemented in the file `bufferc.h`. The size of these buffers is monitored and read or write operations to the buffers may be prohibited. In this case, full transmission frames are dropped but the communication remains intact. As the execution or failure of any command is reported to the PC, the drop of a complete frame is usually detected.

The communication uses an asynchronous protocol, in which each transmitted frame has a header and a body as depicted in Figure B.1. The header consists

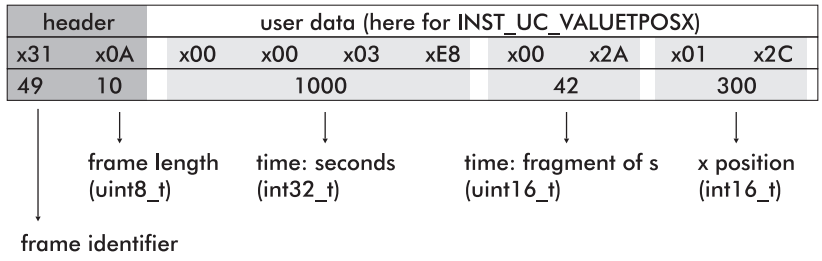

Figure B.1.: Layout of a frame transmitted from the microcontroller to the PC. As an example, the frame with identifier `INST_UC_VALUETPOSX` is chosen. This frame sends the lateral X-position while the tracking is active.

of two bytes: frame identification and frame length, each given as an unsigned 8 bit integer value. Consequently, the shortest possible frame is of length 2 byte.

All instructions are defined in `commands.h` in form of precompiler macros. The instructions send by the PC start with `INST_PC_<...>` and frames send by the microcontroller start with `INST_UC_<...>`. The file `commands.h` is parsed by the Labview programme every time during startup to ensure the command set integrity.

Analog-digital conversion In the harware version 1, the ADC of the ATMega 2560 microcontroller [12] is used. This ADC has a resolution of 10 bit. A multiplexer is connected upstream, yielding a theoretical maximum of 16 analog input channels. The input channels are the $\mathrm{LIA_x}$ and $\mathrm{LIA_y}$ signals (LIA-X, LIA-Y) from the lock-in amplifier, the two front potentiometers (POTI-X, POTI-Y) for fine tip-positioning and a spare channel (AuxIn). The characteristics of this ADC are analysed with the results presented in Section 4.5.1 and yield an overall poor performance for this application. Although all measurements presented in this work are performed using the 10 bit ADC, a two channel 16 bit ADC (LTC1865 from Linear Technology [119]) is included in a hardware version 2 for the LIA-X and LIA-Y conversion and the potentiometers for the fine tip-positioning are connected by a serial interface. The usage of the high-speed 16 bit ADC increased the stability and performance of the lateral feedback loops significantly.

The ATMega 2560 internal 10 bit converters are read out interrupt driven, employing the `ISR(ADC_vect)` function. This routine is executed every time the conversion of a single value is finished. Depending on the channel and precision required, several values are collected and averaged before evaluating them in the programme flow. The external 20 bit converter is triggered using `Timer/Counter5`, employing the compare match A in `ISR(TIMER5_COMPA_vect)`. The converter is read with an interval of 160 ms, according to the conversion time needed. In hardware version 2, this interrupt routine is triggered at a rate of 2 kHz to read out the external 2-channel 16 bit ADC. The readout of the 20 bit converter is still performed at a 160 ms interval.

All valid ADC values are written into registers in the `adcin` struct, which is defined in `adc.h`. For every input channel, a register for the value and one for the status is reserved. Each module has a reserved bit in the latter registers, which are all reset when a new value is stored to the `adcin` struct. Therefore, each module is able to test for new sampled values. The access to these registers is made atomic[2] using the predefined macros in `<util/atomic.h>`, as asynchronous ac-

[2] The used microcontroller is a 8 bit type, therefore, several clock cycles are needed to access registers larger than 8 bit. In this context, *atomic* denotes microcontroller code executed with all interrupt routines deactivated.

cess needs to be possible within the microcontroller programme.

Two systematic errors typically occur during an analog-digital conversion and both need to be discussed. The so-called *offset*- and *gain*-error denote deviations from an ideal working ADC with identity as its transfer function. The *offset*-error denotes a constant offset, while the *gain*-error denotes the deviation in the slope from the ideal transfer function. For input channels LIA-X and LIA-Y, correction factors for the *offset*-error were determined and are defined in the `adccorr` struct. Every sampled value is corrected by this offset before written to the `adcin` struct. For these two channels, this is of large importance, as the tip would oscillate displaced from the centre of the surface protrusion in case of a large offset error.

Oscilloscopes An oscilloscope functionality is implemented in `oscis.c`. Each input channel defined in the `adcin` struct can be monitored, while the update rate is triggered by `Timer/Counter4`. It should be noted, only new sampled values are transmitted in case the trigger is faster than the respective ADC conversion time. This strategy is supported by the status register associated with each input register in the `adcin` struct.

Digital-analog conversion External converters of type DAC712 (Burr-Brown) are used for the analog output channels. They are connected via a 16 bit parallel interface using ports `PORTA` (low byte) and `PORTC` (high byte). The X- and Y-channels are each differential channels, but each is handled as a single output channel throughout the microcontroller code apart from the output routines `dac_save_setx()` and `dac_save_sety()` in `dac.h`.

The struct `cfgout` holds the current valid output value from each module and for each output channel. The physical output for each output channel is defined by the sum of all these contributions. Writing the output to a single or all DACs is triggered by the functions `dac_set_x`, `dac_set_y` and `dac_set_z` in `dac.h`. Each function sums the respective values, tests for overflows in 32 bit arithmetic and writes the resulting value of type signed 16 bit integer to the output registers. The operational amplifier connected to each DAC is wired up such, that it inverts the signal. Therefore, all output values are inverted before writing them to the respective DAC.

With this design, each module can operate individually to a large degree, leading to a very flexible signal output stage.

Sine waveform generation The sine waveform is generated by direct digital synthesis (DDS). Precisely, the values for one period are precalculated using the current frequency $f_{x,y}$ and amplitude $A_{x,y}$. $N_{x,y}$ defines the number of elements

calculated and stored in a linear list. The memory for this list is dynamically allocated at `stat.sin_table` with the necessary code defined in the file `sin.c`. The list has the size $N_{x,y} \times 2$ byte.

An interrupt routine `ISR(TIMER3_COMPA_vect)` is triggered by the compare match A of `Timer/Counter3` and directly writes the sine values to the digital-analog converters. Additionally, the reference signal for the lock-in amplifier is governed by this interrupt routine. The interrupt routine trigger rate f_R depends on the sine frequency and the number of points and is given by

$$f_R = f_{x,y} \times N_{x,y}/2 \tag{B.1}$$

The period of the trigger rate has to be larger than the execution time of the interrupt routine itself, therefore, the dither frequency $f_{x,y}$ and element number $N_{x,y}$ has to be limited to a maximum frequency of 100 Hz and 128 points. As the frequencies are usually in the order of a few tens of Hz, no jitter[3] effects are expected and observed.

Tracking The tracking module uses two independent proportional-integral (PI) feedback loops. Each loop uses one output of the lock-in amplifier as the actual signal. From the first tracking experiments it becam evident, that the integral part of this feedback loop is sufficient to regulate the tip repositioning.

The feedback loop algorithm is triggered by `Timer/Counter3`, but executed in the main programme loop. This strategy is followed as time-consuming floating-point arithmetic is used in the feedback loop calculation which would block the sine generation for short time intervals. The main loop is with all modules active still working at a rate of more than 1 kHz, which is fast enough for a stable feedback loop algorithm.

Feedforward and drift model For future flexibility, the feedforward uses a so-called *drift model* for each feedforward output channel. One model is defined for each spatial direction in `driftmodel.h` and concentrates parameters for the long-term drift behaviour. Currently, only linear drift is implemented.

The drift velocities for each direction are determined from linear least-squares fits to the $x(t)$, $y(t)$ and $z(t)$ data in the Labview interface on the computer side. The resulting velocity for each channel is stored in each of the three `driftmodel` structs. Each model is implemented as a mathematical function with the absolute time as the main variable to gain maximum flexibility.

The feedforward module is triggered by `Timer/Counter3`. During each execution, the function `dmodel_getvalue()` is called for each spatial direction, with

[3] Jitter denotes the variation of amplitude, phase or frequency of a digital signal. Here, this could easily happen when the interrupt routine is not executed with the exact same periodicity.

the valid driftmodel and the current time as arguments. The current feedforward values are calculated from the parameters and the selected model in the relevant `driftmodel`. The feedforward module writes these values to the `cfgout` struct and forces the write to all DACs.

Each driftmodel has a function `dmodel_update()`, which is called every time before the feedforward module is activated. This function ensures a correct offset definition for the current driftmodel based on the valid time and current output value of the feedforward module and, thus, avoids tip jumps.

Tip positioning (potentiometers) Two 10-turn precision potentiometers are availbale at the ADC channels Poti-X and Poti-Y. In hardware version 1, they are read out using the internal ADC with 10 bit resolution. For hardware version 2, three 10-turn precision potentiometers are connected via a second serial interface. These potentiometers are read out using an Arduino Uno board [10] with a 10 bit build-in ADC in an Atmel ATMega328P microcontroller. The communication with this microcontroller is realised via an USART connection following the same protocol as the communication with the computer. It is defined in the file `adc.c`.

To avoid uncontrolled tip movements while activating the potentiometers, the first sampled value after activation is always used as the zero position. Additionally, if one potentiometer reaches the hardware limit at a small gain, it can simply be deactivated, turned back and reactivated. The poti functionality is triggered by `Timer/Counter3`, but updates are only written to the DACs if a new value is sampled.

To change the precision of the potentiometers, gain factors are defined in registers `status.potis_facxy` and `status.potis_facz` for the lateral and vertical direction, respectively. The physical precision furthermore depends on the sensitivity of the piezo scanner. Values for characteristic gains are listed in Tab. B.1 for the X,Y and Z direction. These values are calculated for the herein used Omicron VT AFM 25.

Status reporting The current output status, which is the sum of all components, can be monitored with a low update rate. The used trigger is `Timer/Counter0` running at ~5 Hz, however, its execution rate can be further reduced by setting the parameter `INST_PA_TRIGGER_STATUS_DIVIDER`. The microcontroller code is defined in `status.c`. Reporting the status is activated with the Labview vi gui_status.vi and at the same time, the current tip positioning values are stored in the respective logfile. Please note, this logging is again deactivated when closing the vi gui_status.vi.

Channel	gain	minimum step	one turn	maximum range (10 turns)
	1	8.04 pm	0.82 nm	8.24 nm
	2	16.09 pm	1.64 nm	16.48 nm
	3	24.13 pm	2.46 nm	24.71 nm
X,Y	4	32.18 pm	3.28 nm	32.95 nm
	16	128.71 pm	13.13 nm	131.80 nm
	32	257.42 pm	26.26 nm	263.60 nm
	64	514.84 pm	52.51 nm	527.20 nm
	1	2.56 pm	0.26 nm	2.63 nm
	2	5.13 pm	0.52 nm	5.25 nm
	3	7.69 pm	0.78 nm	7.88 nm
Z	4	10.25 pm	1.05 nm	10.50 nm
	16	41.02 pm	4.18 nm	42.00 nm
	32	82.03 pm	8.37 nm	84.00 nm
	64	164.06 pm	16.73 nm	168.00 nm

Table B.1.: Precision of the potentiometers. The piezo sensitivity in the lateral direction is 26.36 nm/V, in the vertical direction 8.4 nm/V.

C. Model for drift velocity calculation

Starting from the heat equation

$$\frac{\partial u}{\partial t} = D\frac{\partial^2 u}{\partial x^2} \tag{C.1}$$

with the initial condition

$$u(x,0) = \varphi(x) = \begin{cases} 0 & \text{if } 0 \le x \le L_1 \\ -\Delta T & \text{if } L_1 < x \le L \end{cases} \tag{C.2}$$

and the boundary conditions

$$I. \qquad u(0,t) = 0 \tag{C.3}$$

$$II. \qquad \left.\frac{\partial u}{\partial x}\right|_{x=L} = 0, \tag{C.4}$$

the temperature distribution u along a one-dimensional rod of length L is calculated. The geometry is presented in Figure C.1. For the derivation $T_0 = 0$ is chosen, this will later be corrected by adding T_0 to $u(x,t)$.

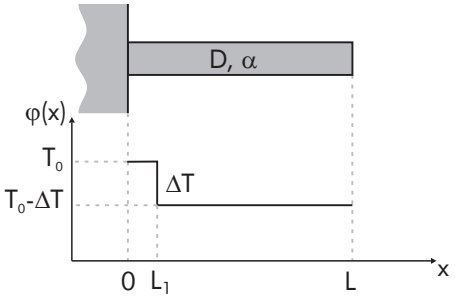

Figure C.1.: Model used for the drift velocity calculation. A one-dimensional rod, with material parameters thermal diffusivity D and coefficient of thermal expansion α, is connected to a heat reservoir on its left side. The lower graph depicts the initial temperature distribution.

Using a separation ansatz $u(x,t) = X(x)T(t)$, the differential equation reads

$$\frac{1}{D}\frac{\dot{T}}{T} = \frac{X''}{X} = -\lambda^2 \tag{C.5}$$

with a constant λ. The solutions are given by

$$T_n(t) = T_0' e^{-\lambda_n^2 D t} \tag{C.6}$$
$$X_n(x) = a_n' \sin(\lambda_n x + \alpha_n). \tag{C.7}$$

The differential equation for X including the boundary conditions is a Sturm-Liouville eigenvalue problem. The solution for Equation C.1 is consequently given by the sum ($a_n = a_n' T_0'$):

$$u(x,t) = \sum_{n=1}^{\infty} a_n \sin(\lambda_n x + \alpha_n) e^{-\lambda_n^2 D t}. \tag{C.8}$$

With the boundary conditions in Equation C.4, the constants α_n and λ_n are determined to

$$\alpha_n = n\pi \tag{C.9}$$
$$\lambda_n = \frac{\pi}{L}\left(n - \tfrac{1}{2}\right) \tag{C.10}$$

and the coefficients a_n are determined by analyzing the Fourier series with the initial condition in Equation C.2. Each coefficient a_n is given by:

$$a_n = -\frac{2}{L}\int_0^L \varphi(x') \sin\left(\frac{\pi}{L}\left(n - \tfrac{1}{2}\right) x'\right) \mathrm{d}x' \tag{C.11}$$
$$= -\frac{2\Delta T L}{\pi(2n-1)} \cos\left(\pi\left(n - \tfrac{1}{2}\right)\frac{L_1}{L}\right) \tag{C.12}$$

By inserting these coefficients into the ansatz in Equation C.7, the solution including the backtransformation to T_0 is given by:

$$u(x,t) = T_0 - \sum_{n=1}^{\infty} \frac{4\Delta T}{\pi(2n-1)} \cos\left(\pi\left(n - \tfrac{1}{2}\right)\tfrac{L_1}{L}\right) \sin\left(\pi\left(n - \tfrac{1}{2}\right)\tfrac{x}{L}\right) e^{-\frac{\pi^2}{L^2}\left(n-\frac{1}{2}\right)^2 D t} \tag{C.13}$$

Equation C.13 describes the temperature distribution with respect to time for all spatial positions along the rod of length L, if the initial temperature distribution is given by Equation C.2. Furthermore, the left end of the rod is held at the constant temperature T_0 and the right end is isolated.

The next step in calculating the drift velocity is to find the thermal expansion caused by the temperature change. In a linear approximation using the coefficient of thermal expansion α, the infinitesimal length change $\mathrm{d}L$ of a rod element

$\mathrm{d}x'$ at postion x' is given by:

$$\mathrm{d}L = \left(1+\alpha\left(u(x',t)-\varphi(x')\right)\right)\mathrm{d}x' \tag{C.14}$$

whereby $\varphi(x)$ is the initial temperature distribution. The total length $L(t)$ at time t is consequently given by the integral

$$L(t) = \int_0^L 1+\alpha\left(u(x',t)-\varphi(x')\right)\mathrm{d}x'. \tag{C.15}$$

The drift velocity follows from the temporal derivative:

$$\begin{aligned} v(t) &= \frac{\partial L(t)}{\partial t} = \int_0^L \alpha \frac{\partial u(x',t)}{\partial t}\mathrm{d}x' \\ &= \frac{2D\alpha\Delta T}{L}\sum_{n=1}^{\infty}\cos\left(\pi\left(n-\tfrac{1}{2}\right)\tfrac{L_1}{L}\right)\left(1-\cos\left(\pi\left(n-\tfrac{1}{2}\right)\tfrac{x}{L}\right)\right)e^{-\frac{\pi^2}{L^2}\left(n-\frac{1}{2}\right)^2 Dt}. \end{aligned} \tag{C.16}$$

The drift velocity caused by a temperature change of $\Delta T = 100\,\mathrm{mK}$ for a 10 cm long rod is given in Figure C.2 for four different materials, namely Copper, Tantalum, Al_2O_3 and PZT-4.

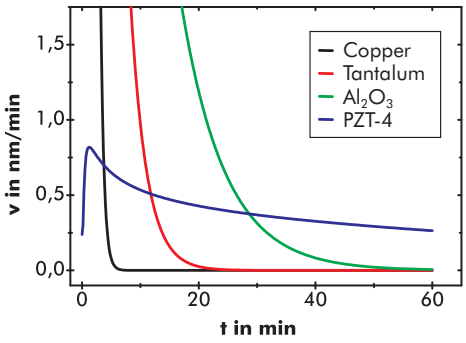

material	D in $10^{-6}\,\mathrm{m^2/s}$	α in $10^{-6}\,\mathrm{K^{-1}}$
Cu	117.0	16.5
Ta	24.5	6.3
Al_2O_3	9.0	8.0
PZT-4	0.67	3.0

Figure C.2.: Drift velocity for four different materials. L=10 cm, L_1=1 cm, ΔT = 100 mK.

I extend this model now by considering two rods of two different materials as depicted in Figure C.3. These two rods are meant to simplify an SPM setup: Let one rod be the scanner piezo, while the second rod represents the scanner and sample support manufactured from a different material. The drift velocity is given by the movement of the two right rod ends relative to each other.

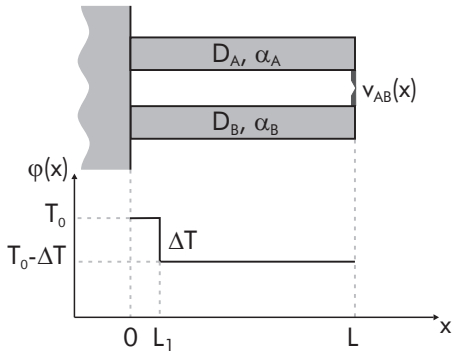

Figure C.3.: Simplified drift model of an SPM setup: Let material A be the sample and scanner support, while B models the piezo scanner.

The drift velocity for this system is given by the difference of Equation C.16 for two different materials. It evaluates to

$$v_{\mathrm{A,B}}(t)=\frac{2\Delta T}{L}\sum_{n=1}^{\infty}\cos\left(\tfrac{\pi L_1}{L}\left(n-\tfrac{1}{2}\right)\right)\left[D_{\mathrm{A}}\alpha_{\mathrm{A}}e^{-\frac{\pi^2}{L^2}\left(n-\frac{1}{2}\right)^2 D_{\mathrm{A}}t}-D_{\mathrm{B}}\alpha_{\mathrm{B}}e^{-\frac{\pi^2}{L^2}\left(n-\frac{1}{2}\right)^2 D_{\mathrm{B}}t}\right]. \tag{C.17}$$

Furthermore, the limit $L_1 \to 0$ is calculated as this reflects a complete rod at a temperature $T_0-\Delta T$. Furthermore, one end is at a constant temperature of T_0 and the other end is isolated. Then, the drift velocity reads

$$v_{\mathrm{A,B}}(t)=\frac{2\Delta T}{L}\sum_{n=1}^{\infty}\left[D_{\mathrm{A}}\alpha_{\mathrm{A}}e^{-\frac{\pi^2}{L^2}\left(n-\frac{1}{2}\right)^2 D_{\mathrm{A}}t}-D_{\mathrm{B}}\alpha_{\mathrm{B}}e^{-\frac{\pi^2}{L^2}\left(n-\frac{1}{2}\right)^2 D_{\mathrm{B}}t}\right]. \tag{C.18}$$

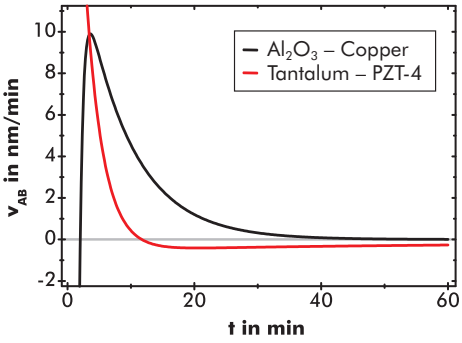

material	D in $10^{-6}\,\mathrm{m^2/s}$	α in $10^{-6}\,\mathrm{K^{-1}}$
Al_2O_3	9.0	8.0
Cu	117.0	16.5
Ta	24.5	6.3
PZT-4	0.67	3.0

Figure C.4.: Drift velocities for different material combinations. L=10 cm, ΔT = 100 mK.

D. Optical properties of calcite

In this section, the relation of the optical properties to the orientation of the calcite $CaCO_3$(10.4) surface is discussed. All calculations have been performed using the software Mathematica.

D.1. Coordinate sytems

Optical properties are usually described in a cartesian coordinate system, while the calcite unit cell is described nowadays usually by the structural hexagonal unit cell. The matrix $\hat{\mathbf{M}}$ transforms a vector from the hexagonal to the cartesian coordinate system and is given by

$$\hat{\mathbf{M}} = \begin{pmatrix} a & -\frac{a}{2} & 0 \\ 0 & a\frac{\sqrt{3}}{2} & 0 \\ 0 & 0 & c \end{pmatrix} \tag{D.1}$$

$$\vec{r}_{\mathrm{c}} = \hat{\mathbf{M}} \cdot \vec{r}_{\mathrm{h}}. \tag{D.2}$$

$\vec{r}_{\mathrm{c}}$ is a vector in the cartesian coordinate system and $\vec{r}_{\mathrm{h}}$ is a vector in the hexagonal system. A subscript h for the hexagonal and subscript c for the cartesian system will be included for convenience in the following.

Throughout this work, the (10.4) surface of calcite is investigated. The vector $\vec{k}_{\mathrm{h}}$ is normal to this surface plane, while the vectors $\vec{e}_{\mathrm{a,h}}$ and $\vec{e}_{\mathrm{b,h}}$ span the surface unit cell. These vectors are defined in the hexagonal coordinate system by

$$\vec{e}_{\mathrm{a,h}} = \begin{pmatrix} 0 \\ 1 \\ 0 \end{pmatrix} \qquad \vec{e}_{\mathrm{b,h}} = \begin{pmatrix} -4 \\ -2 \\ 1 \end{pmatrix} \qquad \vec{k}_{\mathrm{h}} = \begin{pmatrix} 1 \\ 0 \\ 4 \end{pmatrix} \tag{D.3}$$

Using the transformation matrix $\hat{\mathbf{M}}$, the cartesian representation for these vectors

is calculated as:

$$\vec{e}_{\mathrm{a,c}} = \frac{\hat{\mathbf{M}} \cdot \vec{e}_{\mathrm{a,h}}}{\left|\hat{\mathbf{M}} \cdot \vec{e}_{\mathrm{a,h}}\right|} = \begin{pmatrix} -1/2 \\ \sqrt{3}/2 \\ 0 \end{pmatrix} \tag{D.4}$$

$$\vec{e}_{\mathrm{b,c}} = \frac{\hat{\mathbf{M}} \cdot \vec{e}_{\mathrm{b,h}}}{\left|\hat{\mathbf{M}} \cdot \vec{e}_{\mathrm{b,h}}\right|} = \frac{1}{\sqrt{12a^2 + c^2}} \begin{pmatrix} -3a \\ -\sqrt{3}a \\ c \end{pmatrix} \tag{D.5}$$

$$\vec{e}_{\mathrm{n,c}} = \vec{e}_{\mathrm{a,c}} \times \vec{e}_{\mathrm{b,c}} = \frac{1}{2\sqrt{12a^2 + c^2}} \begin{pmatrix} \sqrt{3}c \\ c \\ 4\sqrt{3}a \end{pmatrix}. \tag{D.6}$$

The hexagonal coordinate system is non-orthogonal, thus, the surface normal is recalculated from the cross product of the two surface cell unit vectors. The vector $\vec{e}_{\mathrm{n,c}}$ is perpendicular to the $(10.4)_{\mathrm{h}}$ surface and points outwards in the same direction as the $[10.4]_{\mathrm{h}}$ crystal direction. The angle of this vector with the Z-axis is the well-known value of $\angle(\vec{e}_{\mathrm{n,c}}, \vec{e}_{\mathrm{z,c}}) \sim 44.63°$.

D.2. Optical indicatrix

The properties of a dielectric medium in an electric field is described by the permittivity $\hat{\epsilon}$, defined by the material equation

$$\vec{D} = \hat{\epsilon}\vec{E} \tag{D.7}$$

Here, $\vec{E}$ is the electric field, $\vec{D}$ is the electric displacement field. The permittivity $\hat{\epsilon}$ is generally a tensor of rank two. The electric impermeability tensor $\hat{\eta}$ is defined by $\epsilon_0 \hat{\epsilon}^{-1} = \hat{\eta}$ (ϵ_0: vacuum permittivity) and both tensors completely describe the optical properties of a crystal. Calcite is optically uniaxial and, consequently, the electric impermeability tensor $\hat{\eta}$ can be transformed to the diagonal quadratic form:

$$\hat{\eta} = \begin{pmatrix} \frac{1}{\epsilon_1} & 0 & 0 \\ 0 & \frac{1}{\epsilon_1} & 0 \\ 0 & 0 & \frac{1}{\epsilon_3} \end{pmatrix} \tag{D.8}$$

with relative permittivities ϵ_1 and ϵ_3. The indices of refraction[1] are related to ϵ_i by $n_i = \sqrt{\epsilon_i}$. The optical indicatrix is the representation of $\hat{\eta}$ as defined by:

$$\frac{\vec{D}}{\sqrt{\epsilon_0}} \hat{\eta} \frac{\vec{D}}{\sqrt{\epsilon_0}} = 1, \tag{D.9}$$

[1] Here, the constants for the visible regime are used.

which is the equivalent for defining an ellipsoid:

$$\frac{d_1}{\sqrt{\epsilon_1}^2}+\frac{d_2}{\sqrt{\epsilon_1}^2}+\frac{d_3}{\sqrt{\epsilon_3}^2}=1. \tag{D.10}$$

This index ellipsoid (optical indicatrix) has for calcite main axes of lengths $\sqrt{\epsilon_1}$, $\sqrt{\epsilon_1}$ and $\sqrt{\epsilon_3}$ and is symmetric along the Z-axis. For a given incident electromagnetic wave $\vec{E}(\vec{r},t)=\vec{E}_0\exp\left(i(\vec{k}\vec{r}-\omega t)\right)$, the wave propagation inside the crystal is in the following calculated by using the electric impermeability tensor $\hat{\eta}$.

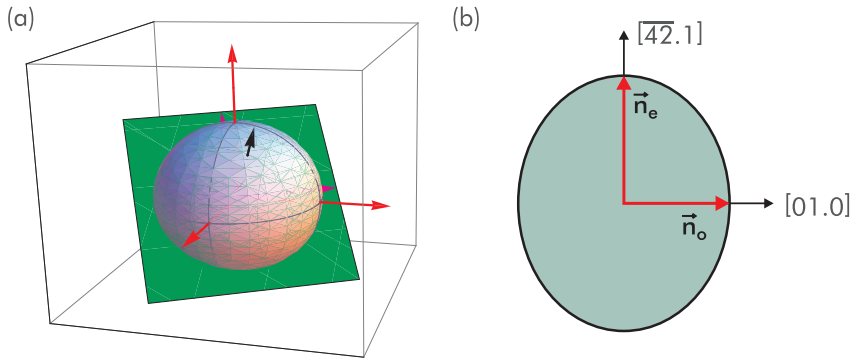

Figure D.1.: (a) Optical indicatrix for $CaCO_3$ including the position of the (10.4) surface plane. In red: base vectors of the cartesian coordinate system, in magenta: unit cell vectors of the (10.4) plane. (b) Elliptic cross section of the (10.4) plane with the optical indicatrix.

The wave vector $\vec{k}_c$ is oriented parallel to the surface normal vector $\vec{e}_{n,c}$, when viewing through a calcite crystal perpendicular to the (10.4) cleavage plane. The orientation of this plane inside the optical indicatrix is depicted in Figure D.1(a). The cross section, usually named index ellipse, is depicted in Figure D.1(b). The semi-minor and semi-major axes define the indices of refraction n_o and n_e for the ordinary and extraordinary ray, respectively.

The semi-major axis is oriented along the [$\overline{42}$.1] crystal direction, while the semi-minor axis points into the [01.0] direction. The vectors pointing in each respective direction are calculated from

$$\vec{n}_o\hat{\eta}\vec{n}_o=1 \qquad \text{with} \qquad \vec{n}_o=a_o\vec{e}_a \tag{D.11}$$

$$\vec{n}_e\hat{\eta}\vec{n}_e=1 \qquad \text{with} \qquad \vec{n}_e=a_e\vec{e}_b \tag{D.12}$$

which is evaluated to

$$\vec{n}_{\mathrm{o}} = \frac{1}{2}\begin{pmatrix} -\sqrt{\epsilon_1} \\ \sqrt{3\epsilon_1} \\ 0 \end{pmatrix} \tag{D.13}$$

$$\vec{n}_{\mathrm{e}} = \sqrt{\frac{\epsilon_1\epsilon_3}{12a^2\epsilon_3 + c^2\epsilon_1}}\begin{pmatrix} -3a \\ -\sqrt{3}a \\ c \end{pmatrix}. \tag{D.14}$$

These modes are usually named "normal modes". The length of the vectors is identical to the refractive indices for the ordinary and the extraordinary ray, respectively. Using the material constants for calcite, the specific values are:

$$n_{\mathrm{o}} = 1.66 \tag{D.15}$$

$$n_{\mathrm{e}} = 1.57. \tag{D.16}$$

For each normal mode, the vector of the dielectric displacement $\vec{D}_{\mathrm{i,c}}$ ($i = \mathrm{o}, \mathrm{e}$) is oriented parallel to n_{i}, and the electric field vector is calculated from the relation $\vec{E}_{\mathrm{i,c}} = \hat{\eta}\vec{D}_{\mathrm{i,c}}$. Here, the dielectric displacement vectors are arbitrarily normed to unity. The electric field vectors are calculated to

$$\vec{E}_{\mathrm{o,c}} = \frac{1}{2\epsilon_1}\begin{pmatrix} -1 \\ \sqrt{3} \\ 0 \end{pmatrix} \tag{D.17}$$

$$\vec{E}_{\mathrm{e,c}} = \frac{1}{\sqrt{12a^2 + c^2}}\begin{pmatrix} -3a/\epsilon_1 \\ -\sqrt{3}a/\epsilon_1 \\ c/\epsilon_3 \end{pmatrix} \tag{D.18}$$

$$\tag{D.19}$$

$\vec{E}_{\mathrm{o,c}}$ is aligned parallel to $\vec{D}_{\mathrm{o,c}}$ and [01.0], while the angle between $\vec{E}_{\mathrm{e,c}}$ and $\vec{D}_{\mathrm{e,c}}$ amounts 6.23°.

The propagation direction for each wave is generally *not* oriented along the wave vector $\vec{k}_{\mathrm{c}}$, but follows the energy flow described by the Poynting vector $\vec{S}_{\mathrm{i,c}}$. These vectors are calculated from $S_{\mathrm{i,c}} = \vec{E}_{\mathrm{i,c}} \times \left(\vec{k}_{\mathrm{c}} \times \vec{E}_{\mathrm{i,c}}\right)$ and the normalised form is:

$$S_{\mathrm{o,n,c}} = \frac{1}{2\sqrt{12a^2 + c^2}}\begin{pmatrix} \sqrt{3}c \\ c \\ 4\sqrt{3}a \end{pmatrix} \tag{D.20}$$

$$S_{\mathrm{e,n,c}} = \frac{1}{2\sqrt{12a^2\epsilon_3^2 + c^2\epsilon_1^2}}\begin{pmatrix} \sqrt{3}c\epsilon_1 \\ c\epsilon_1 \\ 4\sqrt{3}a\epsilon_3 \end{pmatrix} \tag{D.21}$$

$$\tag{D.22}$$

For the ordinary ray, the Poynting vector $\vec{S}_{\mathrm{o,n,c}}$ is parallel to the wave vector $\vec{k}_{\mathrm{c}}$, while for the extraordinary ray, the Poynting vector draws an angle of $\alpha = 6.23°$ with the wave vector $\vec{k}_{\mathrm{c}}$ and, consequently, an angle of α with the (10.4) surface normal vector.

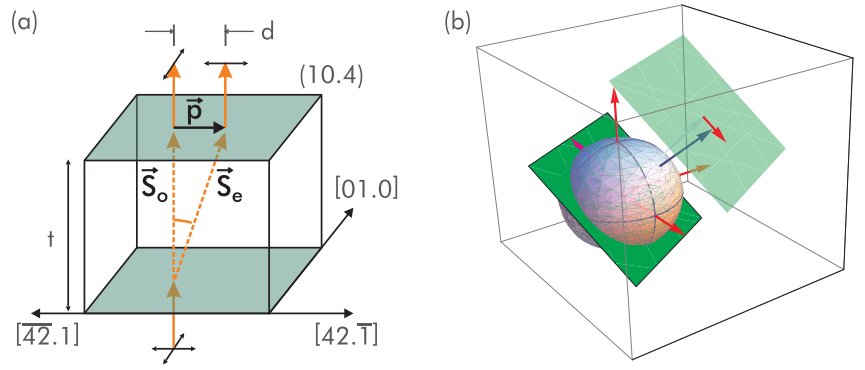

Figure D.2.: (a) Directions of the wave propagation inside a calcite crystal. (b) Positions of the vectors in the optical indicatrix and the sample system.

Of special interest are the crossing points of the ordinary and extraordinary rays with the (10.4) front plane, considering a crystal of thickness t. This is depicted in Figure D.2(a). The split vector $\vec{p}_{\mathrm{c}}$, pointing from the crossing point of the ordinary ray with the front (10.4) surface to the crossing point of the extraordinary ray with the (10.4) surface, is calculated to

$$\vec{p}_{\mathrm{c}} = \frac{t}{\cos\alpha}\vec{S}_{\mathrm{e,n,c}} - t\cdot\vec{S}_{\mathrm{o,n,c}}. \tag{D.23}$$

This vector is aligned parallel to the $[\overline{42}.1]$ substrate direction, because

$$\vec{p}_{\mathrm{c}} = d\cdot\vec{e}_{\mathrm{b,c}} \tag{D.24}$$

has a single solution for $d\,a$, namely

$$d = -\frac{2\sqrt{3}act(\epsilon_1-\epsilon_3)}{12a^2\epsilon_3 + c^2\epsilon_1} \tag{D.25}$$

Especially, the solution is negative for the material constants of calcite, thus, $\vec{p}_{\mathrm{c}}$ points in direction of the $[42.\overline{1}]$ substrate direction.

In conclusion, this analysis allows for identifying the absolute sample orientation by optical means. The top-view examination of a point-like figure placed beneath the calcite crystal reveals the images caused by the ordinary and extraordinary ray. The split direction from the ordinary to the extraordinary picture is oriented along the $[42.\overline{1}]$ substrate direction.

E. Energy barrier estimation

The diffusion barrier and intermolecular binding energy was in this thesis often approximated from experiments at variable temperatures. Within this section, I briefly discuss this approximation. For both, the diffusion barrier E_d and the intermolecular binding energy E_inter, the NC-AFM data usually revealed an estimation for the onset of single molecular diffusion or molecular detachment from island structures, respectively. The rate ν of these diffusion or detachment events follow an Arrhenius law [102]

$$\nu = \nu_0 \exp\left(-\frac{E_\mathrm{i}}{k_\mathrm{B}T}\right) \tag{E.1}$$

with E_i being the respective energy barrier, T being the temperature and ν_0 being the attempt frequency. Solving this equation for E_i yields

$$E_\mathrm{i} = -k_\mathrm{B}T \ln\left(\frac{\nu}{\nu_0}\right) \tag{E.2}$$

$$= -k_\mathrm{B}T \ln(\zeta) \tag{E.3}$$

with $\zeta = \nu/\nu_0$. Interestingly, the energy barrier E_i only depends logarithmical on the rate and the attempt frequency. Thus, these two values are allowed to have a large error. For diffusion events, typical attempt frequencies of $\nu_0 = 10^{10}\,\mathrm{Hz}$ to $10^{13}\,\mathrm{Hz}$ have been reported in literature [102] and the onset of events are revealed within the NC-AFM at rates of $\nu = 10^{-3}\,\mathrm{Hz}$ to $1\,\mathrm{Hz}$. Thus, values for ζ in the range of 10^{-16} to 10^{-10} are reasonable values.

Figure E.1 presents the resulting energy barrier E_i in dependence on the temperature T. The black curve denote the energy value for $\zeta = 10^{-13}$ and the shaded region depict the uncertainty due to the inprecise determination of ν and ν_0. The upper and lower boundary (depicted in orange) are used as the error for E_i herein. Interestingly, despite of the large errors in the determination of ν and ν_0, the energy barrier E_i is determined within reasonable accurancy.

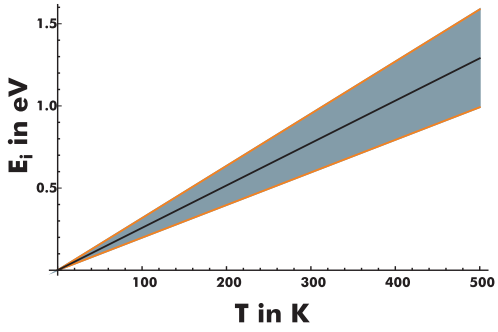

Figure E.1.: Estimation of the diffusion barrier E_d and intermolecular binding energy E_inter from variable temperature experiments. The black curve is drawn for $\zeta = 10^{-13}$, the orange curve estimates the resulting uncertainties due to the errors in the determination of ν and ν_0.

Acknowledgements

An dieser Stelle möchte ich allen Personen danken, ohne die diese Arbeit nicht möglich gewesen wäre:

[Removed to protect privacy]

Publications and presentations

Publications in peer-reviewed journals:

- **P. Rahe, J. Schütte, W. Schniederberend, M. Reichling, M. Abe, Y. Sugimoto, A. Kühnle,** Flexible drift-compensation system for precise 3D force mapping in severe drift environments *Rev. Sci. Inst.* 82 (2011) 063704

- **J. Schütte, R. Bechstein, P. Rahe, H. Langhals, M. Rohlfing, A. Kühnle,** Single-molecule switching with non-contact atomic force microscopy *Nanotechnology* 22 (2011) 245701

- **J. Rybáček, G. Huerta-Angeles, A. Kollárovič, I. G. Stará, I. Starý, P. Rahe, M. Nimmrich, A. Kühnle,** Racemic and Optically Pure Heptahelicene-2-carboxylic Acid: Its Synthesis and Self-Assembly into Nanowire-Like Aggregates *Eur. J. Org. Chem.* 5 (2011) 853

- **A. Greuling, P. Rahe, M. Kaczmarski, A. Kühnle, M. Rohlfing,** Combined NC-AFM and DFT study of the adsorption geometry of trimesic acid on rutile TiO_2(110), *J. Phys. Condens. Matter* 22 (2010) 345008

- **J. Schütte, P. Rahe, L. Tröger, S. Rode, R. Bechstein, M. Reichling, A. Kühnle,** Clear Signature of the (2×1) Reconstruction of Calcite $(10\bar{1}4)$, *Langmuir* 26 (2010) 8295

- **P. Rahe, R. Bechstein, A. Kühnle,** Vertical and lateral drift corrections of scanning probe microscopy images, *J. Vac. Sci. Technol. B* 28 (2010) C4E31

- **M. Nimmrich, M. Kittelmann, P. Rahe, A. J. Mayne, G. Dujardin, A. von Schmidsfeld, M. Reichling, W. Harneit, A. Kühnle,** Atomic-resolution imaging of clean and hydrogen-terminated C(100)$-(2\times1)$ diamond surfaces using noncontact AFM, *Phys. Rev. B* 81 (2010) 201403(R)

- **P. Rahe, M. Nimmrich, A. Greuling, J. Schütte, I. G. Stará, J. Rybáček, G. Huerta-Angeles, I. Starý, M. Rohlfing, A. Kühnle,** Toward Molecular Nanowires Self-Assembled on an Insulating Substrate: Heptahelicene-2-carboxylic acid on Calcite $(10\bar{1}4)$, *J. Phys. Chem. C* 114 (2010) 1547

- **P. Rahe, M. Nimmrich, A. Nefedov, M. Naboka, C. Wöll, A. Kühnle,** Transition of Molecule Orientation during Adsorption of Terephthalic Acid on Rutile TiO_2(110), *J. Phys. Chem. C* 113 (2009) 17471
- **F. Loske, P. Rahe, A. Kühnle,** Contrast inversion in non-contact atomic force microscopy imaging of C_{60} molecules, *Nanotechnology* 20 (2009) 264010
- **J. Schütte, R. Bechstein, P. Rahe, M. Rohlfing, H. Langhals, A. Kühnle,** Imaging perylene derivatives on rutile TiO_2(110) by non-contact atomic force microscopy, *Phys. Rev. B* 79 (2009) 045428
- **P. Rahe, R. Bechstein, J. Schütte, F. Ostendorf, A. Kühnle,** Repulsive interaction and contrast inversion in noncontact atomic force microscopy imaging of adsorbates, *Phys. Rev. B* 77 (2008) 195410

Conference Contributions

(presenting author underlined)

Talks:

- **Molecular self-assembly on calcite**
  A. Kühnle, P. Rahe, J. Schütte, S. Rode
  (DPG spring meeting 2010, Regensburg, Germany)

- **Terephthalic acid on dielectric surfaces using non-contact atomic force microscopy**
  P. Rahe, M. Nimmrich, A. Kühnle
  (DPG spring meeting 2009, Dresden, Germany)

- **Repulsive interaction and contrast inversion in NC-AFM imaging of adsorbates** P. Rahe, R. Bechstein, J. Schütte, F. Ostendorf, F. Loske, A. Kühnle
  (NC-AFM 2008, Madrid, Spain)

- **Unravelling Molecular Contrast Formation Obtained by NC-AFM on Titania**
  R. Bechstein, J. Schütte, P. Rahe, A. Kühnle
  (AVS 54th International Symposium and Exhibition, Seattle, USA)

- **High-resolution imaging of individual perylene derivatives on titania**
  R. Bechstein, J. Schütte, P. Rahe, A. Kühnle
  (NC-AFM 2007, Antalya, Turkey)

Poster presentations:

- **Atom-tracking system for precise 3D force mapping in severe drift environments**
  P. Rahe, J. Schütte, W. Schniederberend, M. Reichling, M. Abe, Y. Sugimoto, A. Kühnle
  (AAFMT workshop 2011, Karlsruhe, Germany)

- **Molecular Self-Assembly on Calcite**
  P. Rahe, M. Nimmrich, J. Schütte, A. Kühnle
  (MRS fall meeting 2010, Boston, USA)

- **Self-organized growth of helicenes on calcite (104) surfaces: Monte Carlo Simulations and Experiments**
  T. Richter, P. Rahe, M. Nimmrich, M. Körner, M. Einax, A. Kühnle, P. Maass
  (DPG spring meeting 2010, Regensburg, Germany)

- **Creating 1D nanostructures: Heptahelicene-carboxylic acid on calcite**
  P. Rahe, M. Nimmrich, A. Greuling, J. Schütte, I. G. Stará, J. Rybácek, G. Huerta-Angeles, I. Starý, M. Rohlfing, A. Kühnle
  (NC-AFM 2009, New Haven, USA

- **The different faces of calcite $(10\bar{1}4)$**
  J. Schütte, L. Tröger, P. Rahe, R. Bechstein, A. Kühnle
  (NC-AFM 2009, New Haven, USA

- **DFT study of TMA on Rutile TiO_2(110)**
  A. Greuling, P. Rahe, A. Kühnle, M. Rohlfing
  (DPG spring meeting 2009, Dresden, Germany)

- **Unravelling molecular contrast formation obtained by NC-AFM**
  R. Bechstein, J. Schütte, P. Rahe, A. Kühnle
  (workshop "Towards Reality in Nanoscale Materials", Levi, Finland)

- **Contrast reversal of protruding adsorbates in NC-AFM**
  P. Rahe, R. Bechstein, A. Kühnle
  (NC-AFM 2007, Antalya, Turkey)

- **Diffusion and manipulation of perylene derivatives on TiO_2**
  J. Schütte, R. Bechstein, P. Rahe, A. Kühnle
  (NC-AFM 2007, Antalya, Turkey)

- **Characterization of Surface Roughness and its Implication on Hydrophobicity**
  K. Brörmann, P. Rahe, A. Kühnle
  (conference ICN+T, Stockholm, Sweden)